BRNO UNIVERSITY OF TECHNOLOGY

VYSOKÉ UČENÍ TECHNICKÉ V BRNĚ

FACULTY OF MECHANICAL ENGINEERING

FAKULTA STROJNÍHO INŽENÝRSTVÍ

INSTITUTE OF PHYSICAL ENGINEERING

ÚSTAV FYZIKÁLNÍHO INŽENÝRSTVÍ TECHNOLOGIE

SEMICONDUCTOR DIAGNOSTICS AND MONITORING OF CHEMICAL REACTIONS BY SIMS METHOD

DIAGNOSTIKA POLOVODIČŮ A MONITOROVÁNÍ CHEMICKÝCH REAKCÍ METODOU SIMS

MASTER'S THESIS

DIPLOMOVÁ PRÁCE

AUTHOR

AUTOR PRÁCE

Bc. MARCEL JANÁK

SUPERVISOR

VEDOUCÍ PRÁCE

Ing. PETR BÁBOR, Ph.D.

BRNO 2021

BRNO UNIVERSITY OF TECHNOLOGY
FACULTY OF MECHANICAL ENGINEERING

Assignment Master's Thesis

Institut:	Institute of Physical Engineering
Student:	**Bc. Marcel Janák**
Degree programm:	Physical Engineering and Nanotechnology
Branch:	no specialisation
Supervisor:	**Ing. Petr Bábor, Ph.D.**
Academic year:	2020/21

As provided for by the Act No. 111/98 Coll. on higher education institutions and the BUT Study and Examination Regulations, the director of the Institute hereby assigns the following topic of Master's Thesis:

Semiconductor diagnostics and monitoring of chemical reactions by SIMS method

Brief Description:

The first part of the diploma thesis will deal with various semiconductor diagnostics methods (localization of defects, quantification of dopants, etc.). The second part will deal with the in–situ analysis of metal surface composition during chemical reactions such as oxidation of carbon monoxide on platinum.

Master's Thesis goals:

1. Create a software and measurement protocol enabling automated detection and localization of high voltage dies defects on a silicon wafer.
2. Calibrate the dopant concentration in AlGaN using ion implantation.
3. Carry out an experiment of oxidation of carbon monoxide in the TOF–SIMS5 device at the CEITEC workplace.
4. Perform an analysis of the platinum surface composition during the carbon monoxide oxidation under various experimental conditions by the static SIMS method.

Recommended bibliography:

BALIGA B. J.: Fundamentals of Power Semiconductor Devices, Springer, 2008

HEIDE, P.: Secondary ion mass spectrometry an introduction to principles and practices, John Wiley & Sons, Inc. 2014

CUI, Z.: Nanofabrication, Principles, Capabilities and Limits, Springer, 2008

REIMER, L.: Scanning Electron Microscopy, Physics of Image Formation and Microanalysis, Springer 1998

Deadline for submission Master's Thesis is given by the Schedule of the Academic year 2020/21

In Brno,

L. S.

prof. RNDr. Tomáš Šikola, CSc. Director of the Institute	doc. Ing. Jaroslav Katolický, Ph.D. FME dean

Abstract

Time-of-flight secondary ion mass spectrometry (TOF-SIMS) is a powerful surface science technique with high sensitivity for elemental composition. This work demonstrates TOF-SIMS abilities in three different research areas.

The first part deals with the localization of high voltage dies defects, which is necessary for their further characterization by the TOF-SIMS method. For this purpose, an experimental setup with control software allowing automated measurement of leakage current tests at various die locations was proposed.

The second part deals with the quantification of Mg dopant depth profiles in various $Al_xGa_{1-x}N$ samples. The quantification is based on the RSF method and allows the characterization of doped $Al_xGa_{1-x}N$ heterostructures for high electron mobility transistors (HEMT) or various optoelectronic devices. A set of 12 Mg doped $Al_xGa_{1-x}N$ calibration samples for quantification of depth profiles was prepared by the ion implantation technique.

The last part demonstrates the abilities of the static TOF-SIMS method in heterogeneous catalysis research. Our primary research objective is the dynamics of catalytic CO oxidation by O_2 to CO_2 on Pt polycrystalline microstructures at high vacuum pressures. In this work we present the first real-time observations of spatiotemporal patterns of varying surface coverages during distinct catalyst regimes. TOF-SIMS observations were correlated with analogous scanning electron microscopy (SEM) observations of gas-phase- and temperature-induced processes on Pt surfaces.

Keywords

TOF-SIMS, semiconductor failure analysis, dynamic SIMS, AlGaN, quantification, Mg doping, ion implantation, static SIMS, heterogeneous catalysis, reaction-diffusion processes, reaction of catalytic CO oxidation

JANÁK, Marcel. *Semiconductor Diagnostics and Monitoring of Chemical Reactions by SIMS Method.* Brno, 2021. 83 p. Master's thesis. Brno University of Technology, Faculty of Mechanical Engineering. Supervised by Petr BÁBOR.

Abstrakt

Hmotnostná spektrometria sekundárnych iónov s analýzou doby letu (TOF-SIMS) patrí vďaka vysokej citlivosti na prvkové zloženie medzi významné metódy analýzy pevných povrchov. Táto práca demonštruje možnosti TOF-SIMS v troch odlišných oblastiach výskumu.

Prvá časť práce sa zaoberá lokalizáciou defektov vysokonapäťových polovodičových súčiastok, ktorá je nevyhnutná k ich ďalšiemu skúmaniu metódou TOF-SIMS. Bola navrhnutá experimentálna zostava s riadiacim softvérom umožňujúca automatizované meranie záverného prúdu v rôznych miestach polovodičových súčiastok.

Druhá časť práce sa zaoberá kvantifikáciou koncentrácie Mg dopantov v rôznych hĺbkach vzoriek $Al_xGa_{1-x}N$. Kvantifikácia je založená na metóde RSF a umožňuje charakterizáciu $Al_xGa_{1-x}N$ heteroštruktúr určených na výrobu tranzistorov s vysokou elektrónovou mobilitou (HEMT) alebo na výrobu rôznych optoelektronických zariadení. Sada 12 $Al_xGa_{1-x}N$ kalibračných vzoriek dopovaných Mg, určených na kvantifikáciu hĺbkových profilov, bola pripravená metódou iónovej implantácie.

Posledná časť práce demonštruje možnosti metódy TOF-SIMS vo výskume heterogénnej katalýzy. Hlavným objektom nášho výskumu je dynamika oxidácie CO na CO_2 pomocou O_2 na polykryštalickom povrchu platiny za tlakov vysokého vákua. V tejto práci prezentujem prvé TOF-SIMS pozorovanie časopriestorových vzorov v reálnom čase, ktoré vznikajú v dôsledku rôzneho pokrytia povrchu Pt reaktantmi. Výsledky TOF-SIMS experimentu boli porovnané s výsledkami podobného experimentu v rastrovacom elektrónovom mikroskope (SEM).

Kľúčové slová

TOF-SIMS, analýza porúch polovodičových súčiastok, dynamická SIMS, AlGaN, kvantifikácia, Mg dopovanie, iónová implantácia, statická SIMS, heterogénna katalýza, reakčne-difúzne procesy, reakcia katalytickej CO oxidácie

I hereby declare that I have written my master's thesis on the theme of *Semiconductor diagnostics and monitoring of chemical reactions by SIMS method* independently, under the guidance of the master's thesis supervisor, Ing. Petr Bábor, Ph.D., and using the technical literature and other sources of information which are all properly quoted in the thesis and detailed in the list of literature at the end of the thesis.

Bc. Marcel Janák

Acknowledgement

At this point, I would like to thank my supervisor Ing. Peter Bábor, PhD. for his support and for sharing valuable suggestions with me during our three-year collaboration. My thanks go to Prof. Dr. Daniel Primetzhofer and Sotirios Droulias for the preparation of samples during my stay at the Uppsala University. I am thankful to doc. Ing. Miroslav Kolíbal, PhD. for EBSD measurements. I am also grateful to my friends Karel Vařeka, Radek Holeňák, Antonín Jaroš and Dominik Hrůza for cooperation on projects. Last but not least, I thank my family for their support during my studies.

CzechNanoLab project LM2018110 funded by MEYS CR is gratefully acknowledged for the financial support of the measurements/sample fabrication at CEITEC Nano Research Infrastructure.

This work was supported in 2020 as part of the LDDA project by the ON Semiconductor company.

Bc. Marcel Janák

Contents

Introduction

The history of secondary ion mass spectrometry (SIMS) instruments dates back to the early 1960s when the first magnetic sector SIMS assemblies were constructed [1]. The first time-of-flight secondary ion mass spectrometry (TOF-SIMS) devices were constructed about 20 years later, in the early 1980s [2]. Commercialization of the SIMS method in recent decades has made this technique an accessible tool for the study of the elemental composition of solid surfaces both in industry and academia. The unceasing progress in the performance of SIMS components constantly opens up new application possibilities. This work demonstrates two applications of TOF.SIMS 5 instrument from the IONTOF company available at the CEITEC Nano laboratory. The third experiment suggests the usage of TOF.SIMS 5 instrument for investigation of high voltage dies defects, however in this work, only the method for their localization is proposed.

Compared with other conventional surface science techniques like AES, XPS, or LEIS, the most significant advantage of the SIMS method is the high sensitivity to detect species with atomic concentrations lower than one particle per billion. However, due to the matrix effect, the high sensitivity is associated with the difficulty to convert the number of ionized sputtered atoms into their concentration in the sample. The seriousness of other limitations depends on applications. The ultimate physical limit of spatial resolution reaches 10 nm. Typical static SIMS measurements have a spatial resolution of 1 µm, during which about 1-10% of surface atoms are sputtered. Depth resolution reaches about 1 nm. Dynamic SIMS measurements are by nature destructive. Returning to advantages, the SIMS method can detect all periodic table elements and their isotopes. The detection of large molecules is possible with cluster primary ion sources. Otherwise, the molecules break into smaller ones.

TOF.SIMS 5 applications in our work cover both dynamic SIMS (DSIMS) and static SIMS measurements (SSIMS). DSIMS depth profiling of Mg doped $Al_xGa_{1-x}N$ samples takes advantage of high sensitivity, while the matrix effect needs to be overcome. The quantification of Mg concentration in various $Al_xGa_{1-x}N$ samples finds application in the characterization of MOCVD grown $Al_xGa_{1-x}N$ heterostructures for optoelectronic devices or high-power electronic devices. SSIMS monitoring of catalyzed CO oxidation to CO_2 over Pt surfaces takes advantage of high sensitivity and the possibility to monitor elemental, isotopic, and molecular surface composition. The effect of the ion probe on the surface reaction is examined. Our results show the first real-time observations of spatiotemporal patterns of varying surface coverages. Spatiotemporal patterns observed by TOF.SIMS 5 were compared with analogous scanning electron microscopy (SEM) experiments.

This thesis consists of four chapters. In the first chapter, TOF-SIMS method is introduced. In the second chapter, the experimental setup for localization of high voltage dies defects on silicon wafers is proposed and tested on defective fast recovery diodes (FRD) and trench insulated gate bipolar transistors (TIGBT). Measurement software with a graphical user interface allowing both measurement automatization and data processing is presented. In the third chapter, the quantification of Mg depth profiles in various AlGaN samples by the RSF method is shown. Calibration samples prepared by ion implantation allow the quantification of depth scale, quantification of matrix species, and quantification of dopant concentrations. In the fourth chapter, the applicability of the SSIMS method

in heterogeneous catalysis research is demonstrated. In the beginning, heterogeneous catalysis and catalyzed CO oxidation to CO_2 over Pt surfaces are introduced. After that, TOF-SIMS and UHV-SEM observations of gas-phase- and temperature-induced processes on Pt surfaces during the reaction of CO oxidation are presented.

1. Time-of-flight secondary ion mass spectrometry

Secondary ion mass spectrometry (SIMS) is a destructive surface science technique providing information about the elemental, isotopic, and molecular composition of solid surfaces. SIMS analysis is based on surface atoms sputtering by primary ions. The mass to charge ratio of ionized sputtered atoms, i.e., secondary ions, is determined by the mass spectrometer. The mass spectrometer defines the type of the SIMS instrument. Commonly used SIMS instrument types are magnetic sector SIMS instruments, quadrupole SIMS instruments, and time-of-flight SIMS instruments. Since TOF.SIMS 5 [3] instrument employed in this work belongs to the TOF-SIMS group, the following text primarily aims to explain TOF-SIMS working principles.

1.1. Instrument overview

The main TOF-SIMS instrument parts are the primary ion gun, the sputter gun, the mass spectrometer, the detector, and the vacuum system. The primary ion gun is used to generate secondary ions, while the sputter gun serves for material removal during depth profiling. Time-of-flight mass spectrometer separates accelerated secondary ions based on the time necessary to hit the detector. The number of secondary ions is counted by the detection system. The time-of-flight mass spectrometer working principle indicates that secondary ions need to be split into pulses when analyzed. Secondary ion pulses may be generated either by pulsed primary ion beam or pulsing of secondary ion beam. TOF.SIMS 5 instrument at the CEITEC Nano laboratory utilizes a pulsed primary ion beam. The vacuum system ensures minimal surface contamination, minimal scattering of flying ions and protects electromagnetic lenses from electric discharges. Besides the main parts, TOF-SIMS instruments are usually equipped with other devices, like ion guns, detectors, etc., enabling a more comprehensive range of the instrument applicability. A scheme of TOF.SIMS 5 instrument is displayed in Fig. 1.1.

TOF.SIMS 5 primary ion gun is composed of bismuth-manganese (Bi - Mn) liquid metal ion source (LMIS), electromagnetic lenses, electrodes, and apertures forming and focusing the primary ion beam onto the sample surface. Up to 30 keV bismuth primary ions (Bi^+, Bi_3^+, Bi_3^{+2}, Bi_4^+, Bi_5^{+2}) are extracted from the sharp tungsten tip (source electrode) covered with liquid Bi - Mn alloy. Liquid Bi - Mn is supplied from a heated reservoir attached to the source electrode. A high-voltage extraction electrode provides the ion extraction, and a suppressor electrode provides the stabilization of ion emission. In order to form a pulse out of a DC[1] ion beam, the primary ion gun is equipped with an electro-dynamic mass filter. The first pulsing system of the mass filter (pre-chopper) cuts a short ion package out of the DC beam. Since the ion package comprises multiple ions of the same energy but different masses, the difference in velocity causes the pulse to widen. Therefore, the second pulsing system (chopper) is added to selects a package containing ions of the same mass and minimal energy spread ($\sim 5\,\mathrm{eV}$). The pulse width at the sample surface may be further reduced from 10^1 ns to the sub-nanosecond range by a bunching system.

[1] direct current

The pulse modified by the bunching system provides better mass resolution but worse lateral resolution and increased energy spread. An electrostatic beam blanking system stops the beam from hitting the sample when necessary. Scanning coils, stigmators, and objective lens are placed at the end of the column. Primary ion gun scheme is displayed in Fig. 1.2.

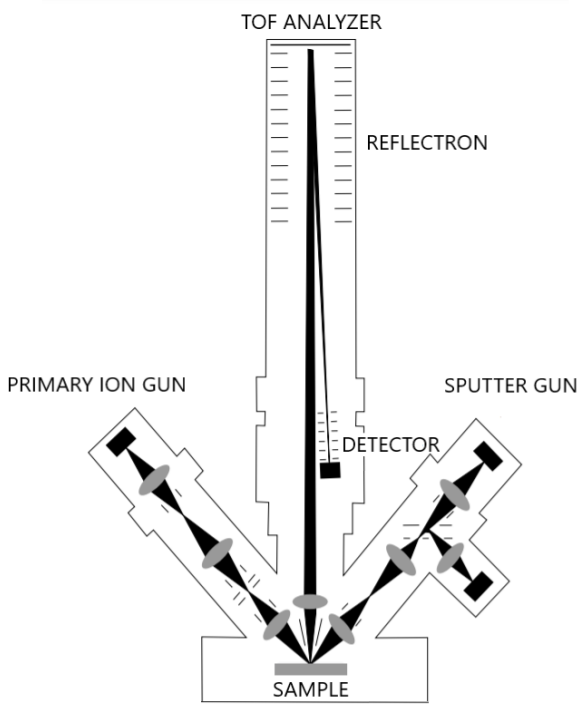

Fig. 1.1: TOF.SIMS 5 instrument scheme. Adapted from [4].

Material removal during depth profiling by TOF.SIMS 5 instrument is provided by dual source column. O_2^+ ions are used to enhance the yield of positively charged secondary ions, while Cs^+ ions are used to enhance the yield of negatively charged secondary ions. Up to 2 keV O_2^+ ions are created in the duoplasmatron ion source, and up to 2 keV Cs^+ ions are created in the surface ionization source. Besides the dual source column, TOF.SIMS 5 instrument at the CEITEC Nano laboratory is also equipped with Ar^+ and O_2^+ gas cluster ion beam (GCIB) column. Up to 30 keV clusters composed of up to 5 000 atoms are suitable for organic samples sputtering since sputtering by clusters preserves information about chemical composition. Sample modifications or tomography measurements may be done by 30 keV Ga^+ focused ion beam (FIB). Nonconductive sample charging may be compensated by an electron flood gun.

Time-of-flight mass spectrometer of TOF.SIMS 5 instrument is composed of electrodes and deflectors tracing the pulse of secondary ions from the sample surface onto the detection unit. Secondary ions are extracted by the extractor electrode, focused by a three-electrode lens, and centered by a deflection unit. A pulse of secondary ions flying through about a 2 m long flight tube is sorted by a mass to charge ratio. Time t necessary for secondary ions with mass m and charge q to fly through the tube of length D is:

$$t = D\sqrt{\frac{m}{2 \cdot q \cdot \Delta U}}, \tag{1.1}$$

where ΔU denotes extraction voltage. The difference in initial velocity of secondary ions is compensated by the reflectron, i.e., ion mirror. Reflectron is composed of multiple parallel electrodes reflecting the flying ions. Ions of the same mass but different initial energies fly pathways of different lengths and hit the detector at the same time. 100% transmissivity of secondary ions flying through the time-of-flight mass spectrometer and therefore also high sensitivity makes TOF-SIMS instruments an ideal tool for analysis of surfaces, i.e., static SIMS. Another advantage of the time-of-flight mass spectrometer over the magnetic sector is the unlimited detection mass range. During analysis of volumes, i.e., dynamic SIMS, TOF-SIMS instruments exhibit lower sensitivity than magnetic sector equipped SIMS instruments because the material cannot be sputtered and detected continuously.

Before hitting the detector, secondary ions are accelerated by the post acceleration unit. The secondary ion detection system of TOF.SIMS 5 instrument is composed of the multichannel plate (MCP), scintillator, photomultiplier, and other signal processing devices. MCP converts a signal of secondary ions to the signal of electrons, which is converted by scintillator to the signal of photons. The signal of photons is outside the vacuum further processed and converted to the mass spectrum. Time-of-flight mass spectrometer with detection system is displayed in Fig. 1.2. Besides secondary ion detection system, TOF.SIMS 5 instrument at the CEITEC Nano laboratory is also equipped with the detector of secondary electrons.

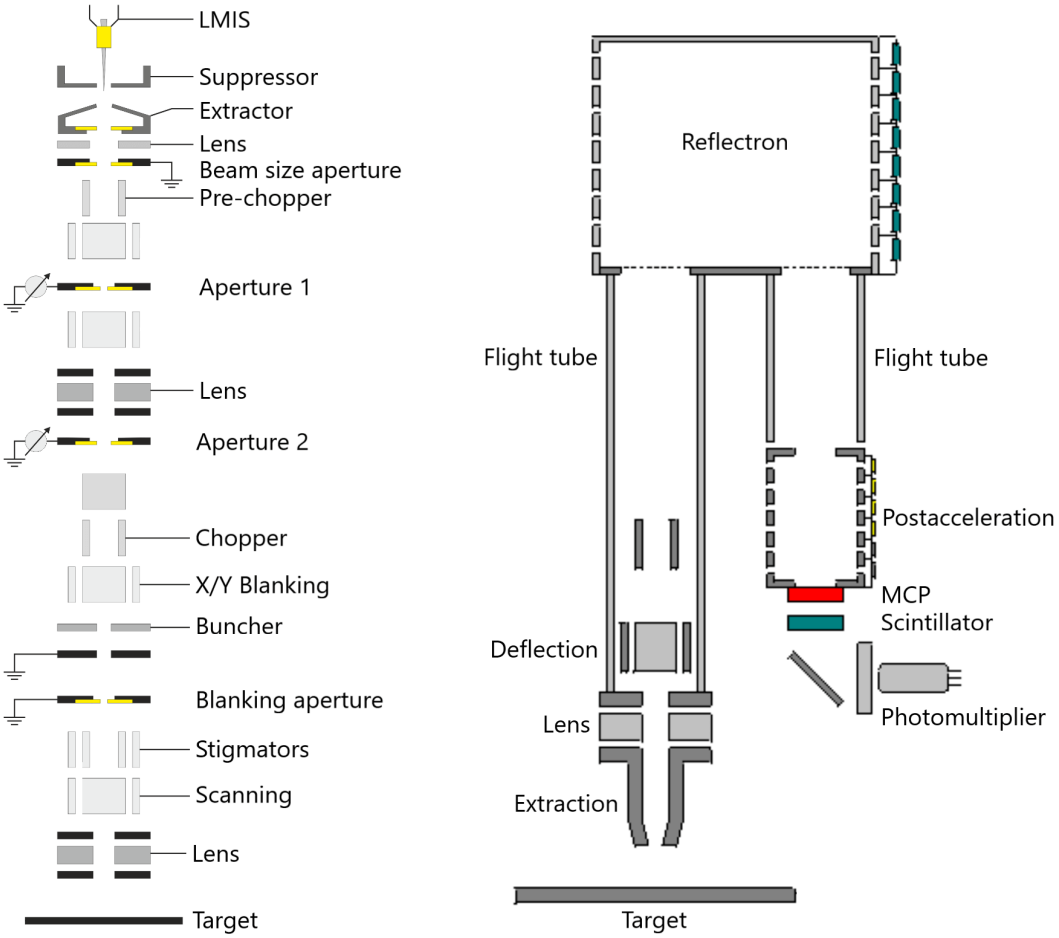

Fig. 1.2: (*left*) Primary ion gun scheme. (*right*) Scheme of time-of-flight mass spectrometer with detection system. Adapted from [5].

The vacuum system of TOF.SIMS 5 instrument is composed of the main vacuum chamber, loadlock chamber, vacuum pumps, vacuum gauges, and a set of valves. Ultrahigh vacuum (UHV) conditions ($< 10^{-7}$ Pa) in the main microscope chamber, ion columns, and TOF analyzer are maintained by a turbomolecular pump backed by a rotary pump. A titanium sublimation pump may further improve UHV conditions. Penning gauges monitor the pressure in various vacuum system parts. The yield of positively charged secondary ions may be enhanced by oxygen flooding through an automated flow regulating valve. The main chamber is equipped with a 5-axis manipulator allowing rotation, tilt, and XYZ positioning. Sample temperature can be decreased by liquid nitrogen cold finger or increased by a resistive heater with a temperature controller. Temperature measurement is provided by a type K thermocouple (chromel/alumel).

1.2. SIMS Measurement

Typical outputs of TOF-SIMS measurements are a mass spectrum, a depth profile, and a lateral sample map. Mass spectrum plots a number of detected ions as a function of mass to charge ratio. The vast majority of secondary ions exist in either -1 or $+1$ charge state. The biggest challenge in mass spectrum processing is mass interference. Mass interference may be partially suppressed by decreasing a primary ion beam pulse width and therefore increasing a mass resolution. Depth profile plots a number of detected ions as a function of sputter time. The mass range for the depth profile is selected in the mass spectrum. The lateral sample map shows a distribution of secondary ions from a certain mass range in 2D space. The lateral resolution depends on the primary ion gun settings and typically ranges from 10 µm to about 50 nm. 3D model of the sample may be reconstructed by combining depth profile with lateral map. A data processing software SurfaceLab 6 from the IONTOF company provides calibration of mass spectra, calibration of depth scale, calibration of concentration, and definition of own regions of interest (ROI) for each graph.

1.3. Ion beam - target interaction

Energetic primary ions transfer energy to surface atoms when impinging. If the energy transferred to surface atoms exceeds their bonding energy, surface atoms may be sputtered. Typical sputtering threshold energies range from 15 eV to 40 eV [4]. The transfer of energy between target atoms induces collision cascades in the material. Collisions within the cascade may be either elastic or inelastic. Elastic energy losses, also known as nuclear stopping, describe interactions between the moving projectile and target nuclei. Inelastic energy losses, also known as electronic stopping, describe interactions between the moving projectile and target electrons. The energy loss of projectile per unit path length ($\mathrm{d}E/\mathrm{d}x$), i.e. the stopping power, is defined as the sum of nuclear $(\mathrm{d}E/\mathrm{d}x)_{\mathrm{n}}$ and electronic $(\mathrm{d}E/\mathrm{d}x)_{\mathrm{e}}$ stopping [6]:

$$\left(\frac{\mathrm{d}E}{\mathrm{d}x}\right) = \left(\frac{\mathrm{d}E}{\mathrm{d}x}\right)_{\mathrm{n}} + \left(\frac{\mathrm{d}E}{\mathrm{d}x}\right)_{\mathrm{e}}. \tag{1.2}$$

Elastic collisions result in a change of projectile and target particle trajectories. Inelastic collisions result in electron excitations, while trajectories are preserved.

The final velocities and trajectories of two isolated particles colliding elastically can be found by applying momentum and energy conservation principles. In the following equations, we assume a moving projectile and stationary target particle. Schematics of a binary collision is displayed in Fig. 1.3.

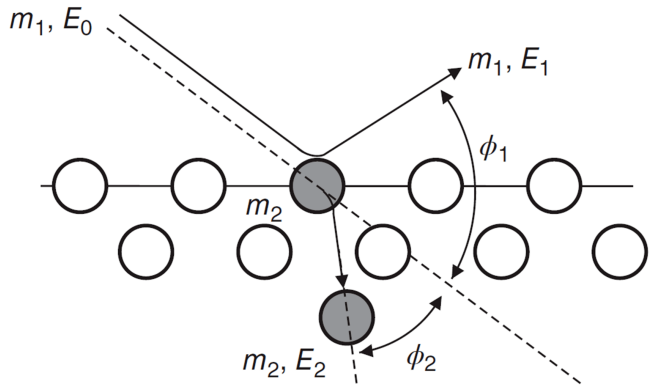

Fig. 1.3: Schematics of a binary collision. Moving projectile with mass m_1 and intitial energy E_0 elastically collides with stationary target particle with mass m_2. Taken from [4].

Scattering angles of the two particles in laboratory coordinates may be expressed as [6]:

$$\phi_1 = \tan^{-1} \frac{m_2 \sin\theta}{m_1 + m_2 \cos\theta}, \quad \phi_2 = \frac{\pi - \theta}{2}, \tag{1.3}$$

where ϕ_1 denotes projectile scattering angle, m_1 is projectile mass, ϕ_2 is target particle scattering angle, m_2 is target particle mass, and θ is the scattering angle in center-of-mass coordinates. The center-of-mass scattering angle may be expressed as [6]:

$$\theta = \pi - 2 \int_{r_{\text{min.}}}^{\infty} \frac{b\,\mathrm{d}r}{r^2 \sqrt{1 - \frac{V(r)}{\frac{1}{2}\mu v_0^2} - \frac{b^2}{r^2}}}, \tag{1.4}$$

where b denotes the impact parameter, i.e., the distance of closest approach of the two particles with the absence of the interaction, $r_{\text{min.}}$ is the distance of closes approach, r is the distance of the two particles, $\mu = \frac{m_1 m_2}{m_1 + m_2}$ is the reduced mass, v_0 is the projectile incident velocity, $V(r)$ is the interatomic potential, e.g., screened Coulomb potential.

The energy of projectile after collision E_1 equals [7]:

$$E_1 = E_0 \left(\frac{\left(m_2^2 - m_1^2 \sin^2\phi_1\right)^{1/2} + m_1 \cos\phi_1}{m_1 + m_2} \right)^2, \tag{1.5}$$

where E_0 denotes the energy of the projectile before the collision. The energy of the target particle after the collision E_2 equals [7]:

$$E_2 = E_0 \frac{4\, m_1 m_2}{\left(m_1 + m_2\right)^2} \cos^2\phi_2. \tag{1.6}$$

The probability of projectile scattering into angle ϕ_1 is proportional to the scattering cross-section σ [7]:

$$\sigma(\phi_1) = \left(\frac{Z_1 Z_2 e^2}{4\, E_0} \right)^2 \frac{4}{\sin^4\phi_1} \frac{\left(\cos\phi_1 + \left[1 - \left(m_1/m_2\right)^2 \sin^2\phi_1\right]^{1/2}\right)^2}{\left[1 - \left(m_1/m_2\right)^2 \sin^2\phi_1\right]^{1/2}}, \tag{1.7}$$

where Z_1 denotes a projectile atomic number, Z_1 is the target particle atomic number, and e is the elementary charge.

2. Localization of high voltage dies defects

This part of the thesis is concerned with developing a fully automated, easy-to-control, and reliable method for failure analysis of defective chips supplied by ON Semiconductor company. Functionality of the measurement assembly was verified by the inspection of two 6-inch wafers. One wafer contains 300 TIGBT (Trench Insulated Gate Bipolar Transistor) dies, and the other contains 579 FRD (Fast Recovery Diode) dies, see Fig. 2.1. Our primary aim was to localize defects within the active area of FRD dies, and the source area of TIGBT dies. In order to localize defects with micrometer accuracy, leakage current tests at various die positions were carried out. Our setup's main building blocks are a semi-automated 4-probe station from Cascade Microtech, electrometer Keithley 6517B with a build-in 1 kV voltage source, and control software with a graphical user interface (GUI). The measurement software, fully developed within this project, allows both controlling experimental setup and processing measured data. Localization of defects is necessary for their further characterization by the SIMS (Secondary Ion Mass Spectrometry) technique.

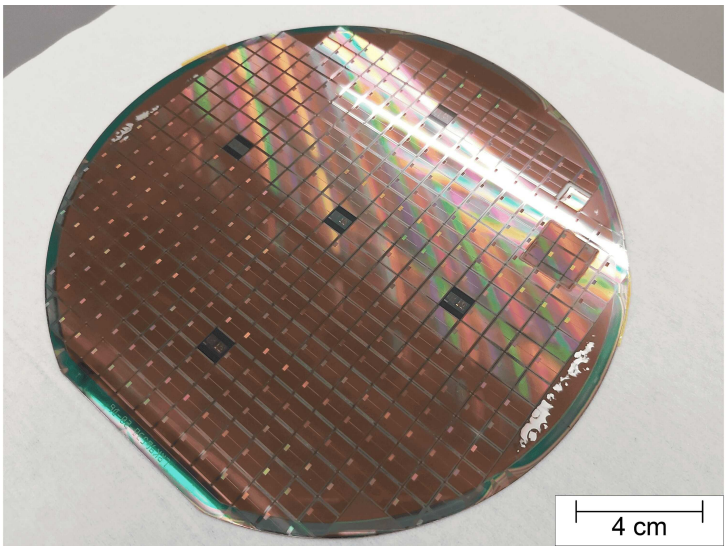

Fig. 2.1: 6-inch wafer with 300 TIGBT dies. Typical sample supplied by the ON Semiconductor company.

2.1. Experimental setup

Semi-automated 4-probe system Cascade Microtech SUMMIT 12000 is an ideal tool for precise on-wafer device characterization. Analytical EMI[1] shielded microchamber with guarded vacuum chuck is suitable for ultra-low noise measurements and leakage current tests of power devices on silicon wafers. Sample navigation with micrometer accuracy is carried out by 4-axis motorized positioning system. Besides that, the 4-probe system is equipped with a microscope imaging video system for precise navigation around the sample. Manipulation with the probe station, e.g., chuck positioning, microscope operation, or

[1] electromagnetic interference

partial measurement automatization, is provided by the *Velox* software. The *Velox* software and, thereby also the whole probe station can be controlled from a client computer via a GPIB[2] interface.

Voltage sweeping and leakage current measurements up to 1 mA are provided by Keithley 6517B electrometer. The main reason to choose Keithley 6517B electrometer is a built-in 1 kV voltage source. Other voltage sources available at the CEITEC Nano laboratory operate at much lower voltages (usually up to 200 V). Another advantage of Keithley 6517B electrometer is a built-in diode leakage current test sequence defined by start voltage, stop voltage, step voltage, and time delay between steps. The electrometer can be controlled from a client computer via a GPIB interface as well.

Communication of a control computer with SUMMIT 12000 probe station and Keithley 6517B electrometer is realized via a GPIB cable and National Instruments GPIB–USB-B adapter. Both SUMMIT 12000 probe station and Keithley 6517B electrometer support standard commands for programmable instruments (SCPI). A control program of the experimental setup is written in a Python programing language, see Sec. 2.2.

The whole experimental setup is displayed in Fig. 2.2.

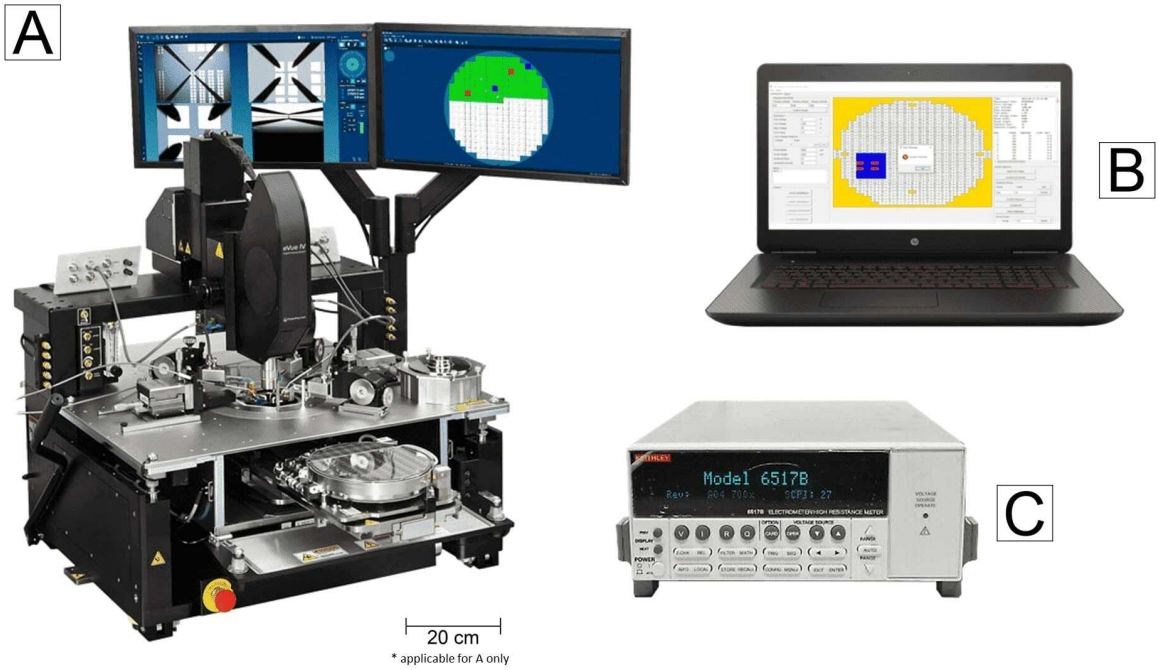

Fig. 2.2: Experimental setup. A - semi-automated 4-probe system Cascade Microtech SUMMIT 12000; B – computer with control software; C - Keithley 6517B electrometer.

2.2. Measurement software

The measurement software is divided into the *EXPERIMENT* part, used for controlling all instruments in the experimental setup, and the *DATA* part, used for measured data processing.

[2]general purpose interface bus

2.2.1. Control of instruments

Analyzing hundreds of dies at one round undoubtedly requires a full automatization of the measurement process. The total number of measurement positions equals the number of analyzed dies multiplied by the number of positions within one die necessary for precise localization of defects with few micrometers in size. Analysis of dies with tens of millimeters in width and height typically requires hundreds of measurement positions within the die. However, due to the increasing density of measurement positions, wafer local temperature during the analysis may increase significantly. Elevated local temperature affects the measurement results. In the worst case, the die may get damaged. The overheating problem can be solved by adding a time delay between measurement steps. However, adding a pause between measurement steps may extensively prolong the analysis time. Less time-consuming overheating elimination can be achieved by designing sophisticated measurement sequences where every measurement position is followed by a measurement position at a much cooler part of the wafer. Each analytical step is defined by time, testing voltage, and two position parameters, namely, die number, and subdie number, i.e., the position within the die. Die response to one analytical step is a leakage current value. Various sequences of analytical steps can provide faster wafer analysis with suppressed local overheating. In order to comfortably define sophisticated measurement sequences, control software with a graphical user interface needs to be developed.

A control software with GUI developed as a part of this project is displayed in Fig. 2.3 and Fig. 2.4. Before each measurement, the user needs to select one of sixteen available die scanning sequences (D01-D16), one of nine available subdie scanning sequences (S01-S09), and one of three available voltage sequences (V01-V03). Available scanning sequences include sawtooth and zigzag sequences with various initial positions and initial scanning directions (left-right, right-left, bottom-up, up-bottom). The user may also prioritize specific dies or define completely new scanning sequences. The first voltage sequence has a regular voltage step and does not include a time delay. The second voltage sequence has a regular voltage step and includes a time delay. The third voltage sequence is entirely defined by the user. The order in which the user selects die (D--), subdie (S--), and voltage (V--) sequences affects the final measurement sequence. According to the selected sequence, the user defines related measurement parameters like first voltage, last voltage, voltage step, time delay, die width, die height, and subdie mesh parameters. Subsequently, the user selects on the wafer map dies for analysis and on the die map subdies for analysis. A detailed measurement sequence and listing of measurement parameters are displayed in the overview window. After the final check of entered data, the user starts the measurement. The running measurement can be paused or stopped at any time of the analysis.

The main output of each measurement is a .txt file containing information about each analytical step, namely, time, die number, subdie number, testing voltage, and leakage current. The output file is supplemented with new data after each analytical step. All further data processing uses the data from this file. Additional output files are a .txt file containing information about measurement parameters and a screenshot of the wafer map with analyzed dies. To make the software even more user-friendly, we added a function of saving and loading own measurement setups. The primary purpose of this feature is to make the process of measurement initialization much quicker. In the case of supplying new wafers with different geometries by ON Semiconductor company, the user can easily

define and load a new wafer map into the GUI. The program communicates with the user by error and information message boxes.

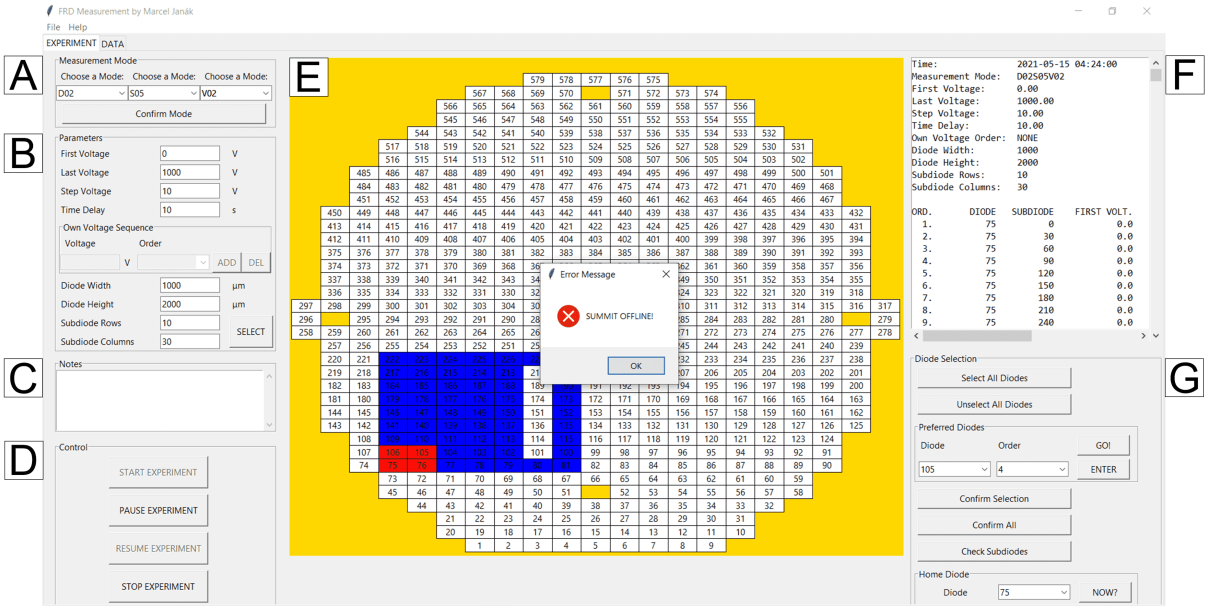

Fig. 2.3: *EXPERIMENT* part of the control software. A – selection of scanning sequence; B – definition of measurement parameters; C – space for notes; D – start/pause/resume/stop measurement buttons; E – wafer map (nonselected dies – white, selected dies – blue, prioritized dies – red, background – yellow); F – overview window; G – other advanced options. Error message boxes guide the user to the measurement initialization.

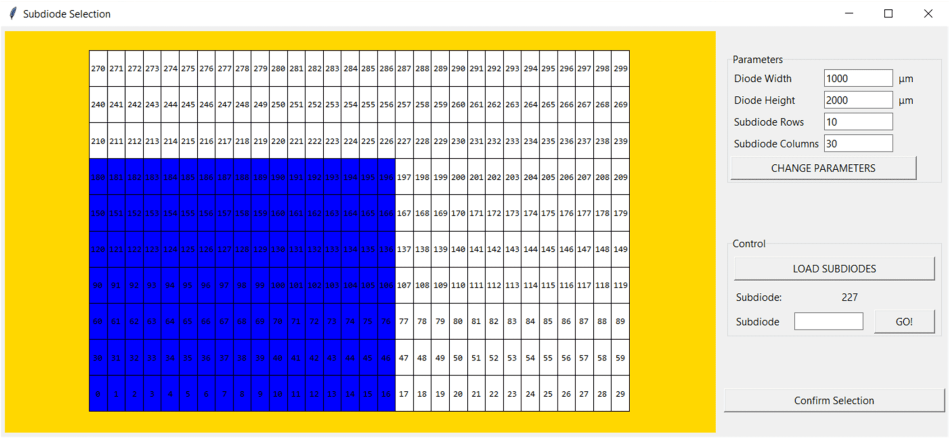

Fig. 2.4: Die map for subdie selection (nonselected subdies – white, selected subdies – blue, background – yellow).

2.2.2. Data processing

Processing data from thousands of analytical steps requires data processing software with a GUI too. The best solution for data analysis seems to be an output of three different graphs, namely, subdie IV curve (see Fig. 2.5), wafer color bitmap where each leakage current value at specific testing voltage is represented by a unique color shade (see Fig. 2.6), and

a histogram representing a number of subdies with leakage currents lying in a specific leakage current range (see Fig. 2.6). The x-axis in the histogram represents leakage current values; the y-axis represents the total number of subdies in a specific small leakage current range. Each histogram refers to a particular testing voltage. The selection of leakage current range for a color bitmap is based on the histogram graph. Subdies with leakage currents below the minimal value of the leakage current range are marked by a red color, measurement positions with the leakage currents above the maximal value of the leakage current range are marked by a dark blue color.

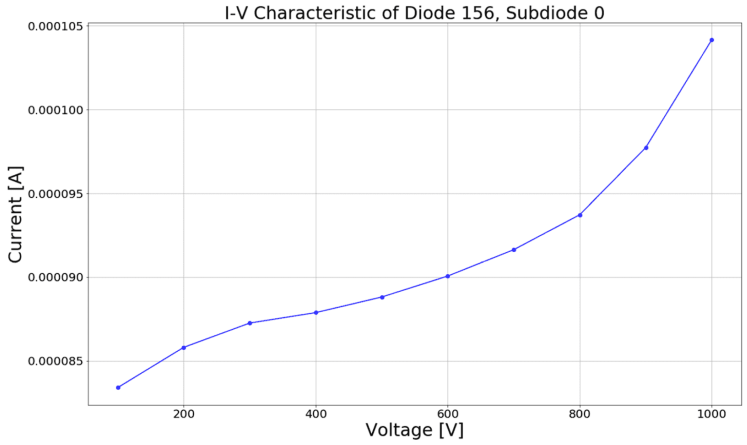

Fig. 2.5: Subdie IV curve graph (original software output).

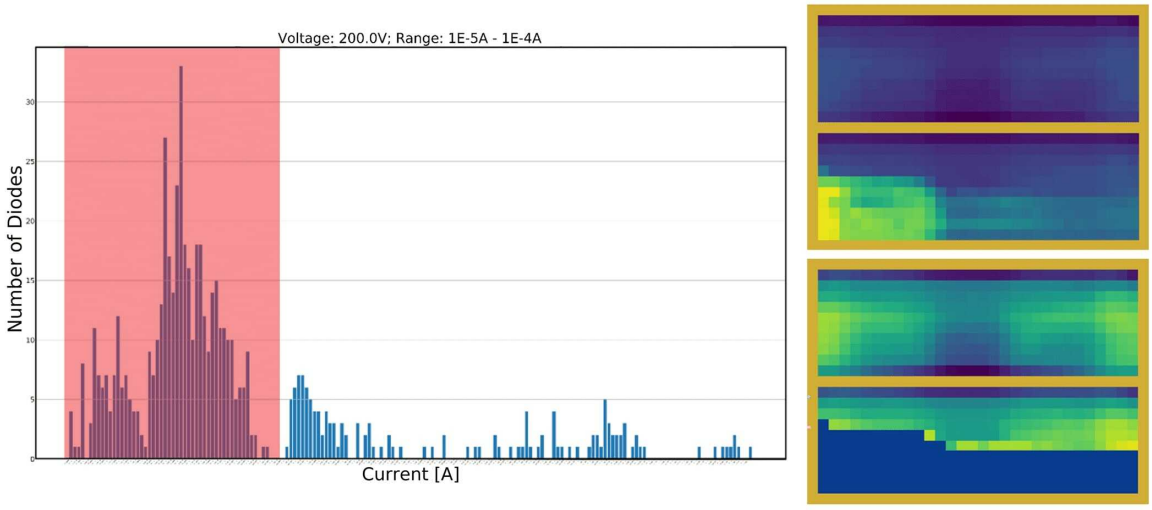

Fig. 2.6: Histogram *(left)* and color bitmaps *(right)* (original software outputs). Both color bitmaps originate from the same measurement output file. A different leakage current range causes the difference in visual. The upper color bitmap is plotted for the whole leakage current range displayed in the histogram, while the lower color bitmap is plotted only for the leakage current range highlighted with a red color.

The graphical user interface for data processing is displayed in Fig. 2.7. The user is free to load any .txt file containing measurement data from previous or currently running measurements. As we have mentioned before, the user can let the program plot any of the three available graphs: IV curve, color bitmap, or histogram. What is more, the user is free

to select dies, subdies, testing voltages, and leakage current ranges for which the graph will be plotted. In practice, the user is free to choose various regions of interest for each graph, e.g., whole wafer, single subdie, single die, specific leakage current range, single testing voltage, etc.

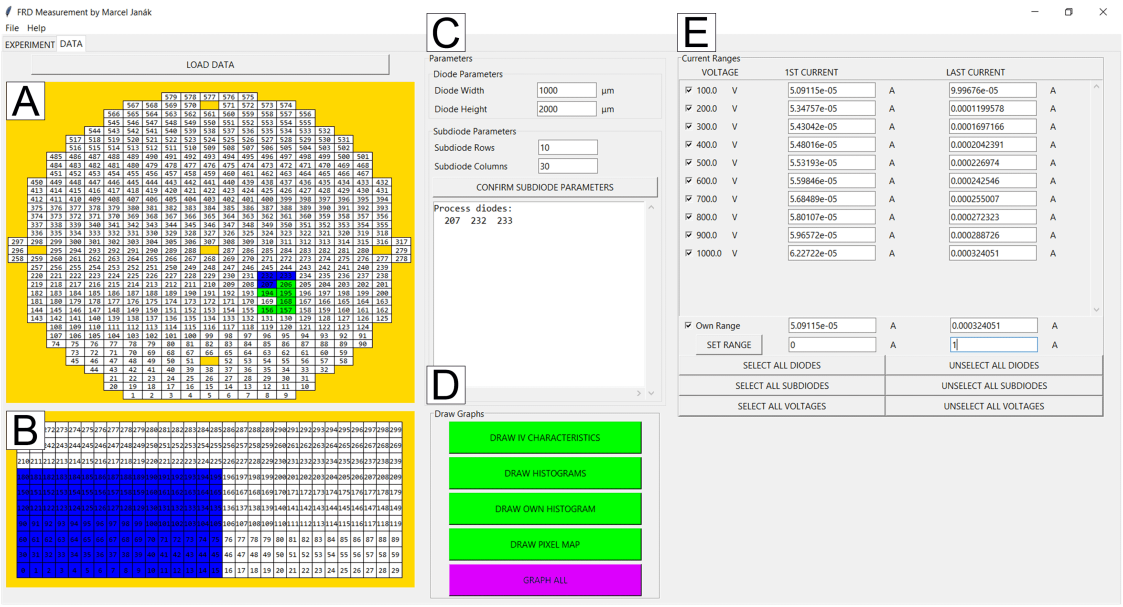

Fig. 2.7: *DATA* part of the control software. A – wafer map for die selection (non-measured dies - white, measured dies – green, dies selected for plotting – blue, background – yellow); B – die map for subdie selection (dies nonselected for plotting – white, dies selected for plotting – blue, background – yellow); C – subdie mesh parameters; D – buttons for plotting IV curve/histogram/own histogram/color bitmap/all graphs at once; E – definition of leakage current ranges and testing voltages for plotting.

Previous software description shows that the program developed as a part of this project makes the whole process of measurement initialization and data processing much easier and less time-consuming. What is more, all programming work carried out during the process of experiment tuning may be incorporated into one well-arranged software. The whole program was written in Python programing language. The software runs in the *Spyder 3.3.6* environment, which is a part of the *Anaconda 2019.10* distribution with *Python 3.7* version. Control PC with measurement software is running on *Windows 10 Home 64-bit* operating system. Communication with SUMMIT 12000 probe station and Keithley 6517B electrometer provides the *PyVISA* package; data graphing provides the *Matplotlib* package. The whole graphical user interface is written in *TkInter* package commands.

2.3. Results

Measurements results are divided into TIGBT (Trench Insulated Gate Bipolar Transistor) and FRD (Fast Recovery Diode) sections.

2.3.1. TIGBT

Since ON Semiconductor unveiled defective TIGBT dies and positions of defects for us, our strategy changed to the reproduction of ON Semiconductor results. This knowledge allowed us to concern test measurements on a smaller area of the wafer containing both defective and good chips. Subdie density was high (1000 subdies per die) since the increasing subdie density increases the probability of precise defect localization. During the process of software testing, we performed a lot of test measurements. Results of the most representative measurement are discussed and displayed below. Good chips are compared with defective ones.

To start with, a difference in leakage currents between defective chips and good chips was significant for all testing voltages. What is more, we were able to observe a characteristic pattern that occurs on every color bitmap at each testing voltage. The characteristic pattern occurs both on defective and good chips but with shifted leakage current values for each subdie. A leakage current shift can be observed on a subdie IV curve graph displayed in Fig. 2.8. Both IV curves come from the equal positions on a defective and a good chip. Unfortunately, the origin of the observed pattern is unknown to us. Correlation between the defect position and areas on the chip with higher leakage currents was not observed. It means that defective chips were successfully revealed; however, defects within chips were not localized.

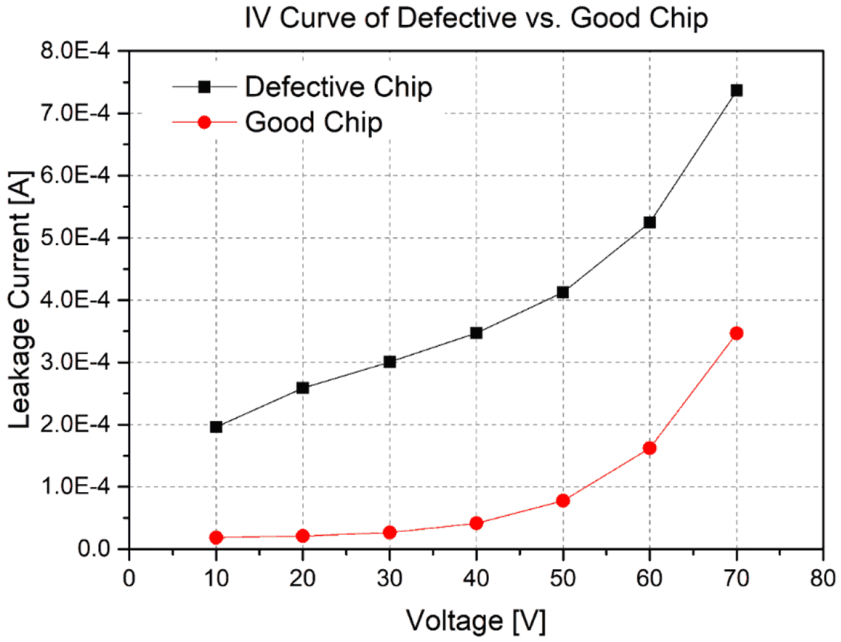

Fig. 2.8: IV curve of one defective chip (black curve) and good chip (red curve). Both IV curves come from equal positions.

In Fig. 2.9, a measurement of two defective and three good TIGBT dies is displayed. Each transistor was fragmentized into a matrix of 31×33 subdies. A red pattern inside each die in Fig. 2.9 represents a gate area of the transistor. This area was not tested (altogether, 73 subdies for each die were skipped). Parameters of voltage sequence are: 10 V first voltage, 10 V voltage step, 70 V last voltage, and 0.5 s time delay. Altogether, ca. 76 000 analytical steps in a ca. 45-hours lasting measurement were performed. The analysis was

performed with a *D07S01V02* scanning mode: whole leakage current test sequence was carried out on each subdie; scanning over subdies was performed in a sawtooth mode; after scanning the whole die, the positioner moved to the next die; scanning over dies was analogous to scanning over subdies. Between each leakage current test sequence was a 15 s pause.

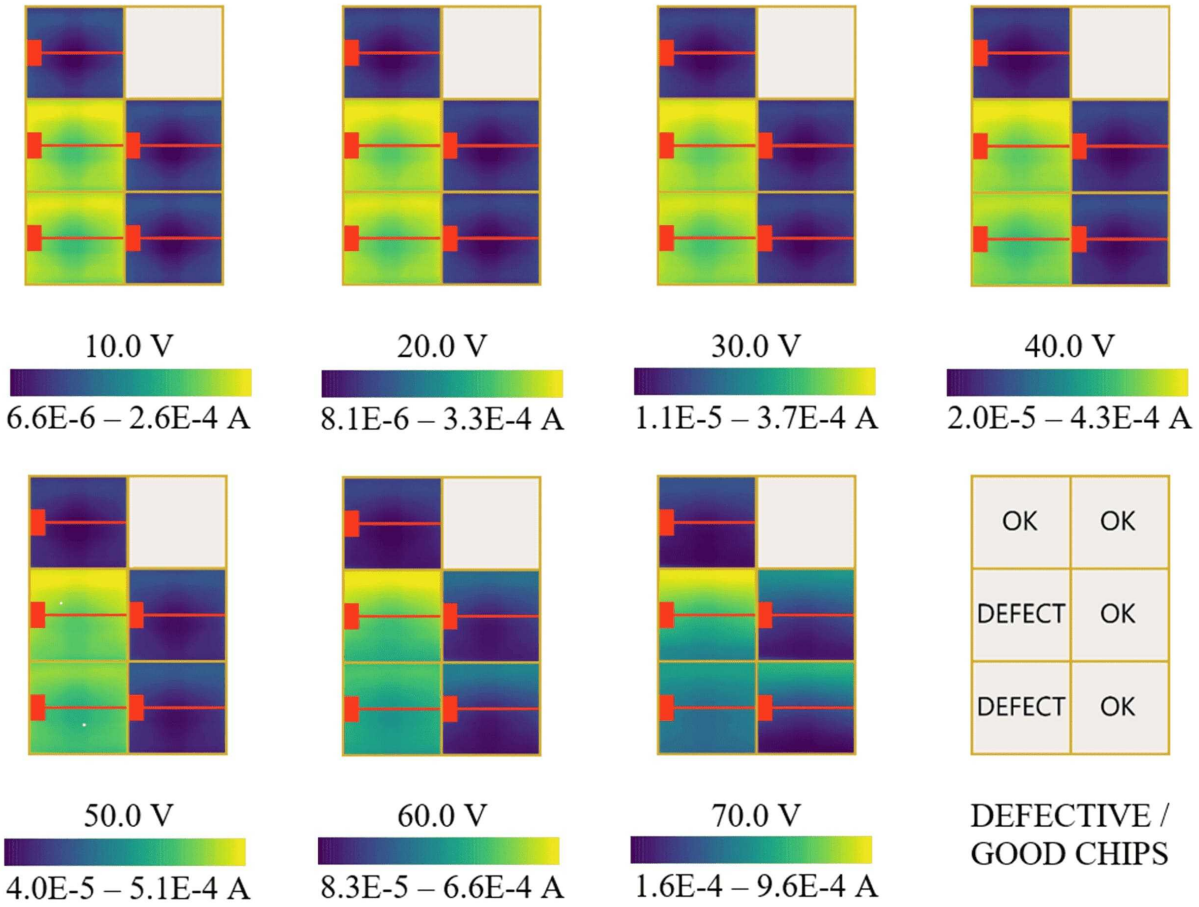

Fig. 2.9: Color bitmaps of defective and good TIGBT dies (the die in an upper right corner was not measured). Each die exhibits the same pattern, i.e., higher current at the borders, lower current in the center.

2.3.2. FRD

The measurement strategy for FRD dies is similar to the measurement strategy for TIGBT dies. ON Semiconductor unveiled defective dies for us; therefore, the analysis focused on a smaller area of the wafer containing both defective and good chips. Each die was fragmentized into a matrix of 10×30 subdies. Even though we have performed several long-lasting measurements, defects could not be localized. On the other hand, we were successful in repetitive observations of characteristic patterns on every die at each testing voltage, see Fig. 2.10. After etching the top alumina passivation layer, a new characteristic pattern was observed, see Fig. 2.11.

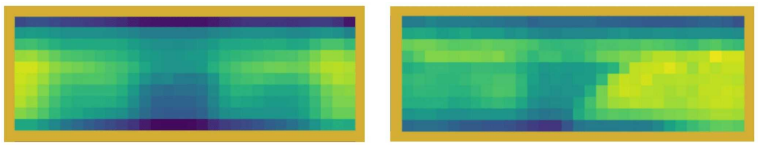

Fig. 2.10: *(left)* A typical pattern observed on every FRD die. *(right)* Deviation from the characteristic pattern.

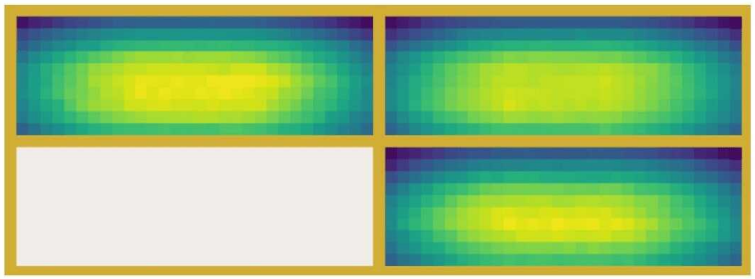

Fig. 2.11: A typical pattern observed on every FRD die with an etched top aluminum passivation layer.

Although the pattern could be observed on every die, some dies exhibited deviation from the characteristic pattern, see, Fig. 2.10. Therefore, dies with patterns deviating from the characteristic pattern were further studied with an optical microscope, which revealed a melted edge of the die, see Fig. 2.12. The edge was melted during test measurements and did not originate from the fabrication.

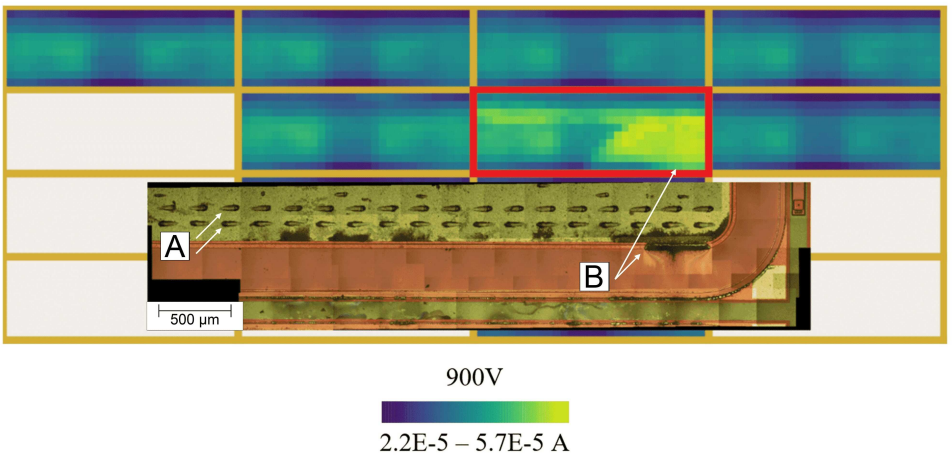

Fig. 2.12: Six FRD dies with a characteristic pattern and one FRD die with a deviated pattern. A light micrograph shows the melted edge of the die. A – a pair of grooves in the aluminum passivation layer created by a pair of probes touching the die surface during analysis; B – melted edge of the die.

Since macroscopic defects displayed in Fig. 2.12 were created during the measurement process, we tried to find out the exact moment of the defect creation, i.e., an analytical step after which the defect appeared. This information could potentially reveal a weak area of the chip. The most effective way to reveal the defect creation was to scan the whole chip area after each analytical step. For this purpose, we enhanced the measurement software with a scanner function. Because of a limited field of view of the SUMMIT 12000

microscope, each scan consists of nine overlapping pictures at different chip positions, see Fig. 2.13. The defect creation was not observed yet.

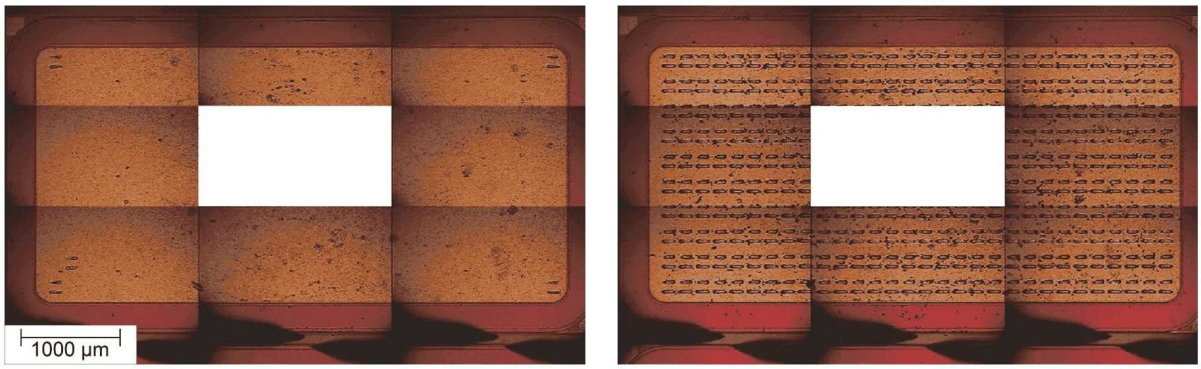

Fig. 2.13: Two different scans of one FRD die. Scan after the first analytical step *(left)*, scan after the last analytical step *(right)*. Scanning is normally performed after each analytical step. Since defects were created only on edges, a middle picture is missing. Dark shades at the bottom of the figure are measurement probes.

3. Dynamic SIMS quantification of Mg dopants in $Al_xGa_{1-x}N$ structures

Due to electronic properties and good thermal stability, multilayered $Al_xGa_{1-x}N$ heterostructures are promising candidates for the commercial production of optoelectronic devices, high-power, and high-frequency electronic devices. The desired performance of $Al_xGa_{1-x}N$ heterostructures is often achieved by introducing various impurities (H, Mg, Si) into selected $Al_xGa_{1-x}N$ layers. Thus, the resulting structure consists of multiple $Al_xGa_{1-x}N$ layers of different widths (typically from 10^0 nm to 10^2 nm), different AlN mole fractions ($x \in \langle 0, 1 \rangle$), and different doping concentrations (typically around 10^{19} at.cm^{-3}). The frequently used fabrication technique for multilayered $Al_xGa_{1-x}N$ heterostructures is metal-organic vapor-phase epitaxy (MOVPE). The concentration of dopants in the growing layer is controlled by the flow of dopant precursors in the reactor. However, desorption of preadsorbed dopants from the reactor walls may cause unwanted doping of later growing layers. Another unwanted phenomenon is the bulk diffusion of dopants at elevated temperatures during the growth or activation treatment. Fine-tuning of the manufacturing parameters, therefore, requires precise characterization of test samples. Due to high sensitivity and good depth resolution, dynamic SIMS (DSIMS) is an ideal method for characterizing doped $Al_xGa_{1-x}N$ heterostructures. The biggest challenge in the quantitative DSIMS analysis of multilayered $Al_xGa_{1-x}N$ heterostructures with varying AlN mole fraction remains a matrix effect that causes hardly predictable relation between the signal of secondary ions and concentration of sputtered species. Therefore, a suitable quantification method for the signal of secondary ions needs to be developed.

CEITEC Nano laboratory cooperates with the ON Semiconductor company on the characterization of multilayered $Al_xGa_{1-x}N$ heterostructures for high electron mobility transistors (HEMT). Typically Mg doped multilayered $Al_xGa_{1-x}N$ heterostructures are characterized by TOF-SIMS instrument TOF.SIMS 5 from the IONTOF company. The first quantification method for H/C/O/Mg dopant concentrations in GaN samples using TOF.SIMS 5 instrument was proposed in the author's bachelor thesis [8]. The proposed method was based on the work of Gu et al. [9,10]; however, doped $Al_xGa_{1-x}N$ calibration samples with higher AlN mole fractions were missing in the bachelor thesis. Therefore, 12 new $Al_xGa_{1-x}N$ calibration samples with $x \in \{0, 0.065, 0.13, 0.26, 0.31, 0.33, 0.42, 0.6, 0.7, 0.9, 1\}$ were prepared by Mg ion implantation at the Uppsala University (Sweden), and extended calibration curves are presented. While Gu et al. [9, 10] employed the SIMS instrument equipped with a magnetic sector, our work is aimed at the SIMS instrument equipped with a time-of-flight mass analyzer. Otherwise, the methods do not differ significantly.

3.1. Mg doped $Al_xGa_{1-x}N$

$Al_xGa_{1-x}N$ is an III-V semiconductor formed by bonding a group III aluminum (Al) and gallium (Ga) with a group V nitrogen (N). Depending on the AlN mole fraction, either binary gallium nitride (GaN), binary aluminum nitride (AlN), or various ternary aluminum gallium nitride alloys ($Al_xGa_{1-x}N$) may be formed. The entire composition

range between GaN and AlN is allowed [11]. The thermodynamically stable phase of $Al_xGa_{1-x}N$ compounds at normal temperatures and atmospheric pressure is a wurtzite structure [12]. The symmetry of the wurtzite structure causes spontaneous polarization and allows piezoelectric polarization upon external strain [13]. Lattice parameters and bandgap structure of $Al_xGa_{1-x}N$ alloys are tunable between the values of two end members, namely GaN and AlN, by AlN mole fraction [11] [14]. 3.43 eV direct bandgap of GaN and 6.11 eV direct bandgap of AlN indicate that $Al_xGa_{1-x}N$ compounds are suitable for the fabrication of ultraviolet and deep-ultraviolet optoelectronic devices operating between 200–365 nm wavelengths, e.g., laser diodes (LD) or light-emitting diodes (LED). Carrier mobility depends on doping concentration and defect concentration caused primarily by the lattice constant mismatch between neighboring layers. Common intentional impurities in $Al_xGa_{1-x}N$ compounds are Si and Mg. Si donors with typical concentrations of 10^{17}–10^{19} at.cm^{-3} are used to create n-type regions, while Mg acceptors with typical concentrations around 10^{18} at.cm^{-3} are used to form p-type regions [9]. Common unintentional impurities introduced into the material from precursors and reactor impurities during chemical vapor deposition (CVD) are O, which acts as a shallow donor, and C, which acts either as acceptor or donor. H doping results in neutralization of dopants and, therefore, higher resistivity.

An extensive review of $Al_xGa_{1-x}N$ metal-organic chemical vapor deposition (MOCVD) growth was published by Tang et al. [12]. Typical precursors for the growth of $Al_xGa_{1-x}N$ heterostructures are $Al(CH_3)_3$, trimethylaluminum (TMAl), $Ga(CH_3)_3$, trimethylgallium (TMGa), and NH_3, which are introduced into the reactor chamber together with H_2 and N_2 carrier gasses. Mg doping is provided by adding bis-(cyclopentadienyl)-magnesium (Cp_2Mg) precursor into the gas flow. Gas-phase precursors introduced into the reaction chamber chemically react to form growth precursors. After adsorption and subsequent diffusion to the growing sites on the substrate, matrix and dopant materials are incorporated into the growing film. Reaction by-products are released from the surface and carried by the flow away from the reactor. In terms of defect densities, the quality of multilayered $Al_xGa_{1-x}N$ heterostructures depends on the lattice constant and thermal expansion difference between the substrate and growing layer. Therefore an ideal substrate for $Al_xGa_{1-x}N$ heterostructures is highly crystalline AlN single-crystal, typically growing on Si(111), silicon carbide (SiC(0001)), or sapphire (Al_2O_3) at temperatures around 2000 °C. The substrate temperature during $Al_xGa_{1-x}N$ growth is usually kept around 1050 °C, which is sufficient for NH_3 decomposition and surface mobility of strongly bonding Al precursors.

After the fabrication of Mg doped $Al_xGa_{1-x}N$ structures, an activation treatment needs to be performed in order to obtain higher p-$Al_xGa_{1-x}N$ conductivity. The generation of holes is usually carried out by a low-energy electron beam irradiation treatment (LEEBI), a microwave treatment, and thermal annealing treatment [15]. However, due to the relatively high activation energy of Mg acceptors in $Al_xGa_{1-x}N$ structures ranging from 170 meV for GaN to 510 meV for AlN, the efficiency of conventional activation procedures remains low [16]. Mg concentration of $1 \cdot 10^{19}$ at.cm^{-3} typically corresponds to around a hundred times lower concentration of free holes [17]. Activation energy may be lowered by techniques of Mg-Zn, Mg-Si, Mg-O co-doping, delta doping, or superlattice doping [16]. H passivation is another phenomenon decreasing the free hole concentration in Mg doped $Al_xGa_{1-x}N$ structures. H impurities introduced during MOCVD growth are typically removed by annealing in N_2 surrounding atmosphere at temperatures below

850 °C or by rapid thermal annealing [18]. Improper activation treatment may enhance unwanted diffusion of Mg dopants into adjacent layers of $Al_xGa_{1-x}N$ heterostructures. According to Köhler et al. [19], the activation barrier for Mg diffusivity in GaN reaches 5.0 eV, while the activation barrier for Mg diffusivity in $Al_{0.1}Ga_{0.9}N$ reaches 5.2 eV.

Comparison of p-GaN metal-oxide semiconductor field effect transistors (MOSFET) with AlGaN/GaN high electron mobility transistors (HEMT) shows that HEMTs exhibit much lower channel on-resistivity than widely used MOSFETs [20]. A huge difference in mobility stems from the fact that conduction electrons in p-GaN MOSFETs occupy the same space as ionized impurities and, therefore, get easily scattered. On the other hand, conductive electrons in HEMTs are localized in two dimensional electron gas (2DEG) at the undoped interface of the AlGaN/GaN heterostructure. Enhanced electron mobility and high thermal stability make AlGaN/GaN HEMTs excellent candidates for high switching frequency power applications. Due to the spontaneous polarization of wurtzite AlGaN/GaN structures, 2DEG is formed at the interface even at zero external voltages. Therefore, AlGaN/GaN HEMTs are normally ON devices, see Fig. 3.1a. However, for the simplicity of electric circuit designs, normally OFF devices are usually preferred. Transformation of normally ON AlGaN/GaN HEMT into normally OFF devices may be achieved by adding Mg doped GaN layer causing carrier depletion from 2DEG [21]. The final structure is composed of a substrate, GaN channel layer, AlGaN barrier layer, a p-GaN cap layer, and a metallic gate electrode, see Fig. 3.1b. The gate-source voltage varies 2DEG channel density and thereby directly controls the source-drain current flow. A comparison of conduction band energy diagrams for p-GaN/$Al_{0.15}Ga_{0.75}N$/GaN structure and $Al_{0.15}Ga_{0.75}N$/GaN structure is displayed in Fig. 3.1c.

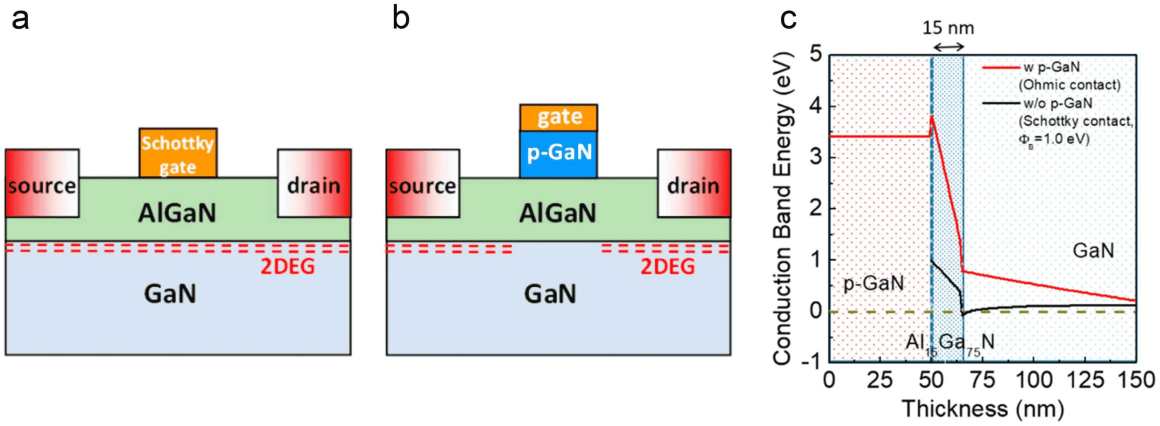

Fig. 3.1: a: schematics of normally ON AlGaN/GaN HEMT, b: schematics of normally OFF p-GaN/AlGaN/GaN HEMT, c: comparison of conduction band energy diagram of normally ON $Al_{0.15}Ga_{0.75}N$/GaN HEMT (black) and normally OFF p-GaN/$Al_{0.15}Ga_{0.75}N$/GaN HEMT (red). Taken from [21].

3.2. Depth profiling

Depth profiling by TOF-SIMS is a destructive process periodically alternating between the analysis of surface composition and material sputtering, providing penetration into depth, see Fig. 3.2. The output of the DSIMS measurement is the signal of secondary ions as a function of sputter time. In order to obtain quantitative information about the sample

composition, sputter time needs to be converted into depth, and the signal of secondary ions needs to be converted into concentration. Despite excellent sensitivity (10^1 ppb) and good depth resolution (10^0 nm), the quantification of depth profiles is exceedingly difficult due to the strong matrix effect. In DSIMS measurements, the term matrix effect denotes a hardly predictable influence of any element, whose concentration in bulk exceeds one atomic percent, on the yield of secondary ions. The most reliable method for quantifying impurity concentrations below one atomic percent in a known matrix is a comparative RSF (relative sensitivity factor) method. In the beginning, the RSF coefficient for a certain impurity in a known matrix is determined by measuring the calibration sample. Then, the RSF coefficient is used in calculations converting the intensity of the impurity signal from the sample with identical matrix composition into concentration.

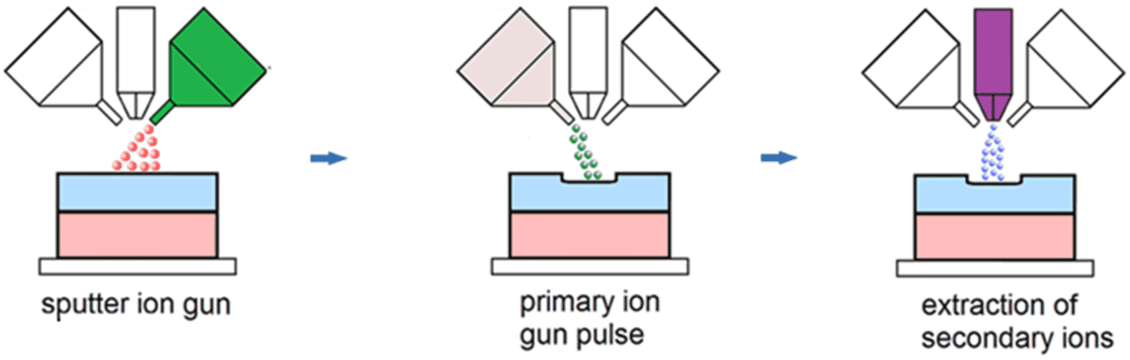

Fig. 3.2: Scheme illustrating depth profiling by DSIMS method. Taken from [22].

Before a detailed RSF method description, pitfalls of depth profiling will be discussed briefly. While in SSIMS measurements, about 1–10% of the upper 2 nm of the surface are damaged by impinging primary ions, significant surface damage induced during material sputtering in DSIMS measurements brings several phenomena which need to be considered when designing experiments [4]. The most significant phenomenon affecting the depth resolution of DSIMS measurements is the effect of atomic mixing. The mixing of near-surface atoms and their penetration into greater depths results from the knock-on of atoms in collision cascades caused by energetic ion impact. Interfaces in depth profiles then appear broad. In the worst case, periodic thin layer structures disappear entirely. Atomic mixing can be minimized by decreasing the angle between the ion beam and sample surface, decreasing the energy of impinging ions, or increasing the ion mass to charge ratio [4]. Another phenomenon lowering the depth resolution of DSIMS measurements is a crater edge effect. The crater edge effect describes the detection of secondary ions originating from crater edges, i.e., the detection of secondary ions from shallower layers. The suppression of the crater edge effect may be achieved by optical or electronic gating, i.e., filtering out the signal from near edge areas. In TOF-SIMS instruments, the crater edge effect may be removed by sputtering a larger crater than the analyzed area. The influence of surface topography on depth resolution is referred to as the crater base effect. Since surface sputtering follows the surface topography, dust particles, scratches, voids, or steps cause detection of secondary ions from various depths, resulting in worsened depth resolution. On the other hand, smooth surface, however not parallel

with subsurface interface, causes spatial reaching of the interface at different times, and therefore the interface appears broad. Steps on the crater base may also be created due to different sputtering rates of various crater areas, i.e., preferential sputtering. This phenomenon is particularly significant on polycrystalline samples where preferential sputtering of various grain orientations causes surface roughening. Surface roughening may be suppressed by sample rotation during the analysis. In general, the crater base effect may be suppressed by proper sample preparation (removal of dust particles, preparation of surfaces parallel with interfaces, etc.). In some cases, the crater base effect may be revealed by plotting a 3D model of the measured sample.

3.2.1. The RSF method

Theoretically, the signal of secondary ions I_D of the element D in DSIMS measurements may be quantified based on the current of primary ions I_P, sputter yield Y_D of the element D, ionization probability $P_\mathrm{D}^{\pm}$ of the element D, and the instrument transmissivity f [9]:

$$C_\mathrm{D} = \frac{I_\mathrm{D}}{I_\mathrm{P} \cdot Y_\mathrm{D} \cdot P_\mathrm{D}^{\pm} \cdot f}. \tag{3.1}$$

C_D denotes the concentration of the element D. Sputter yield determines the number of atoms sputtered per incident primary ion; ionization probability determines the fraction of ionized atoms out of sputtered atoms; instrument transmissivity determines the fraction of detected ions out of ionized atoms. In real experiments, I_D, I_P, Y_D, and f may be easily measured or calculated. On the other hand, ionization probability $P_\mathrm{D}^{\pm}$, strongly depending on the matrix composition and primary ions, is hardly determinable. Therefore, practical applications of Eq. (3.1) are considerably limited.

As already outlined, the RSF method is a widely used method for concentration quantification in DSIMS measurements. According to the RSF method, concentration C_D of the element D is calculated based on the secondary ion signal I_D of the element D, the secondary ion signal I_M of the matrix element M, concentration C_M of the matrix element M, and relative sensitivity factor RSF [4]:

$$C_\mathrm{D} = RSF \cdot \frac{I_\mathrm{D} \cdot C_\mathrm{M}}{I_\mathrm{M}}. \tag{3.2}$$

The signal of secondary ions I_D and I_M is determined by DSIMS measurement, while the product $RSF \cdot C_\mathrm{M}$ is determined by the measurement of calibration samples with known concentration C_D. The matrix composition of the calibration sample is identical to the matrix composition of the examined sample. Since elements with concentrations exceeding ca. 1% of the bulk concentration significantly affect the signal of matrix elements, the concentration of element D in examined sample and calibration sample cannot exceed 1% of the bulk concentration. RSF can be then calculated according to the following equation [9]:

$$RSF = \frac{C_\mathrm{D} \cdot I_\mathrm{M}}{I_\mathrm{D} \cdot C_\mathrm{M}} = const., \quad \text{for } 0.01 \cdot C_\mathrm{M} \gtrsim C_\mathrm{D} \wedge C_\mathrm{M} = const. \tag{3.3}$$

Analytical conditions during the measurement of the calibration sample should differ minimally from the analytical conditions during the measurement of the examined sample.

Another way of RSF determination is a DSIMS depth profiling of calibration samples prepared by ion implantation. Element D implanted into the sample with known matrix composition forms an implantation profile, and RSF is then calculated via [4]:

$$RSF = \frac{\delta \cdot I_{\mathrm{M}} \cdot C \cdot t}{d \sum I_{\mathrm{D}} - d \sum I_{\mathrm{DB}} \cdot C}, \tag{3.4}$$

where δ denotes implantation dose, I_{M} denotes the secondary ion signal of the matrix element M, C denotes the number of analytical cycles, t denotes the analysis time, d denotes crater depth, I_{D} denotes the secondary ion signal of the element D, and I_{DB} represents the background signal. The oxygen enhanced I_{D} signal during initial analytical cycles needs to be omitted when calculating RSF via Eq. (3.4).

A typical implantation profile is displayed in Fig. 3.3. The energy of implanted ions should be high enough to minimize the fraction of backscattered ions from the sample surface during the implantation. At the same time, the implantation profile needs to be localized close to the sample surface to minimize the time necessary for a full profile DSIMS measurement. The concentration of the majority of implanted ions should exceed the detection limit of the instrument, but at the same time, maximal concentration in the implantation peak has to surpass 1% of the bulk concentration. Implantation parameters are usually determined by simulations in the TRIM software. Typical input parameters for TRIM[1] simulations are ion type, ion energy, implantation angle, and target composition (stoichiometry, density, etc.). The output of the simulation is an implantation profile plot. Y-axis conversion to concentration is obtained after multiplication by implantation dose ([at.cm^{-2}]). The implantation peak position is given by ion energy.

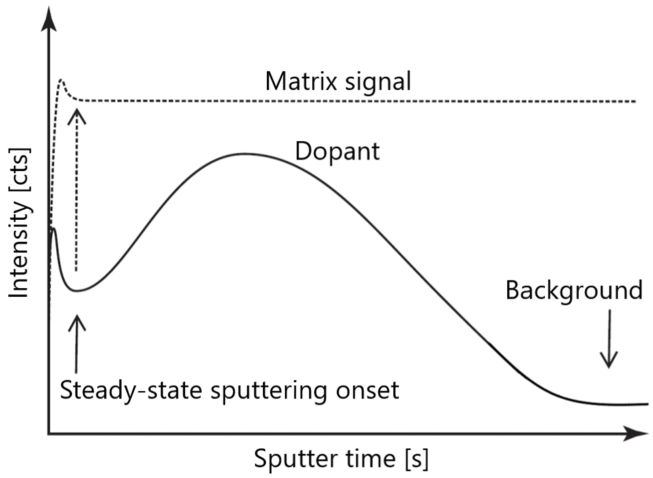

Fig. 3.3: Typical DSIMS depth profile of an implanted calibration sample used for determination of RSF coefficient. Adapted from [4].

3.3. Experiment

The experimental part is divided into the preparation of calibration samples and their subsequent depth profiling by the TOF.SIMS 5 instrument.

[1] the Transport of Ions in Matter

3.3.1. Sample preparation

For quantification of Mg concentration in various $Al_xGa_{1-x}N$ samples measured by TOF.SIMS 5 instrument, a set of 12 calibration samples was prepared. Since the quantification is based on the RSF method, calibration samples were prepared by ion implantation. Pure $Al_xGa_{1-x}N$ samples were available in the laboratory; therefore, our tasks were reduced to the sample preparation for ion implantation. Ion implantation was performed by a 350 kV high-current implanter at the Tandem Laboratory of Uppsala University (Sweden), operated by Sotirios Droulias. Matrix composition of calibration samples covers the whole AlN mole fraction range between GaN and AlN: $x \in \{0, 0.065, 0.13, 0.26, 0.31, 0.33, 0.42, 0.6, 0.7, 0.9, 1\}$. The minimal thickness of $Al_xGa_{1-x}N$ layers reaches 300 nm. $Al_xGa_{1-x}N$ layers were grown on AlN substrate, which was grown on Si substrate.

Parameters for ion implantation were chosen by TRIM simulations. The optimal implantation peak position was found for Mg ions with an energy of 75 keV. The Mg implantation peak of GaN sample is located at 75 nm depth, Mg implantation peak of AlN sample is located at 103 nm depth. The optimal implantation dose was determined to $3.0 \cdot 10^{14}$ at.cm^{-2}. Maximal Mg concentration in the implantation peak ranges from $3.0 \cdot 10^{19}$ at.cm^{-3} for GaN sample to $3.2 \cdot 10^{19}$ at.cm^{-3} for AlN sample. Atomic density of GaN reaches $8.9 \cdot 10^{22}$ at.cm^{-3} and atomic density of AlN reaches $9.58 \cdot 10^{22}$ at.cm^{-3} [23]. That implies that maximal Mg concentration does not exceed 1% of the bulk concentration. TRIM simulated Mg implantation profiles in all 12 $Al_xGa_{1-x}N$ calibration samples are displayed in Fig. 3.4. All simulations were performed for a typical implantation angle of 7°, which prevents ions from unwanted channeling.

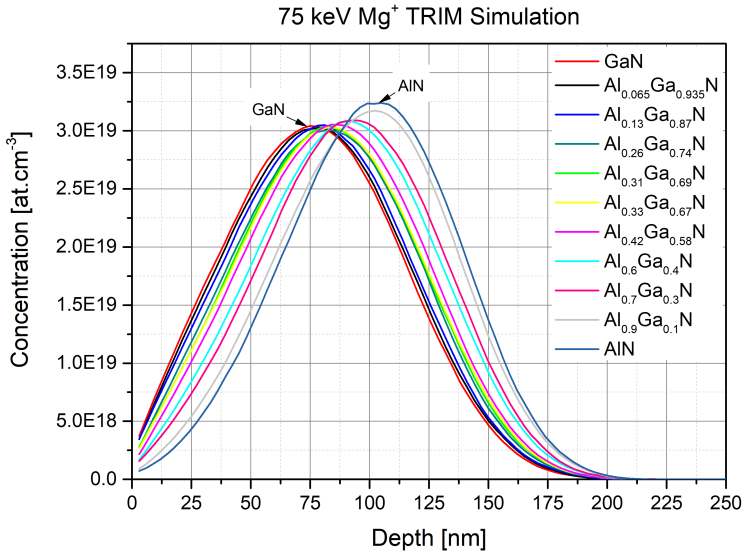

Fig. 3.4: TRIM simulated Mg implantation profiles in all 12 $Al_xGa_{1-x}N$ calibration samples.

After finding optimal implantation parameters, all 12 1×2 cm $Al_xGa_{1-x}N$ samples were implanted at once by the high-current implanter. After that, all 12 Mg implanted $Al_xGa_{1-x}N$ calibration samples were inserted into the TOF.SIMS 5 sample holder and prepared for DSIMS depth profiling. TOF.SIMS 5 sample holder with $Al_xGa_{1-x}N$ calibration samples is displayed in Fig. 3.5.

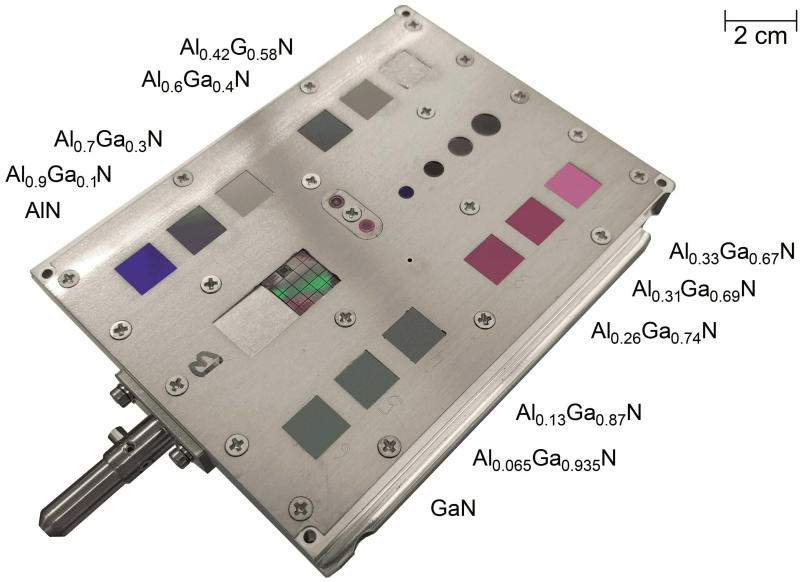

Fig. 3.5: TOF.SIMS 5 sample holder with all 12 $Al_xGa_{1-x}N$ calibration samples.

3.3.2. Depth profiling

Quantification of dopant concentration using the RSF method requires identical conditions of analysis for calibration samples and examined samples. The highest accuracy is achieved when both types of samples are analyzed in one run. Therefore, it is necessary to find such instrument settings that provide sufficient depth resolution and measurement sensitivity in the shortest analysis time possible. TOF.SIMS 5 instrument settings in our work allowed the analysis of ca. 300 nm thick AlGaN layer per 1 hour. Although the analysis of 12 $Al_xGa_{1-x}N$ calibration samples takes more than half a day, analysis time in real experiments may be shortened since not all 12 calibration samples are necessary. Calibration samples with specific AlN mole fraction, necessary for the analysis of full $Al_xGa_{1-x}N$ range, will be specified based on our results, see Sec. 3.4.

TOF.SIMS 5 depth profiling of Mg doped $Al_xGa_{1-x}N$ calibration samples was provided by a bismuth primary ion gun and oxygen sputter gun. An electron flood gun compensated sample charging during the analysis. Since Mg atoms exhibit the highest yield of positive ions in the presence of oxygen, the main chamber was flooded with oxygen to the pressure of $1 \cdot 10^{-5}$ mbar. The enhanced yield of positive ions was also the reason for the selection of the oxygen sputter gun. Electrodes in the reflectron-equipped time-of-flight mass spectrometer were set to voltages allowing detection of positive ions. The analysis of the crater base was performed on the area of 100×100 µm by 30 keV Bi^+ ions. 128×128 points were scanned in random mode. Sputtering the area of 250×250 µm by 2 keV O_2 ions ensured the elimination of the crater edge effect. The angle between the primary ion gun and the surface normal, as well as the angle between the sputter gun and the surface normal, was fixed to 45°. The EDR[2] unit had to be used for aluminum (Al^+) and gallium (Ga^+) signals; otherwise, the signals would be saturated.

[2]extended dynamic range

3.4. Results

The results of TOF.SIMS 5 depth profiling of Mg doped $Al_xGa_{1-x}N$ calibration samples is divided into three parts. In the first part, data for quantification of depth scale are presented. In the second part, two graphs for the quantification of matrix species are displayed. The last part shows the RSF – x graph, which is necessary to quantify Mg concentration in various $Al_xGa_{1-x}N$ layers.

3.4.1. Quantification of depth scale

Quantification of depth scale is based on the position of implantation peaks simulated by TRIM software. The graph showing the sputter rate, i.e., the ratio of simulated Mg peak position and measurement time necessary for reaching maximal Mg signal, as a function of AlN mole fraction, is displayed in Fig. 3.6. In agreement with Gu et al. [10], sputter rate decreases with increasing AlN mole fraction. Measured data were fitted with the fourth degree polynomial.

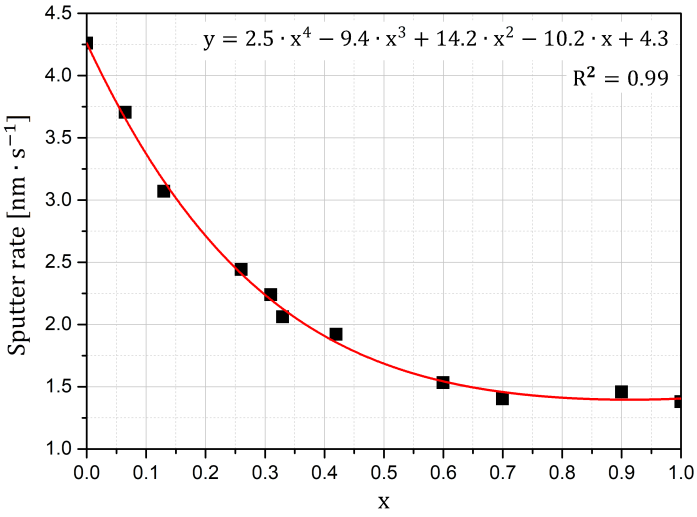

Fig. 3.6: Sputter rate as a function of AlN mole fraction x. The graph is used for depth quantification of AlGaN samples ranging from GaN to AlN.

3.4.2. Quantification of matrix species

According to Gu et al. [10], two graphs for the quantification of matrix species are necessary. Both graphs plot the ratio of signals of matrix elements ($I(Al^+)/I(Ga^+)$, $I(Ga^+)/I(Al^+)$) as a function of the AlN mole fraction ratio ($x/1-x$, $1-x/x$). The first graph determines the matrix composition of AlGaN samples ranging from GaN to $Al_{0.6}Ga_{0.4}N$, see Fig. 3.7; the second graph determines the matrix composition of AlGaN samples ranging from $Al_{0.13}Ga_{0.87}N$ to AlN, see Fig. 3.8. Since the signal ratio in both graphs is linearly proportional to the AlN mole fraction ratio, and both graphs cross the y-axis in zero, the analysis of one calibration sample with $x \in \langle 0.13, 0.6 \rangle$ is sufficient. Both graphs agree

with measurements of Gu et al. [10] and measurements presented in the author's bachelor thesis [8].

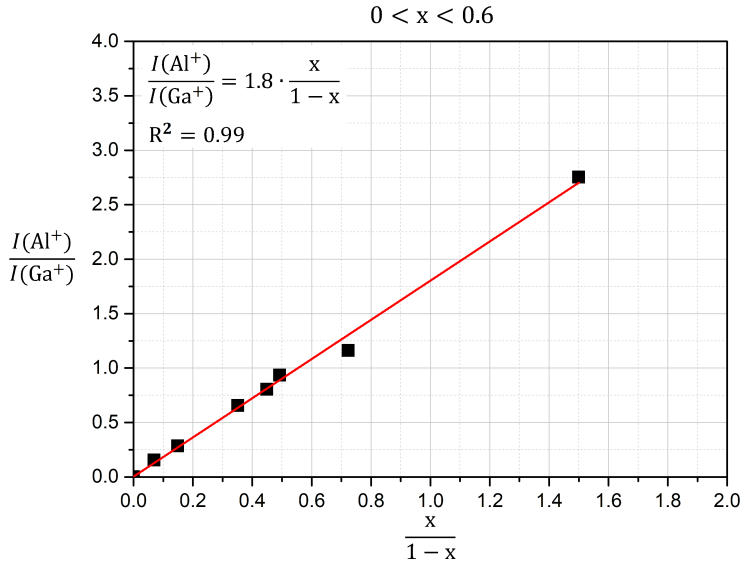

Fig. 3.7: Ratio of signals of matrix elements as a function of AlN mole fraction ratio. The graph is used for the quantification of matrix species in AlGaN samples ranging from GaN to $Al_{0.6}Ga_{0.4}N$.

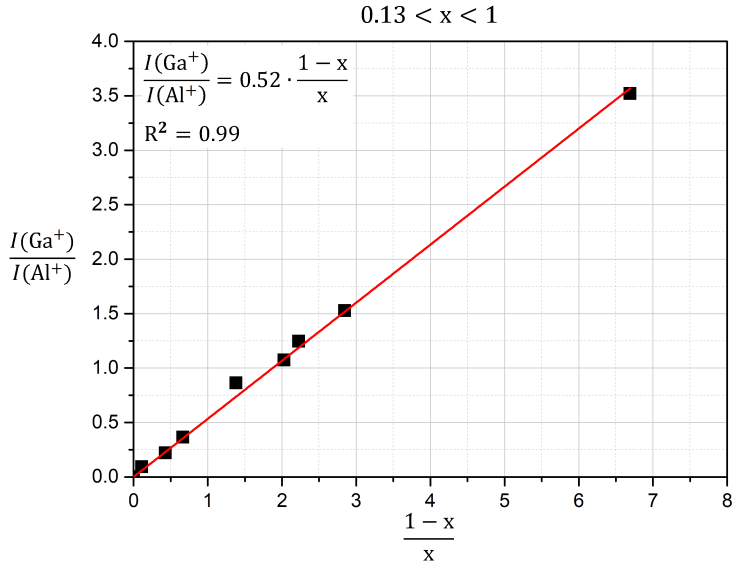

Fig. 3.8: Ratio of signals of matrix elements as a function of AlN mole fraction ratio. The graph is used for the quantification of matrix species in AlGaN samples ranging from $Al_{0.13}Ga_{0.87}N$ to AlN.

3.4.3. Quantification of Mg dopants

After finding the right matrix composition of the examined sample (see Sec. 3.4.2), an appropriate *RSF* coefficient needs to be selected to quantify the signal of Mg dopants (see

Eq. (3.2)). A graph showing *RSF* as a function of AlN mole fraction x is displayed in Fig. 3.9. *RSF* coefficients in Fig. 3.9 were calculated by the SurfaceLab 6 software from the IONTOF company, which is used for TOF.SIMS 5 measured data processing. Calculations are based on Eq. (3.4); therefore, the user needs to quantify the depth scale, select the matrix reference signal, define the implantation profile depth range, and input the ion implantation dose. Fig. 3.9 shows two curves for two matrix reference signals, namely Al^+ and Ga^+. Ga reference is used for Mg quantification in AlGaN samples ranging from GaN to $Al_{0.7}Ga_{0.3}N$; Al reference is used for Mg quantification in AlGaN samples ranging from $Al_{0.26}Ga_{0.74}N$ to AlN. Unlike Gu et al. [10], who observed exponential correlation of *RSF* with AlN mole fraction x, we observed rather linear proportionality of *RSF* to AlN mole fraction x. According to our results, the analysis of three samples for RSF – x graph construction would be sufficient. We suggest the measurement of Mg doped GaN, AlN calibration samples and one $Al_xGa_{1-x}N$ $x \in \langle 0.26, 0.6 \rangle$ calibration sample.

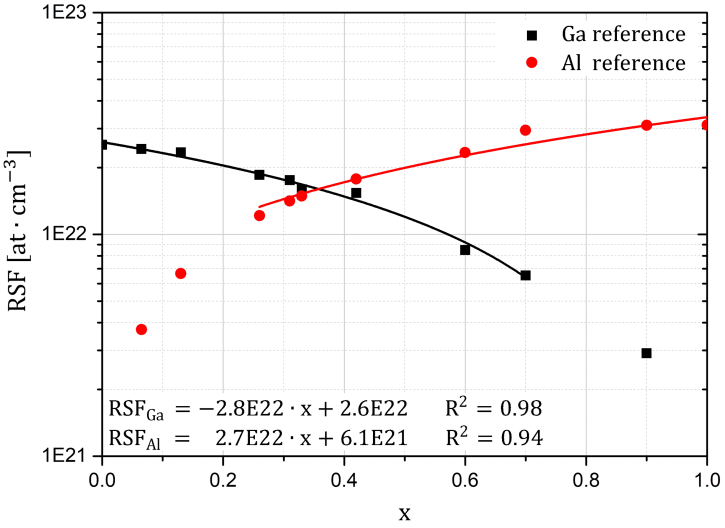

Fig. 3.9: *RSF* as a function of AlN mole fraction x. The black curve is used for Mg quantification in AlGaN samples ranging from GaN to $Al_{0.7}Ga_{0.3}N$; the red curve is used for Mg quantification in AlGaN samples ranging from $Al_{0.26}Ga_{0.74}N$ to AlN.

4. Static SIMS Monitoring of Catalytic CO Oxidation to CO_2 Over Platinum Surfaces

Industrial development in recent decades has raised the importance of CO elimination from various gas product streams. Incomplete fossil fuel combustion in the production and transportation sector are the primary sources of atmospheric CO. Increased CO concentrations in living environments cause oxygen deprivation of the human body vital organs [24]. CO molecules are also an unwanted byproduct of hydrogen production from natural gas or other carbon feedstocks (e.g., methanol). Excessive CO feeds to hydrogen fuel cells may cause decay in their electro-generation performance [25–27].

Platinum group metals (Ru, Rh, Pd, Ir, Pt) are the most widespread catalysts for CO oxidation by O_2 [28]. The role of the catalyst is to increase the reaction rate by lowering activation barriers. Nanomaterial-based catalysts of different structures (e.g., nanoparticles, nanorods, shell-core nanocomposites), supported on various materials (e.g., silica, aluminum oxide) and promoted by various substances (e.g., alkali metals) are investigated by many research groups in order to enhance CO conversion rates [29]. Although the catalyst remains throughout the reaction unconsumed, structural changes like catalyst sintering, surface faceting, or surface poisoning in long-term runs lead to the catalytic activity lowering. Therefore, reaction mechanism and deactivation mechanism understanding is crucial for designing stable CO catalytic converters with high CO conversion rates.

Many conventional surface science techniques may be employed for heterogeneous catalysis research. The selection of proper techniques is based on the research objectives. Depending on requirements for determining chemical composition, determining crystallographic structure, requirements for reaching a high lateral resolution or high temporal resolution, one may choose any of the X-ray, infrared, electron beam, ion beam, or scanning probe microscopy techniques. Particularly advantageous is a combination of several methods in operando experiments, which allows the identification of various catalytic regimes at industrially relevant conditions. The most advanced studies nowadays employ in-situ synchrotron-based X-ray [30] or in-situ environmental transmission electron microscopy (ETEM) [31] techniques.

Our study's objective is the dynamics of catalytic CO oxidation over platinum polycrystalline microstructures at high vacuum pressures ($\sim 10^{-5}$ mbar). In-situ scanning electron microscopy (SEM) and in-situ static secondary ion mass spectrometry (SSIMS) were employed for the real-time observation of gas-phase- and temperature-induced processes on platinum surfaces. Elemental composition changes observed by in-situ SSIMS were compared with work function changes observed by in-situ SEM. Our research demonstrates the abilities of in-situ SSIMS as a powerful technique for the real-time monitoring of surface composition in a flow reactor under fixed conditions. Spatiotemporal patterns of varying surface coverages were observed during distinct catalyst regimes in both instruments.

4.1. Introduction to catalysis

Catalyst is a substance that facilitates chemical reactions via a reaction pathway with lowered activation energy barriers. The reaction may proceed in both directions, and the catalyst presence does not affect the thermodynamic equilibrium of the reaction. What the catalyst affects is the speed at which the reaction reaches its equilibrium. When the reaction products are released, the catalyst regenerates into its original state and may be used repeatedly. If the reactant and catalyst phases match, we talk about *homogeneous catalysis*. If their phases do not match, typically gaseous reactants and solid catalysts, we talk about *heterogeneous catalysis*. *Biocatalysis* denotes chemical processes in living cells catalyzed by enzymes. In this section, key terms and fundamental concepts related to heterogeneous catalysis will be explained.

4.1.1. Industrial applications

If we look back to history, the term *catalysis* was used for the first time to identify accelerated reactions in 1835 by J. J. Berzelius [32]. The first explanation of this phenomenon came in 1900 by W. Ostwald, who proposed that "A catalyst is a substance which affects the rate of a chemical reaction without being part of its end products" [33]. The boom in utilizing catalysis for industrial purposes started at the beginning of the 20^{th} century and continues. The global catalyst market size was estimated at 35 billion USD in 2019, and it is expected to reach 48 billion USD by 2027 [34]. 72% of the total market value in 2019 was assigned to heterogeneous catalysis. Its predominance over homogeneous catalysis lies in the simplicity of product separation from catalysts. Nowadays, heterogeneous catalysis is the backbone of the fertilizer industry, petrochemical industry, and chemical synthesis. Its importance is also significant for the food industry, energy science, and environmental science. Major industrial processes utilizing heterogeneous catalysis nowadays are the Haber-Bosch process of ammonia production (Fe_3O_4 catalysts) [35], the Fischer-Tropsch process of liquid hydrocarbons production (Co/Fe catalysts) [36], syngas-to-methanol conversion ($Cu/ZnO/Al_2O_3$ catalysts) [37], and catalytic cracking in the oil industry (clay catalysts) [38]. Ecological importance has carbon dioxide hydrogenation to methanol, which would allow the global carbon cycle to close [39].

4.1.2. Reaction thermodynamics and kinetics

For further explanation, let us consider a typical chemical reaction:

$$\mathrm{m\,A} + \mathrm{n\,B} \leftrightarrows \mathrm{p\,C} + \mathrm{q\,D}, \tag{4.1}$$

where reactants A, B with stoichiometric coefficients m, n combine to form products C, D with stoichiometric coefficients p, q. In this process, chemical bonds of reactants are broken, while new chemical bonds of products are formed.

A *reaction pathway* is a free energy profile along reaction coordinates. In general, reaction coordinates represent the progress of the reaction. Specifically, reaction coordinates may represent geometric parameters of simple reactions (e.g., bond length, bond angle) or non-geometric parameters of complex reactions (e.g., bond order). The profile starts at the free energy of reactants and ends at the free energy of products. Local maxima along the reaction pathway denote *transition states*, i.e., activation barriers; local minima

denote the existence of *reaction intermediates*.

The *reaction spontaneity* at constant temperature T and pressure p is given by the Gibbs free energy change ΔG between reactants (G_{R}) and products (G_{P}) [40]:

$$\Delta G = G_{\mathrm{P}} - G_{\mathrm{R}} = \Delta H - T\Delta S, \quad p, T = const. \tag{4.2}$$

Taking the enthalpy change ΔH, the entropy change ΔS, and system temperature T into account, the Gibbs free energy lowering increases the system stability. Therefore, a reaction with a negative Gibbs free energy change – an *exergonic reaction* – proceeds spontaneously. On the other hand, a reaction with a positive Gibbs free energy change – an *endergonic reaction* – requires energy to be driven. A negative enthalpy change denotes an *exothermic reaction*, which releases the heat; a positive enthalpy change denotes an *endothermic reaction*, which absorbs the heat. It is important to remind here that the catalyst does not change the free energies of reactants and products; however, the catalyst changes the reaction speed, i.e., the reaction rate, by activation barrier lowering. A rate equation [41]:

$$r = k\,[\mathrm{A}]^{\alpha}\,[\mathrm{B}]^{\beta}\,, \tag{4.3}$$

which links reactant concentrations [A], [B] with the rate coefficient k and partial reaction orders α, β, enumerates the reaction rate at a given time. Partial reaction orders represent the relation between reactant concentration and the reaction rate. The overall reaction order, which is the sum of partial orders for each reactant, needs to be determined experimentally. The *reaction coefficient* k may be determined either empirically by the Arrhenius equation or non-empirically by the Eyring equation [41]:

$$k = A \cdot \exp\left(-\frac{E_{\mathrm{a}}}{RT}\right), \tag{4.4}$$

$$k = \frac{k_{\mathrm{b}}T}{h} \cdot \exp\left(-\frac{\Delta G_{\mathrm{a}}}{RT}\right), \tag{4.5}$$

where k_{b}, h, and R are Boltzmann, Planck, and gas constant, respectively. The pre-exponential factor A, also known as the frequency factor, represents the frequency of molecular collisions favorable for chemical reactions. The frequency factor value is usually determined experimentally, and its unit depends on the reaction order. Both the activation energy E_{a} in the Arrhenius equation and the activation Gibbs free energy ΔG_{a} in the Eyring equation represent the height of activation barriers along the reaction pathway. According to the Boltzmann distribution, a fraction of molecules may feature enough energy to overcome the activation barrier at a given temperature T. A scheme of catalyzed and uncatalyzed reaction pathways is displayed in Fig. 4.1.

From Eq. (4.4) and (4.5), it is evident that the reaction rate may be increased either by raising the temperature or lowering the activation barrier. From a practical point of view, lowering the activation barrier by the catalyst is more advantageous. Firstly, the catalyst may be used repeatedly, which is less costly than permanent heating. Secondly, elevated temperatures may increase the reaction rates of unwanted reactions in the system.

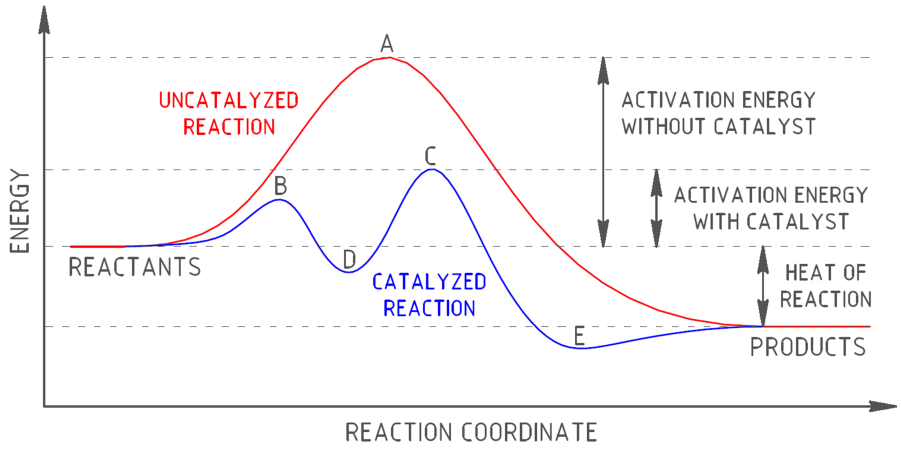

Fig. 4.1: Reaction pathway of catalyzed (blue) and uncatalyzed (red) exothermic reaction. A, B, C – reaction transition states; D, E – reaction intermediates.

Another useful way of visualizing catalyzed reactions, complementary to the free energy - reaction coordinate plot in Fig. 4.1, is a *catalytic cycle* scheme displayed in Fig. 4.2. The loop shape of the diagram represents the recoverability of the catalyst. Each step in the graph shows the origin and destiny of its reactants and products, respectively. Reactants either come from outside (e.g., adsorption) or originate from the previous steps; products either leave the reaction (e.g., desorption) or continue in the reaction as intermediates. The step with the highest energy barrier determines the overall reaction rate. It is denoted as the *rate-limiting step*. The number of catalytic cycles at the active site per unit time, i.e., the *turnover frequency*, is an essential catalyst efficiency indicator.

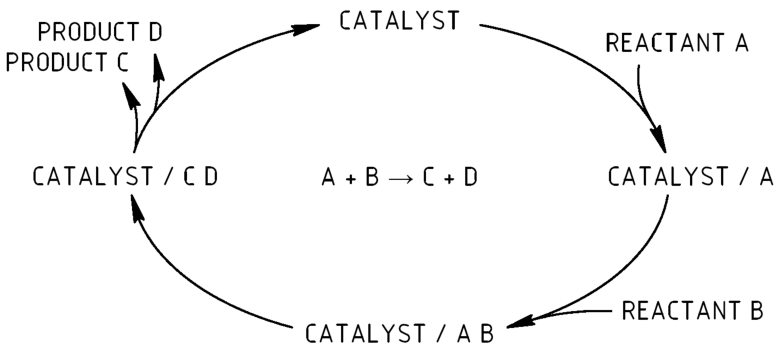

Fig. 4.2: Catalytic cycle of the A + B → C + D reaction. Adapted from [42].

4.1.3. Catalyst composition and structure

Industrial applications frequently employ solid catalysts in various chemical reactor designs, e.g., fixed-bed reactors. Catalysts for industrial applications form either bulky structures or nanoparticles supported on bulky carrier materials [41]. Fixed-bed reactors typically incorporate catalyst pellets with few millimeters in diameter and length; automotive catalytic converters employ ceramic honeycomb structures decorated with catalyst nanoparticles. Placing such structures to the gas pipelines creates a porous obstacle for the gas stream. This arrangement allows enhanced interaction of reactants from the gas

phase with the catalyst surface. The best possible performance is obtained after setting the proper gas mixture, gas pressure, gas flow rate, and surface temperature. Optimal working parameters are found by carrying out catalytic tests in laboratory fixed-bed reactors at various conditions. The stream of products is usually analyzed by a mass spectrometer or gas chromatograph (GC) equipped with a flame ionization detector (FID), thermal conductivity detector (TCD), and other detectors relevant for expected products. Yield, conversion, and selectivity as a function of time-on-stream (TOS) are the most appropriate performance evaluation quantities. Yield evaluates the amount of desired products; conversion evaluates the amount of reactants converted to unspecified products; selectivity evaluates the ratio of desired and undesired products.

The chemical composition and crystallographic structure are two key factors affecting the catalyst performance. Specifically, the electron configuration is the feature, which determines the surface site's contribution to the overall catalyst performance. Reaction participants in one catalytic cycle have to chemisorb onto the catalyst surface, diffuse over the surface, undergo reaction, and finally desorb from the surface. The sites facilitating desired chemical reactions are denoted as active sites. According to Sabatier's principle, the interaction between reaction participants and active sites should provide both reactant bonding and product desorption [43]. Understanding adsorption sites and active sites is crucial for synthesizing catalysts with enhanced densities of desired sites. Quantitative measurement of the active site density is essential for evaluating turnover frequency (TOF) and may be done by physisorption experiments.

As already outlined, industrial catalyst structures are composed either of a single bulky active component, i.e., catalyst, or the catalyst nanoparticles supported on the bulky carrier, i.e., support. Bulky catalysts are usually made of metals and their oxides; nanoparticles are usually made of precious metals. Typical support materials are silica (SiO_2), aluminum oxide (Al_2O_3), or carbon (C). A primary support task is to provide a uniform dispersion of nanoparticles, resulting in a larger active surface area. Even larger surface areas may be reached when employing microporous supports, e.g., zeolites or carbon frameworks. Mass transfer of reaction participants in microporous structures is, however, still not well understood. High thermal stability of support/catalyst composite is desired to prevent thermal deactivation by sintering. Thermally-induced nanoparticle agglomeration leads to the lowered accessibility of active sites for reactants. Mechanical strength is also required, especially during the pellet loading into the reactor. In addition to the previously mentioned support tasks, the support and catalyst synergy may change the electron configuration of surface sites and, therefore, overall catalyst performance. For example, it is well known that metallic nanoparticles supported on the outer surface of carbon nanotubes exhibit different activity than metallic nanoparticles supported on the inner surface of the same support [44]. This feature is a direct consequence of the interaction between support and catalyst caused by asymmetry in the inner and outer nanotube surface electronic properties.

Based on the benefits from synergy between support and catalyst, a third component called promoter may enhance the overall catalyst performance [45]. Many heterogeneous catalysts are promoted by alkali metals, added in significantly smaller amounts than support materials [46]. Because of the minimization of surface energy, promoters usually uniformly spread over the catalyst surface. Their role is hardly predictable. Depending on the support/catalyst composition, the resulting synergy effect may enhance thermal stability, improve reactants chemisorption, or protect the catalyst from oxidation and

sintering. Since promoters physically block surface sites, thick promoter shells around catalyst nanoparticles may negatively affect the overall catalyst performance.

The influence of crystallographic structure on catalyst performance is significant. The coordination number and electron configuration of surface atoms depend on surface planes, surface reconstructions, and defect types. Defects like steps, kinks, edges, holes, and corners are usually favorable for reactants bonding. High-index planes and surfaces with high defect densities, therefore, exhibit enhanced catalytic performance. The dependence of low-coordinated atom densities on nanoparticle size and shape needs to be considered when designing catalyst structures. Various surface structures are displayed in Fig. 4.3.

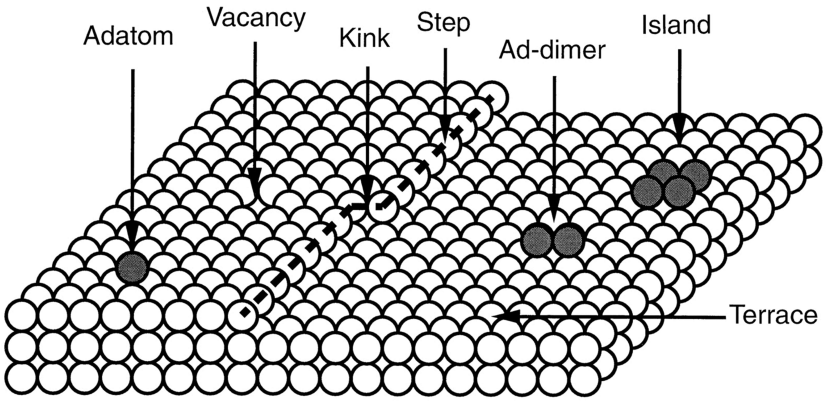

Fig. 4.3: Atomic surface structure. Taken from [47].

Chemisorbed reactant overlayers may, in some cases, lift the surface reconstruction [48]. If the reconstruction occurs repeatedly, the rearrangement of surface atoms transfers chemisorbed species to subsurface layers. The penetration of adsorbents into the bulk may also create subsurface layers. The chemical composition of the catalyst is, therefore, changed. A buildup of subsurface layers may affect the overall catalyst performance either positively or negatively. When desired species get stuck in the near-surface area, the reservoir boosting the reaction is created [49]. On the other hand, incorporating unwanted species into the near-surface area negatively affects electron configuration of surface sites. As a result, the surface may exhibit worsened chemical bonding properties [50]. A variety of other modifications may occur during long-term runs. We will name some of them. Catalysts exposed to reducing or oxidizing atmosphere continuously change their chemical composition. The surface sites may also get poisoned by strongly bonded adsorbed species. As a result, the active sites are blocked, and the surrounding electron configurations are changed. However, in some cases, selective poisoning of surface sites facilitating unwanted reactions may improve the system selectivity towards desired products. Unwanted reaction byproducts are another threat to catalyst performance. Their presence may result in surface self-poisoning or catalyst sintering. Surface faceting is another phenomenon that may also lead to the lowered catalyst activity.

The optimal chemical composition and crystallographic structure of catalyst systems may be theoretically predicted by density functional theory (DFT) [51]. By comparing several reaction pathways, the most probable path with the lowest activation barrier may be found. Based on the height of activation barriers, DFT may also identify adsorption sites,

active sites and reveal whether the reaction will proceed via the Langmuir-Hinshelwood, Eley-Rideal, or Mars van Krevelen mechanism. In the Langmuir-Hinshelwood mechanism, two molecules adsorbed onto the neighboring surface sites undergo a chemical reaction; in the Eley-Rideal mechanism, one adsorbed molecule reacts with the second molecule directly from the gas phase. The Mars van Krevelen mechanism describes reactions where the catalyst surface gets oxidized by gaseous O_2 reactant, and the second reactant is adsorbed onto the oxidized catalyst surface. DFT predictions have to be, of course, verified by catalytic tests and other characterization techniques, which will be described in the further text.

Before the characterization methods are introduced, the preparation of solid catalysts will be briefly described. To start with, the catalyst synthesis and its subsequent activation follow empirical recipes, improved over time. The catalyst structure is composed either entirely of the active material, i.e., bulky catalyst, or the active material is supported on the bulky carrier, i.e., impregnated catalyst. Bulky catalysts and supports for impregnated catalysts are usually prepared by precipitation, hydrothermal synthesis, sol-gel synthesis, or fusion. In the precipitation method, an aqueous solution of precursor salts is prepared. Adding the acid or base reagent to the solution triggers the salt nucleation. Salt crystals then grow until the desired gel is formed. The resulting gel is after aging filtered, washed, dried, and finally calcinated. If the gel is further thermally treated in water, the crystallographic structure of the catalyst changes. This method is called hydrothermal synthesis. In the fusion method, metallic precursors are melted, mixed, and controllably cooled to obtain alloys of desired phases. Impregnated catalysts are usually prepared by incipient wetness impregnation or ion exchange method. Incipient wetness impregnation is based on filling pores of dry support with precursor solution. After adding a reagent, the solution precipitates, and the resulting catalyst is filtered, dried, and calcinated. For industrial applications, the catalyst powder needs to be further pelletized. As a final step, the catalyst activation is performed. Unwanted impurities originating from the synthesis procedure, e.g., nitrates from precursors, are removed by calcination. In some cases, the reduction of oxidized species by H_2 treatment is desired.

Synthesized catalysts need to be characterized before and after each catalytic test. Physisorption experiments determine the surface area and pore volume. The effect of reducing and oxidizing atmospheres on the catalyst is evaluated by Temperature-Programmed Reduction (TPR) and Temperature-Programmed Oxidation (TPO) experiments. The catalyst morphology may be observed by Scanning Electron Microscopy (SEM). However, High-Resolution Transmission Electron Microscopy (HRTEM) with the sub-angstrom resolution is more relevant for studying particles with few nanometers. TEM measurements usually determine the size distribution of catalyst nanoparticles and their structure. Energy-Dispersive X-ray analysis (EDS) in TEM may be employed to check the uniformity of elemental dispersion. X-Ray Diffraction (XRD) is a commonly used technique in catalyst research to identify crystalline phases. According to the Scherrer equation, XRD may also be used for the crystallite size determination. The elemental composition of the surface and near-surface layers is determined by X-Ray Photoelectron Spectroscopy (XPS). Elemental oxidation states are identified by XPS as well. Oxidation states and coordination numbers are determined by X-Ray Absorption Near-Edge Structure (XANES) and Extended X-Ray Absorption Fine Structure (EXAFS), respectively. Diffuse-Reflectance Infrared Fourier-Transform Spectroscopy (DRIFTS) is a powerful technique for identifying reaction intermediates and adsorption configurations

of molecules. The influence of the ambient atmosphere on surface reconstruction may be studied by Scanning Tunneling Microscopy (STM) or Low Energy Electron Diffraction (LEED). Besides the most frequently used catalyst research techniques above, there is a whole arsenal of other powerful surface analytical tools that were not mentioned.

For a deeper understanding of the catalyst working principles, it is not sufficient to study their chemical and crystallographic composition only before and after catalytic tests. To identify distinct catalyst regimes (e.g., activation, stable performance, deactivation) and associated structural changes, the sample needs to be observed in operando experiments. The main limitation of operando experiments is the magnitude of the ambient gas pressure. Industrially relevant conditions for heterogeneous catalysis usually exceed tens of bars; however, conventional surface science techniques usually require ultrahigh vacuum conditions. This constraint may be overcome by differentially pumped environmental microscopes (e.g., environmental SEM, environmental TEM) or closed nanoreactors with transparent windows for probes, which can be loaded to conventional microscopes [31]. For example, nanoreactors equipped with gas chromatography may be employed in in-situ synchrotron-based X-ray, in-situ DRIFTS, or in-situ environmental TEM experiments.

4.2. Catalytic CO Oxidation to CO_2 Over Pt Surfaces

Fundamental concepts introduced in the previous section will be applied to the catalytic CO oxidation by O_2 over Pt surfaces. In the beginning, typical industrial uses and state-of-the-art catalyst structures will be introduced. Then, the reaction thermodynamics and kinetics of simplified systems without promoters will be described. Essential for our research is a detailed understanding of CO oxidation by O_2 over well-defined Pt single-crystal surfaces. This reaction, considered a model system of heterogeneous catalysis, will be experimentally explored by time-of-flight secondary ion mass spectrometry (TOF-SIMS) to exhibit this method's catalytic research abilities. Continuing in the work of Gerhard Ertl et al. [52], spatiotemporal patterns created by varying reactant coverages, e.g., chemical fronts, or target patterns, will be monitored by the in-situ TOF-SIMS technique. Spatiotemporal pattern formation on platinum surfaces will be, therefore, explained as well. Since the reaction mechanism changes with the surrounding reactant pressures, it is noteworthy that further explanation aims primarily at high vacuum conditions because the maximal permitted pressure in the main chamber of the employed TOF-SIMS instrument reaches $3 \cdot 10^{-3}$ Pa.

4.2.1. Industrial applications

Platinum is a rare earth metal with a total mining supply of 173 tons in 2019 [53]. For comparison, gold mining production hit 3 464 tons in the same year [54]. The total platinum supply, including recycling, reached 233 tons, while 235 tons were demanded by automotive, jewelry, investment, and other industry branches. The most significant demand of 35% for platinum came from the automotive industry to produce catalytic converters. The limited global resources of platinum indicate that sophisticated support/catalyst/promoter structures with high CO conversion rates and minimized bulk platinum volume are highly required.

CO as a product of incomplete combustion of fossil fuels is a serious health threat due to its 210 times higher affinity to hemoglobin than O_2 [55]. Exposure to concentrations higher than 12 800 ppm (1.28%) causes fatal oxygen deprivation of the human body vital organs within 1 to 3 minutes [56]. Three-way catalytic converters (TWCs) provide conversion of poisonous CO from vehicle exhaust fumes to less harmful CO_2. The remaining two reactions in TWCs are oxidation of hydrocarbons to $CO_2 + H_2O$ and reduction of nitrogen oxides to $O_2 + N_2$. Typical autocatalysts are composed of honeycomb ceramic substrates with hundreds of cells per square inch, coated with $\gamma - Al_2O_3$ carrier [57]. CeO_2 promoted Pt/Pd nanoparticles facilitate oxidation reactions, while CeO_2 promoted Pt/Rh nanoparticles facilitate reduction reactions. The adequate working conditions for autocatalysts are around 800 °C. The illustration of TWC is displayed in Fig. 4.4.

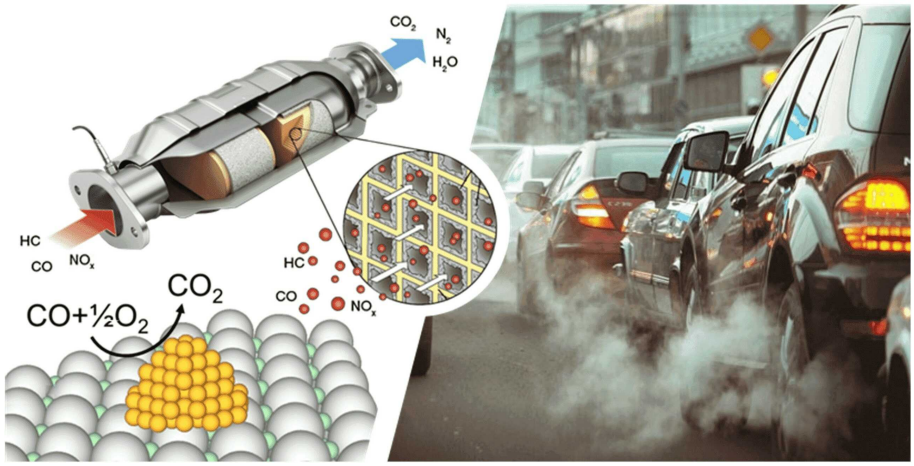

Fig. 4.4: Cartoon illustrating operation of the three-way catalytic converter. Images were taken from [58–60].

Another industrial application employs Pt/CeO_2 catalysts for preferential oxidation of CO in H_2-rich streams (CO-PROX reaction) [61]. The most common way of H_2 production today is a stream reforming of natural gas ($CH_4 + H_2O \leftrightarrows CO + 3H_2$) followed by a water-gas shift reaction ($CO + H_2O \leftrightarrows CO_2 + H_2$). Excessive CO residual concentrations in $H_2 + N_2$ streams for ammonia production cause poisoning of Al/K promoted Fe_3O_4 catalysts widely used in the Haber-Bosch process [62]. H_2 also serves as an effective fuel for various fuel cell types, e.g., indirect methanol fuel cells (IMFC) or proton-exchange membrane fuel cells (PEMFC). Feeding CO molecules over platinum fuel cell electrodes operating at low temperatures around 80 °C causes their CO poisoning and consequent performance decrease [25–27].

An extensive overview of various platinum catalysts for low-temperature CO oxidation was published by Dey and Dhal [29]. The critical factor affecting catalyst activity at low temperatures is the oxygen storage property of the support. That stems from the fact that Pt surfaces get at low temperatures easily poisoned by CO, preventing O_2 adsorption. The CO oxidation on Pt, supported by reducible metal oxides, e.g., Pt/CeO_2, Pt/IrO_2, and Pt/TiO_2, is, therefore, initiated at lower temperatures than CO oxidation on systems composed of Pt/Al_2O_3, $Pt\text{-}BaSnO_3$, Pt/ZrO_2, or Pt/SiO_2. The highest activity and stability for low-temperature CO oxidation were observed on $Pt\text{-}CeO_2/SiO_2$ catalysts. The full conversion of 2 500 ppm CO in the air was detected at 25 °C [63].

4.2.2. Platinum

Platinum (Pt) is a silverish-white transition metal with an atomic number 78. Six naturally occurring Pt isotopes are ^{190}Pt (0.01%), ^{192}Pt (0.78%), ^{194}Pt (32.86%), ^{195}Pt (33.78%), ^{196}Pt (25.21%) and ^{198}Pt (7.36%). The most abundant ^{195}Pt isotope decays with a half-life of $6.5 \cdot 10^{11}$ years. In the periodic table of elements, Pt is found in d-block, period 6, and group 10. The remaining three group 10 elements are nickel (Ni), palladium (Pd), and darmstadtium (Ds). Due to excellent corrosion resistance, Pt belongs, together with silver (Ag), gold (Au), ruthenium (Ru), rhodium (Rh), palladium (Pd), osmium (Os) and iridium (Ir) to the group of noble metals. Typical Pt physical properties are lustrousness, high electrical conductibility, and ductility. Pt electric resistivity is 105 nΩ.m at 20 °C, Mohs hardness is 3.5, and melting point reaches 1 768.3 °C. The most common oxidation states are +2 and +4. The less common oxidation states +1 and +3 are usually stabilized by metallic bonding in bimetallic species. Atomic radius reaches 1.39 Å, and the first ionization energy of Pt atom is 870 kJ/mol. The atomic weight of the most abundant ^{195}Pt isotope is 194.96 Da.

The crystallographic structure of Pt catalysts significantly affects their performance in CO oxidation. Pt particularly crystallizes in face-centered cubic structure (FCC), with eight Pt atoms at the corners and six Pt atoms in the face centers of the cubic unit cell. The length of the Pt FCC unit cell is 3.92 Å. Various high Miller index surfaces, also known as stepped faces, may be constituted by different combinations of three basal low Miller index planes – Pt(100), Pt(110), and Pt(111). High Miller index planes are typically composed of low Miller index terraces separated by periodic, monatomic height steps. Each single-crystal surface may be defined either by Miller indices $(h\,k\,l)$ or step-terrace notation $m\,(h\,k\,l) \times n\,(h'\,k'\,l')$. Miller indices define macroscopic surface planes, while step notation allows the definition of surfaces with multiple height steps. In the step-terrace notation, m denotes terrace width, $(h\,k\,l)$ denotes terrace orientation, n denotes step height, and $(h'\,k'\,l')$ denotes step orientation. Structures with large m, n coefficients are called facets. Monatomic height steps, multiple height steps, and stereographic triangle for FCC single-crystal faces are displayed in Fig. 4.5. Varying coordination numbers and atomic surface densities of three low Miller index planes indicate that the electronic properties of Pt surface atoms differ with crystallographic orientations. Pt(111) surface atom has 9 nearest neighbors, Pt(100) surface atom has 8 nearest neighbors, and Pt(110) surface atom has 7 nearest neighbors. For comparison, the coordination number of Pt bulk atom is 12. Atomic surface density of three basal planes follows the order of $1.5 \cdot 10^{15}$ at.cm^{-2} for Pt(111) $> 1.3 \cdot 10^{15}$ at.cm^{-2} for Pt(100) $> 0.9 \cdot 10^{15}$ at.cm^{-2} for Pt(110).

A detailed LEED study of the stability of various high Miller index Pt planes was published by Blakely et al. [64]. Pt samples were exposed to ultra-high vacuum, $1 \cdot 10^{-6}$ Torr oxygen atmosphere, and an atmosphere containing hydrocarbons. Among twenty-two examined Pt surface structures, Pt(100), Pt(110), Pt(111), Pt(113), Pt(112), Pt(012), Pt(122) and Pt(133) were stable in all three surrounding atmospheres. Clean Pt(111) surface, as well as oxygen- and carbon-covered Pt(111) surfaces, exhibit a bulklike 1×1 termination. Clean Pt(100) surface and oxygen covered Pt(100) surface reconstruct into the quasi-hexagonal structure with the lowered surface energy. In hydrocarbons atmosphere, the Pt(100) - hex reconstruction is lifted into a 1×1 structure. Similar behavior was observed on Pt(110) surface. Clean Pt(110) surface and oxygen-covered Pt(110) surface reconstruct into a 1×2 "missing row" structure, while carbon coverage lifts the Pt(110)

- 1×2 reconstruction into a 1×1 structure. Pt(110) surface with saturated oxygen coverage further transforms into a c(2×2) structure [65]. Pt(110) – 1×1 structure looks like a perfectly stepped surface [66], while Pt(110) – 1×2 structure is composed of 3(111) microfacets separated by ridges and valleys. Nonreconstructed and reconstructed surface structures of three low Miller index Pt planes are displayed in Fig. 4.5. Exposure of unstable surface structures to elevated temperatures and oxidizing or reducing atmospheres causes their transformation into more stable step-terrace structures. This process is known as faceting.

The importance of bulky single-crystals in catalytic fundamental research lies in the periodic arrangements of surface atoms, allowing direct assignment of catalyst performance to the well-known surface structure. However, bulky Pt single-crystals in industrial applications are inconvenient due to their high production costs. Therefore, processes allowing the cost-effective, mass production of Pt nanoparticles with the desired shape and crystallographic structure need to be developed. For example, Cheng et al. developed a method for synthesizing cube-octahedral-shaped Pt single-crystal nanoparticles with (111) facets [67]. Commonly used Pt structures in the industry today are polycrystalline nanoparticles composed mainly of randomly arranged low-coordinated Pt atoms.

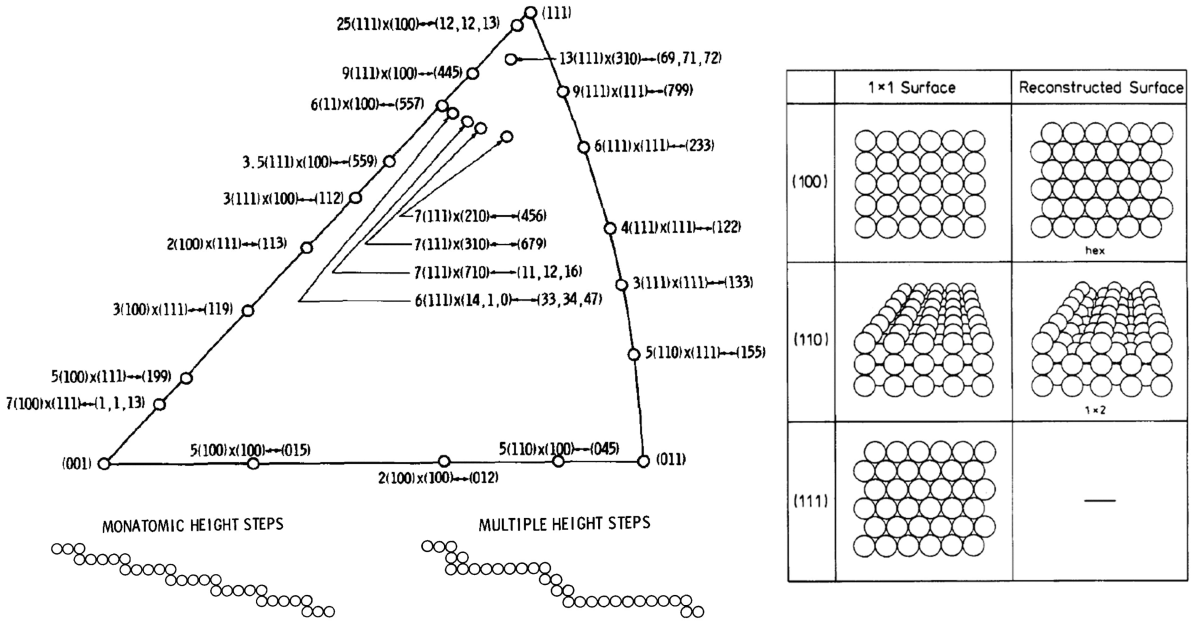

Fig. 4.5: *(left)* Stereographic triangle of FCC single-crystal faces. Monatomic height steps are noted as $m\,(h\,k\,l)\times(h'\,k'\,l')$, and multiple height steps are noted as $m\,(h\,k\,l)\times n\,(h'\,k'\,l')$. Taken from [64]. *(right)* Three Pt low Miller index planes in nonreconstructed 1×1 and reconstructed form. Taken from [68].

4.2.3. Platinum – oxygen interaction

The way O_2 molecules from the gas phase (O_2(g)) interact with Pt surface atoms depends on surface temperature, oxygen partial pressure, and crystallographic orientation of the surface. Extensive studies in the field of platinum-oxygen interaction are concerned with four major topics: identification of surface sites with enhanced oxygen sticking coefficients, understanding of the oxygen adsorption mechanism, understanding of the sub-

surface oxygen influence on catalytic activity, and understanding of the platinum oxide influence on catalytic activity.

At temperatures below 150 K, oxygen chemisorbs onto Pt surface in a molecular form ($O_2(g) \rightarrow O_{2,ad}$) [69]. Above 150 K, oxygen starts to chemisorb dissociatively ($O_2(g) \rightarrow 2O_{ad}$). When the surface temperature exceeds 700 K, associative desorption of oxygen occurs [70]. A comparative study of oxygen adsorption on flat and stepped Pt surfaces was published by Winkler et al. [69]. Flat Pt(111) and stepped Pt(112) ([3(111)×(100)] in step notation) surfaces were studied by TPD, isothermal desorption, AES, LEED, and isotopic exchange. The saturated $O_{2,ad}$ coverage at 87 K reaches 0.5 ML for Pt(111) and 0.51 ML for Pt(112) surfaces. The saturated O_{ad} coverage at 300 K reaches 0.25 ML for Pt(111) and 0.37 ML for Pt(112) surfaces. Higher O_{ad} saturation coverage on stepped surfaces indicates a higher probability of dissociative O_2 adsorption at steps. The initial O_2 sticking coefficient at 87 K reaches 0.29 for Pt(111) and 0.97 for Pt(112) surfaces. The initial O sticking coefficient at 300 K reaches 0.05 for Pt(111) and 0.53 for Pt(112) surfaces. Results presented by Winkler et al. indicate that oxygen coverage of Pt surfaces is relatively sparse, and the oxygen sticking coefficient is higher for stepped surfaces. Therefore, stepped surfaces facilitate oxygen adsorption.

A DFT (GGA-RPBE[1]) study of O_2 dissociation on flat Pt(111) and stepped Pt(211) ([3(111)×(100)] in step notation) surfaces was published by Šljivančanin and Hammer [71]. The most probable pathways for O_2 dissociation were found by evaluating energetics of molecular precursor states (MPS), transition states (TS), and the final states of dissociated O atoms. The study considered various geometries of O_2 chemisorption to flat Pt(111) surfaces, to flat Pt(111) surfaces at the proximity of step edges, O_2 chemisorption parallelly to step edges, and perpendicularly to step edges. The influence of preabsorbed atomic and molecular oxygen species on O_2 dissociation was investigated as well. In agreement with STM experiments [72], O_2 chemisorption, dissociation, and O binding to steps were favored over the same processes on terraces. At Pt(211) step edges, O_2 molecules chemisorb exclusively in top-bridge-top (t-b-t) MPS with the chemisorption potential energy of −0.9 eV and dissociation barrier of 0.9 eV with respect to MPS. On Pt(111) terraces, O_2 molecules chemisorb in top-fcc-bridge (t-fcc-b) and top-bridge-top (t-b-t) MPS with the chemisorption potential energy of −0.1 eV for both states. However, O_2 dissociation is favored at top-fcc-bridge MPS with a dissociation barrier of 0.6 eV with respect to MPS. Reaction energetics and geometries for Pt(211) t-b-t and Pt(111) t-fcc-b pathways are displayed in Fig. 4.6. Atomic O preferably bonds to bridge fcc sites on Pt(211) surface with chemisorption energy of −1.1 eV relative to $\frac{1}{2}\,O_2(g)$, while on Pt(111), atomic O preferably bonds to threefold fcc sites with a binding energy of −0.7 eV relative to $\frac{1}{2}\,O_2(g)$. At small distances, preabsorbed oxygen species strongly repel $O_2(g)$ molecules.

The influence of Pt(111) subsurface oxygen on CO oxidation was investigated by Bashlakov et al. [73]. A buildup of subsurface oxygen layer was revealed by LEED, STM, and TPD studies. The subsurface layer was created after the Pt(111) 400 L O_2 exposure ($1\,L = 1 \cdot 10^{-6}$ Torr.s) in UHV conditions and sample temperatures ranging from 400 K to 600 K. While LEED and STM experiments observed p(2×2) - O chemisorbed overlayer with saturation coverage of 0.25 ML, TDS experiments revealed that additional oxygen must be stored under the surface. The amount of desorbed O_2 would correspond to 0.5 ML coverage, which is well above the common observations [69]. Unlike the case of subsurface

[1] generalized gradient approximation revised Perdew-Burke-Ernzerhof

oxygen decreasing CO oxidation activity on Pd(111) catalysts [50], subsurface oxygen on Pt(111) does not lower the activity of Pt towards CO oxidation. The influence of platinum oxide on Pt catalytic activity is discussed in the reaction mechanism section.

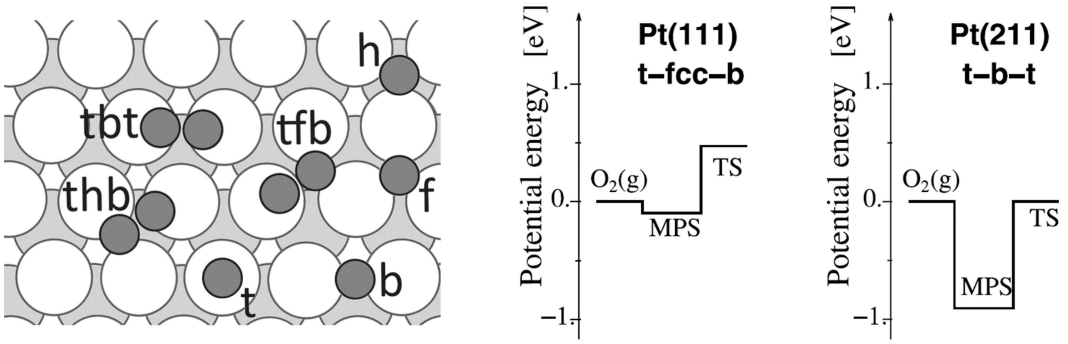

Fig. 4.6: *(left)* Schematic illustration of oxygen adsorption sites and O_2 adsorption configurations on Pt(111) surface. Adsorption sites are denoted as t – top, b – bridge, f – fcc, h – hcp. O atoms are displayed as dark-grey disks, Pt 1st layer atoms are displayed as white disks, and Pt 2nd layer atoms are displayed as light-grey disks. Adapted from [74]. *(right)* The molecular precursor (MPS) and transition state (TS) energies along the most favorable reaction pathway for O_2 dissociative adsorption on Pt(111) terraces and Pt(211) steps. Taken from [71].

4.2.4. Platinum – carbon monoxide interaction

CO chemisorbs onto Pt surface in a molecular form ($CO(g) \rightarrow CO_{ad}$). Similarly to Pt–$O_2$ interaction, Pt-CO interaction depends on surface temperature, CO partial pressure, and crystallographic orientation of Pt surface. Generally, CO bonding to Pt surfaces follows the Blyholder model [75]. Electrons from the highest occupied molecular orbital (HOMO) at the carbon end of CO molecule – 5σ – are donated into Pt, while Pt d-electrons are backdonated into the lowest unoccupied molecular orbital (LUMO) of CO molecule – $2\pi^*$, see Fig. 4.7. TPD experiments with Pt(335) ([4(111)×(100)] in step notation) surfaces revealed that at temperatures around 400 K, CO molecules desorb from terraces [76]. At temperatures around 500 K, desorption of CO molecules from steps occurs.

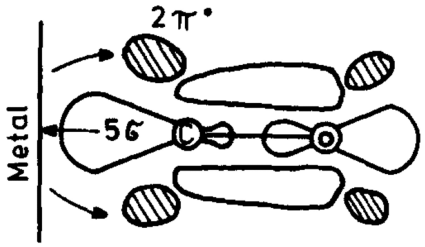

Fig. 4.7: Schematic illustration of CO molecule chemisorbed on Pt surface. Taken from [75].

A detailed DFT (vdW-DF[2]) investigation of CO adsorption on Pt(111) surfaces was published by Gunasooriya and Saeys [77]. The study was concerned with the stability of various CO adsorption structures at low and high CO-coverages. Among several hundreds

[2]van der Waals density functional

of examined structures four structures were found stable: 0.33 ML ($\sqrt{3}\times\sqrt{3}$)R30° - CO (top); 0.5 ML c(4×2) – 4 CO (1:1 bridge:top); 0.6 ML c($\sqrt{3}\times5$)rect – 6 CO (1:2 bridge:top); 0.67 ML saturation coverage c($\sqrt{3}\times3$)rect – 4 CO (1:3 bridge:top). These structures were also observed experimentally. In agreement with Gunasooriya and Saeys [77], in terms of preferred adsorption sites, is a DFT (vdW-DF) study of Lakshmikanth et al. [78], whose calculated CO adsorption energies follow the order of -1.46 eV for top $<$ -1.43 eV for bridge $<$ -1.42 eV for hcp $<$ -1.40 eV for fcc.

4.2.5. Reaction mechanism

The widely accepted mechanism of CO oxidation by O_2 over Pt catalysts is a Langmuir-Hinshelwood mechanism. However, many research groups pointed out that the mechanism changes with reactants' partial pressures, reaction temperature, and catalyst surface structure. Our experiment's typical partial pressures are $p_O = 1.5 \cdot 10^{-3}$ Pa, $p_{CO} = 3.0 \cdot 10^{-4}$ Pa, reaction temperature ranges from room temperature to 1 000 °C, and Pt surface is usually composed of high Miller index planes. In order to assign the right mechanism to our experimental conditions, various CO oxidation mechanisms over Pt surfaces will be introduced.

Low-pressure studies of catalytic CO oxidation on platinum metals from the late '60s and early '70s assigned the Langmuir-Hinshelwood mechanism for CO pre-covered surfaces and the Eley-Rideal mechanism for O pre-covered surfaces [79]. However, based on the molecular beam studies from the late '70s [80], Engel and Ertl concluded that, in fact, no evidence for the Eley-Rideal mechanism exists [81]. According to the Langmuir-Hinshelwood mechanism, the CO molecule adsorbs non-dissociatively onto the Pt surface, requiring one free surface site ($\star$) (A1). For temperatures below 600 K, CO_{ad} molecules form a densely packed layer prohibiting oxygen adsorption [68]. When two free surface sites are accessible, the O_2 molecule adsorbs onto the Pt surface dissociatively (A2). Recombination and thermal desorption of O_2 molecule occurs at temperatures above 700 K [70]. O_{ad} overlayer does not inhibit CO adsorption. If CO_{ad} molecule meets O_{ad} atom at the neighboring surface site, the $CO_{2,ad}$ molecule and one free surface site are formed (A3). $CO_{2,ad}$ molecule is subsequently desorbed, leaving one free surface site behind (A4). Equations (A1)–(A4) are taken from [82].

$$CO + \star \leftrightarrows CO_{ad} \quad \text{(A1)}$$

$$O_2 + 2\star \leftrightarrows 2O_{ad} \quad \text{(A2)}$$

$$O_{ad} + CO_{ad} \rightarrow CO_{2,ad} + \star \quad \text{(A3)}$$

$$CO_{2,ad} \rightarrow CO_2 + \star \quad \text{(A4)}$$

DFT comparison of the Langmuir-Hinshelwood and Eley-Rideal pathways for CO oxidation on Pt(111) catalyst surface was published by Baxter and Hu [83]. Fig. 4.8 shows that the activation barrier with respect to O_{ad} + CO_{ad} for the Langmuir-Hinshelwood mechanism (1.05 eV) is higher than the activation barrier with respect to O_{ad} + CO(g) for the Eley-Rideal mechanism (0.72 eV). Although the activation barrier on the Eley--Rideal pathway is lower, the reaction proceeds via the Langmuir-Hinshelwood pathway because CO adsorption to sparsely O_{ad} covered Pt surface is still energetically and statistically more favorable than direct reaction with O_{ad} molecule. What is more, frequently occurring unfavorable tilting of CO(g) molecule reaching the O_{ad} molecule significantly increases the activation barrier of the Eley-Rideal mechanism.

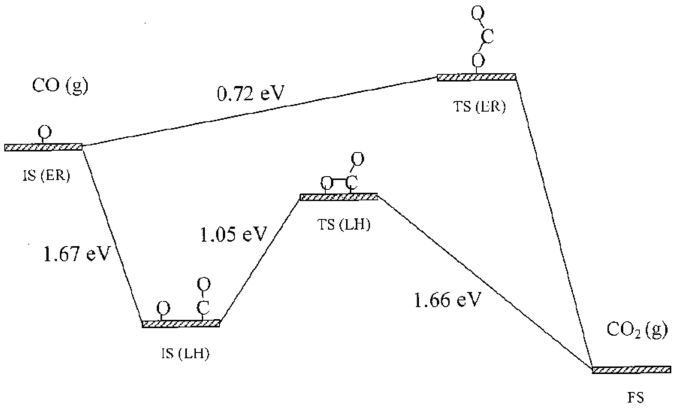

Fig. 4.8: Comparison of reaction pathways of CO oxidation on Pt(111) surface proceeding via Langmuir-Hinshelwood (LH) and Eley-Rideal (ER) mechanism. Taken from [83].

The effect of lattice strain on CO oxidation over Pt(111) surface, proceeding via the Langmuir-Hinshelwood mechanism, was studied by Grabow et al [84]. CO oxidation over Pt(111) was simulated using microkinetic modeling, and DFT (GGA-PW91[3]) calculations at partial pressures of $p_O = 1.02 \cdot 10^{-2}$ mbar, $p_{CO} = 1.89 \cdot 10^{-3}$ mbar, and reaction temperatures ranging from 400 K to 800 K. The lattice strain variation is typically driven by the heat released in the exothermic reactions on ultrathin Pt samples. Temperature variation in the order of 10^1 K may result in the sample wrinkling, causing compression and stretching of various sample parts. The resulting change in the Pt lattice constant affects binding energies, activation barriers, and the rate-limiting step, which directly affects the rate of CO_2 production. Fig. 4.9 shows that CO oxidation at 530 K, follows on equilibrated Pt(111) surface with lattice constant of 4.00 Å and 2% compressed Pt(111) surface with lattice constant of 3.92 Å pathways with higher energy states than on 4% stretched Pt(111) surface with lattice constant of 4.16 Å. Height of the activation barrier in the rate-limiting step, which is assigned to O_2 dissociation, follows the order of 4% stretched surface (0.71 eV) < equilibrated surface (0.77 eV) < 2% compressed surface (0.89 eV).

Based on the energy of desorbing CO_2 molecules from Pt(111) and Pt(332) ([6(111)× (111)] in step notation) surfaces, Neugebohren et al. identified three distinct mechanisms which precede the Langmuir-Hinshelwood recombination of CO molecules with O atoms [85]. Pulsed-molecular-beam was used for O_2 and CO dosing. CO oxidation was initiated by the introduction of CO molecules to the oxygen pre-covered Pt surface. The Pt(111) surface structure with a 0.25% step density causes more than 99% of impinging CO molecules to be initially adsorbed onto terrace sites. Velocity vectors of desorbing CO_2 molecules were monitored by slice ion imaging technique. Desorbing CO_2 molecules were divided into two groups. Hyperthermal CO_2 molecules ($CO_2^{\text{hyperthermal}}$) desorb promptly from Pt terrace sites with high kinetic energies, high internal energies, and narrow angular distribution. On the other hand, thermal CO_2 molecules (CO_2^{thermal}) get before desorption trapped at Pt step sites resulting in lower kinetic energies, lower internal energies, and broader angular distribution. Despite the dominance of terrace sites over step sites, CO_2 molecules desorb at temperatures below 700 K, primarily from step sites (CO_2^{thermal}). CO_2^{thermal} molecules may originate from two types of reactions. The first reaction involves CO molecules initially adsorbed onto step sites ($CO_{\text{ad}}^{\text{step}}$) and O atoms

[3]generalized gradient approximation Perdew-Wang 1991

adsorbed onto step sites (O_{ad}^{step}) (B1). The second reaction involves CO molecules initially adsorbed onto terrace sites ($CO_{ad}^{terrace}$) but subsequently diffused to step sites and O_{ad}^{step} atoms (B2). At higher temperatures, mainly $CO_2^{hyperthermal}$ molecules are detected. Domination of hyperthermal channel stems from the fact that CO desorption at elevated temperatures is much faster than diffusion. Therefore, CO molecules oxidate immediately at adsorption sites (B1) (B3). Equations (B1)–(B3) are taken from [85].

$$CO_{ad}^{step} + O_{ad}^{step} \rightarrow CO_2^{thermal} \quad \text{(B1)}$$

$$CO_{ad}^{terrace} + O_{ad}^{step} \rightarrow CO_2^{thermal} \quad \text{(B2)}$$

$$CO_{ad}^{terrace} + O_{ad}^{terrace} \rightarrow CO_2^{hyperthermal} \quad \text{(B3)}$$

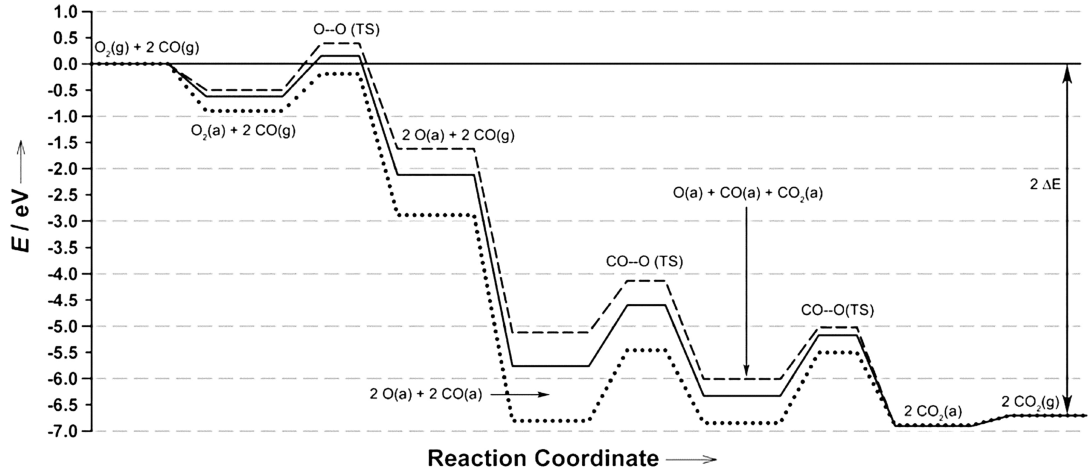

Fig. 4.9: Comparison of reaction pathways of CO oxidation on 4% stretched Pt(111) surface (· · ··), equilibrated Pt(111) surface (——), and 2% compressed Pt(111) surface (– – –) proceeding via Langmuir-Hinshelwood mechanism. Taken from [84].

A comprehensive study of particle size effect on CO oxidation over Al_2O_3 supported Pt nanoparticles was published by Neumann et al. [82]. Four different reaction mechanisms were identified on nanoparticles with 1 – 4 nm in diameter at reaction temperatures ranging from 170 °C to 250 °C. An assignment of reaction mechanism to specific experimental conditions was based on kinetic measurements. Experimental data of turnover frequency (TOF) as a function of reactants' partial pressures were compared with theoretically derived rate equations of various mechanisms and the most suitable mechanism was chosen (listed below). O_2 partial pressures varied from 6.8 kPa to 20.3 kPa at 0.39 kPa constant CO partial pressure; CO partial pressures varied from 0.29 kPa to 0.45 kPa at 12.2 kPa constant O_2 partial pressure. The highest activity of CO oxidation was observed on 2 nm Pt nanoparticles with a high density of low-coordinated Pt atoms.

Neumann et al. observed that CO oxidation over 1 – 4 nm Pt nanoparticles at 170 °C proceeded via the Langmuir-Hinshelwood mechanism. Boudouard reaction was identified as a side reaction. In the Boudouard reaction, CO_{ad} molecule (C1) reacting with another CO_{ad} molecule (C1) produces $CO_{2,ad}$ molecule and C_{ad} atom (C3). $O_{2,ad}$ molecule adsorbed onto Pt surface (C2) reacts with C_{ad} atom. As a result, another $CO_{2,ad}$ molecule and one free surface site are created (C4). Both $CO_{2,ad}$ molecules are desorbed from the Pt surface, leaving two free surface sites behind (C5). Boudouard reaction occurs mainly on the nearly CO-covered Pt surfaces and is facilitated by pressure [86]. Equations (C1)–(C5)

are taken from [82].

$$\mathrm{CO} + \star \leftrightarrows \mathrm{CO_{ad}} \quad \text{(C1)}$$
$$\mathrm{O_2} + \star \leftrightarrows \mathrm{O_{2,ad}} \quad \text{(C2)}$$
$$\mathrm{CO_{ad}} + \mathrm{CO_{ad}} \rightarrow \mathrm{CO_{2,ad}} + \mathrm{C_{ad}} \quad \text{(C3)}$$
$$\mathrm{C_{ad}} + \mathrm{O_{2,ad}} \rightarrow \mathrm{CO_{2,ad}} + \star \quad \text{(C4)}$$
$$\mathrm{CO_{2,ad}} \rightarrow \mathrm{CO_2} + \star \quad \text{(C4)}$$

For higher temperatures, a significant dependence of the reaction mechanism on particle size was observed. CO oxidation over 1 nm Pt nanoparticles at 200 °C proceeded with kinetic behavior typical for the mechanism proposed by Langmuir in 1922 [87], i.e., $r = k\,[\mathrm{CO}]^{-1}\,[\mathrm{O_2}]^{1}$. Reaction order of -1 for CO indicates reaction deceleration by densely packed CO_{ad} overlayer (D1). Reaction order of 1 for O_2 denotes that O_2 molecules adsorb onto the Pt surface non-dissociatively (D2). Subsequent interaction of $O_{2,ad}$ molecule with adjacent free surface site causes $O_{2,ad}$ dissociation to O_{ad} atoms (D3). Identically to the Langmuir-Hinshelwood mechanism, CO_{ad} molecule recombines with neighboring O_{ad} atom, creating $CO_{2,ad}$ molecule and one free surface site (D4). $CO_{2,ad}$ molecule is subsequently desorbed from the Pt surface, leaving one free surface site behind (D5). Equations (D1)–(D5) are taken from [82].

$$\mathrm{CO} + \star \leftrightarrows \mathrm{CO_{ad}} \quad \text{(D1)}$$
$$\mathrm{O_2} + \star \rightarrow \mathrm{O_{2,ad}} \quad \text{(D2)}$$
$$\mathrm{O_{2,ad}} + \star \rightarrow 2\mathrm{O_{ad}} \quad \text{(D3)}$$
$$\mathrm{O_{ad}} + \mathrm{CO_{ad}} \rightarrow \mathrm{CO_{2,ad}} + \star \quad \text{(D4)}$$
$$\mathrm{CO_{2,ad}} \rightarrow \mathrm{CO_2} + \star \quad \text{(D5)}$$

According to Neumann's study, CO oxidation over Pt nanoparticles with a higher density of high-coordinated Pt atoms at terraces, i.e., nanoparticles larger than 3 nm, proceeds via Langmuir-Hinshelwood mechanisms accompanied with Boudouard reaction.

An alternative pathway to Langmuir's mechanism of CO oxidation over Pt surfaces, with identical reaction orders, was observed by Allian et al. [88]. The proposed mechanism was investigated on Al_2O_3 supported 1-20 nm Pt nanoclusters by kinetic, isotopic, and infrared studies. Rate experiments were performed at reaction temperatures ranging from 360 K to 445 K; O_2 partial pressures varied from 4 kPa to 18 kPa at 0.1 kPa constant CO partial pressure; CO partial pressures varied from 0.02 kPa to 0.8 kPa at 10 kPa constant O_2 partial pressure. The only two differences between the mechanism proposed by Allian et al. and Langmuir lie in the reversibility of O_2 adsorption (E2)(D2) and in the mechanism of $O_{2,ad}$ dissociation, which is either assisted by CO_{ad} molecule (E3) or driven by neighboring free surface site (C3), respectively. DFT (GGA-RPBE) calculations show that CO oxidation with CO_{ad}-assisted $O_{2,ad}$ dissociation proceeds via a pathway with a lower activation barrier than Langmuir's mechanism, and therefore seems to be favored. Equations (E1)–(E5) are taken from [82].

$$\mathrm{CO} + \star \leftrightarrows \mathrm{CO_{ad}} \quad \text{(E1)}$$
$$\mathrm{O_2} + \star \leftrightarrows \mathrm{O_{2,ad}} \quad \text{(E2)}$$
$$\mathrm{O_{2,ad}} + \mathrm{CO_{ad}} \rightarrow \mathrm{CO_{2,ad}} + \mathrm{O_{ad}} \quad \text{(E3)}$$
$$\mathrm{O_{ad}} + \mathrm{CO_{ad}} \rightarrow \mathrm{CO_{2,ad}} + \star \quad \text{(E4)}$$
$$\mathrm{CO_{2,ad}} \rightarrow \mathrm{CO_2} + \star \quad \text{(E5)}$$

Platinum oxidation is another critical phenomenon affecting the mechanism of CO

oxidation over Pt surfaces. The formation of platinum oxide (PtO_2) is generally ascribed to elevated oxygen partial pressures ($1 - 5$ bar) and reaction temperatures ($400 - 500$ K), typically occurring in industrial applications [89]. The study of Pt catalysts by conventional UHV surface science techniques usually does not allow conditions for Pt oxidation. Hendriksen and Frenken, therefore, employed high-pressure high-temperature STM for the study of CO oxidation over Pt(110) surfaces and revealed that the surface in oxidic state exhibits higher CO oxidation activity than the surface in a metallic state [90]. During the experiment, the reaction temperature was kept constant at 425 K, and O_2 partial pressure reached maximally 1.25 bar. The reactivity of oxidized Pt(110) surfaces was further investigated by Pedersen et al. in DFT (GGA-RPBE) studies [91]. Evaluation of activation barriers for various reaction pathways showed that CO oxidation may proceed via the Langmuir-Hinshelwood and the Eley-Rideal mechanism on Pt(110) - (12×2) - 2O structures. The second structure facilitating CO adsorption and oxidation is the $(10\bar{1}0)$ facet of $\alpha - PtO_2$ oxide. Feasible reaction pathways for both structures are displayed in Fig. 4.10. Following the previous observations, Wang et al. showed that 1D PtO_2 structures formed at Pt(332) steps ([6(111)×(111)] in step notation) exhibit higher CO oxidation activity than Pt surfaces covered with chemisorbed oxygen [92]. The fact that the formation of 1D PtO_2 structures was observed at relatively mild $1 \cdot 10^{-6}$ Torr oxygen partial pressure and 310 K surface temperature is essential for our experiment.

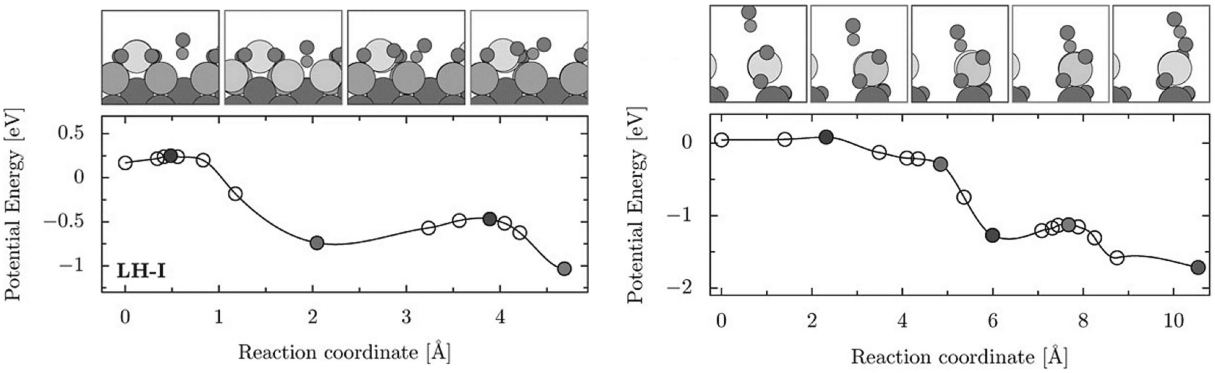

Fig. 4.10: *(left)* Reaction pathway of CO oxidation on Pt(110)-(12×2)-2O proceeding via Langmuir-Hinshelwood mechanism. *(right)* Reaction pathway of CO oxidation on the $(10\bar{1}0)$ facet of $\alpha - PtO_2$ oxide. Taken from [91].

4.2.6. Spatiotemporal patterns

The rate of CO oxidation by O_2 on Pt surface operated in a flow reactor under fixed external conditions may vary with time [93]. Depending on surface temperature T, CO partial pressure p_{CO}, O_2 partial pressure p_{O_2}, and crystallographic orientation of Pt surface, the rate of CO_2 production may turn from stationary to oscillatory or even chaotic behavior. Nonlinear dynamics of the CO_2 production on Pt surface is a direct consequence of the amount of chemisorbed reactants available to participate in the reaction. On the one hand, chemisorbed reactants are permanently consumed in Pt catalyzed CO oxidation. On the other hand, reactants from the gas phase are permanently supplied to the Pt surface. Depending on the adsorption sites and external conditions, chemisorbed molecules exhibit different diffusibility over the surface. Reaction-diffusion processes on the Pt surface may give rise to the formation of spatiotemporal patterns. Spatiotemporal patterns are com-

posed of CO and oxygen covered Pt surface areas of different sizes and shapes evolving in time. Specifically, rotating spirals, target patterns, moving wavefronts, and irregular structures denoted as chemical turbulences may be observed by nondestructive surface science techniques with good lateral (in the order of 10^0 µm) and temporal resolution (in the order of 10^0 s), see Fig. 4.11.

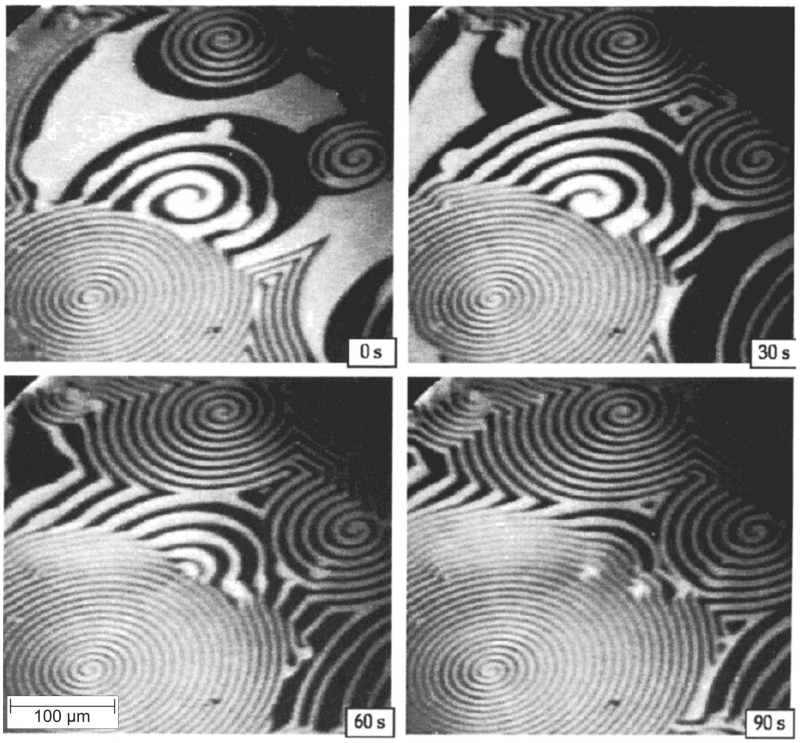

Fig. 4.11: Temporal evolution of rotating spirals observed by PEEM on Pt(110) at $T = 448\,\mathrm{K}$, $p_{\mathrm{CO}} = 4.3 \cdot 10^{-5}\,\mathrm{mbar}$, $p_{\mathrm{O_2}} = 4.0 \cdot 10^{-4}\,\mathrm{mbar}$. Bright areas are CO covered; dark areas are oxygen covered. Taken from [68].

Belousov-Zhabotinsky (BZ) reaction, discovered by Boris Belousov in 1951, is a famous example of nonlinear chemical oscillations [94]. Homogeneous autocatalytic oxidation of malonic acid by potassium bromate is a typical representative of BZ reaction, observable by the naked eye. Periodic color changes reflecting the varying composition of the solution show that chemical reactions do not necessarily have to proceed to equilibrium monotonically. What is more, if a continuous reactants inlet and products outlet in open systems, e.g., flow reactors, are ensured, oscillations may be sustained in thermodynamically stable states far from the equilibrium. The first rate oscillations in catalytic CO oxidation were observed by Wicke et al. in the early '70s [68]. A significant contributor to the more profound understanding of oscillatory kinetics in catalytic CO oxidation over Pt single-crystals is a German physicist Gerhart Ertl, awarded the Nobel prize for Chemistry in 2007. Simplicity and current level of knowledge make this reaction a model system of heterogeneous catalysis.

Kinetic oscillations on Pt single-crystal surfaces are conditioned by Pt crystallographic structure, which needs to be reconstructable when covered with chemisorbed reactants. Among three low Miller index planes, oscillations may be observed on Pt(100) and Pt(110), but not on Pt(111) surface. Assuming that CO molecules recombine on Pt surface with O atoms via Langmuir-Hinshelwood mechanism, the single oscillation on

Pt(110) surface proceeds as follows [68]: Initially CO-covered Pt(110) - 1×1 structure with O_2 sticking coefficient $s_{O,1\times1} = 0.6$ exhibits high catalytic activity. As a consequence of favored O_2 adsorption and increased CO consumption, CO-coverage declines. When CO-coverage falls below critical value of $\theta_{CO} = 0.2\,\mathrm{ML}$, Pt(110) - 1×1 reconstructs to Pt(110) - 1×2 structure with $s_{O,1\times2} = 0.3$–$+0.4$. CO adsorption on Pt(110) - 1×2 surface is favored over O_2 adsorption, and therefore CO coverage increases. When CO-coverage exceeds the critical value of $\theta_{CO} = 0.2\,\mathrm{ML}$, the reconstruction is lifted to Pt(110) - 1×1 structure, and initial conditions are reestablished. Theoretically calculated temporal evolution of surface coverages, surface reconstruction, reaction rate and CO partial pressure fluctuations are displayed in Fig. 4.12. Since Pt(111) surface does not reconstruct, oscillations cannot be observed on this structure.

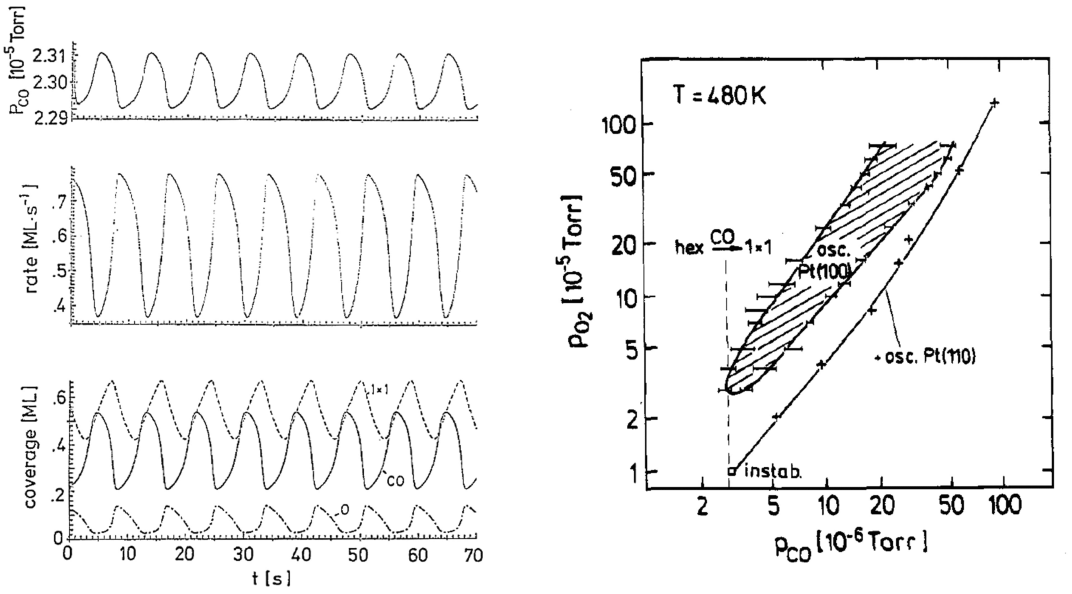

Fig. 4.12: *(left)* Theoretically calculated temporal evolution of surface coverages, surface reconstruction, reaction rate and CO partial pressure fluctuations during CO oxidation on Pt(110) at $T = 540\,\mathrm{K}$, $p_{CO} = 2.3 \cdot 10^{-5}\,\mathrm{mbar}$, $p_{O_2} = 5.0 \cdot 10^{-5}\,\mathrm{mbar}$. Taken from [93]. *(right)* Region in the pressure plane (p_{O_2}, p_{CO}) at $T = 480\,\mathrm{K}$ where rate oscillations on Pt(100) and Pt(110) occur. Taken from [68].

As already outlined, kinetic oscillations are conditioned by the crystallographic orientation of Pt surface, surface temperature T, CO partial pressure p_{CO}, and O_2 partial pressure p_{O_2}. The oscillation mechanism indicates that high Miller index planes composed of (100) and (110) terraces and steps, e.g., Pt(210) ([2(110)×(100)] in step notation), or high Miller index planes faceting to such structures allow CO_2 production rate oscillations. However, oscillation properties change with oxygen sticking coefficients. Pt(110) surface with $s_{O,1\times1}$ to $s_{O,1\times2}$ ratio of ca. 1.5 ($s_{O,1\times1} = 0.6$, $s_{O,1\times2} = 0.3-0.4$) exhibits regular oscillations while Pt(100) surface with $s_{O,1\times1}$ to $s_{O,hex}$ ratio of ca. 3 000 ($s_{O,1\times1} = 0.3$, $s_{O,hex} = 1 \cdot 10^{-4} - 1 \cdot 10^{-3}$) exhibits irregular oscillations. The amount of chemisorbed reactants is controlled by partial pressures and surface temperature. Chemical oscillations on Pt(110) surfaces exist for a narrow region in the pressure plane (p_{O_2}, p_{CO}). In contrast, chemical oscillations on Pt(100) surfaces exist for a significantly wider region in the pressure plane (p_{O_2}, p_{CO}), see Fig. 4.12. According to Imbihl and Ertl [68], the high

sensitivity of Pt(110) surface towards partial pressure changes causes better long-range synchronization of oscillating surfaces. Therefore, Pt(110) allows the creation of regular spatiotemporal patterns which cannot be observed on Pt(100). p_{CO} fluctuations caused by varying reaction rates are displayed in Fig. 4.12.

Mathematical modeling of spatiotemporal self-organization and associated rate oscillations in CO oxidation over Pt surfaces helps predict the system's behavior in various regions of the parameter space ($p_{\mathrm{O_2}}$, p_{CO}, T). Historically first model, also known as the KEE model, corresponding to the experimentally observed bistability and oscillations of Pt(110) surface coverages, was proposed by Krischer, Eiswirth, and Ertl in 1992 [95]. The system of three coupled ordinary differential equations (ODE) in the KEE model depends on three external control parameters, namely partial pressures $p_{\mathrm{O_2}}$, p_{CO}, and temperature T. A system of the first two ODEs (4.6), (4.7) for the temporal evolution of surface coverages θ_{CO} and θ_{O} correctly predicts hysteretic bistability displayed on Fig. 4.13. The temporal evolution of θ_{CO} in the ODE (4.6) depends on CO adsorption, CO desorption, and CO oxidation. The temporal evolution of θ_{O} in the ODE (4.7) depends only on O_2 adsorption and CO oxidation because O atoms at examined temperatures do not desorb. Adding the third ODE (4.8) for the temporal evolution of nonreconstructed surface fraction $w_{1\times1}$ allows a correct prediction of simple oscillations. Eq. (4.6)–(4.8) are taken from [96].

$$\frac{\partial\theta_{\mathrm{CO}}}{\partial t} = p_{\mathrm{CO}}k_{\mathrm{CO}}s_{\mathrm{CO}}\left(1-(\theta_{\mathrm{CO}}/\theta_{\mathrm{CO,sat}})^{q}\right) - k_{\mathrm{des}}\theta_{\mathrm{CO}} - k_{\mathrm{r}}\theta_{\mathrm{CO}}\theta_{\mathrm{O}} \tag{4.6}$$

$$\frac{\partial\theta_{\mathrm{O}}}{\partial t} = p_{\mathrm{O}}k_{\mathrm{O}}s_{\mathrm{O}}\left(1-\theta_{\mathrm{O}}/\theta_{\mathrm{O,sat}}-\theta_{\mathrm{CO}}/\theta_{\mathrm{CO,sat}}\right)^{2} - k_{\mathrm{r}}\theta_{\mathrm{CO}}\theta_{\mathrm{O}} \tag{4.7}$$

$$\frac{\partial w_{1\times1}}{\partial t} = k_{\mathrm{rec}}\left(f\left(\theta_{\mathrm{CO}}\right)-w_{1\times1}\right) \tag{4.8}$$

Here k_{CO}, k_{O} denote the impingement rates; s_{CO}, s_{O} are the sticking coefficients; $\theta_{\mathrm{CO,sat}}$, $\theta_{\mathrm{O,sat}}$ are the saturation coverages, k_{des} is a CO desorption rate, k_{r} is a reaction rate, factor $q = 3$ models the asymmetry in reactants adsorption caused by CO inhibition of O_2 adsorption, k_{rec} is a rate of surface reconstruction, and function $f\left(\theta_{\mathrm{CO}}\right)$ evaluates the influence of θ_{CO} on surface reconstruction. Temperature T affects parameters k_{r}, k_{des}, k_{rec}, which may be calculated by the Arrhenius equation. s_{O} is a linear combination of sticking coefficients for 1×1 and 1×2 structures. Ryzha and Gaiduchok further extended the KEE model with the fourth ODE for the temporal evolution of surface faceting and terms considering CO and O diffusion over the catalyst surface [97]. This improvement correctly predicts mixed-mode oscillations. Experimentally observed mixed-mode oscillations are displayed in Fig. 4.13. Bzovska and Mryglod [98] examined the existence of Hopf and Turing bifurcations in the parameter space. Their approach was based on extending the KEE model with one diffusion term for each ODE. The resulting equations had a form of reaction-diffusion equation [52]:

$$\frac{\partial u}{\partial t} = f\left(u\right)\cdot D\Delta u, \tag{4.9}$$

where D denotes diffusion coefficient. Hopf bifurcations lead to temporal pattern formation, while Turing bifurcations lead to spatial pattern formation. A computer simulation of spatiotemporal patterns proved the coexistence of both instabilities for the calculated region in the parameter space.

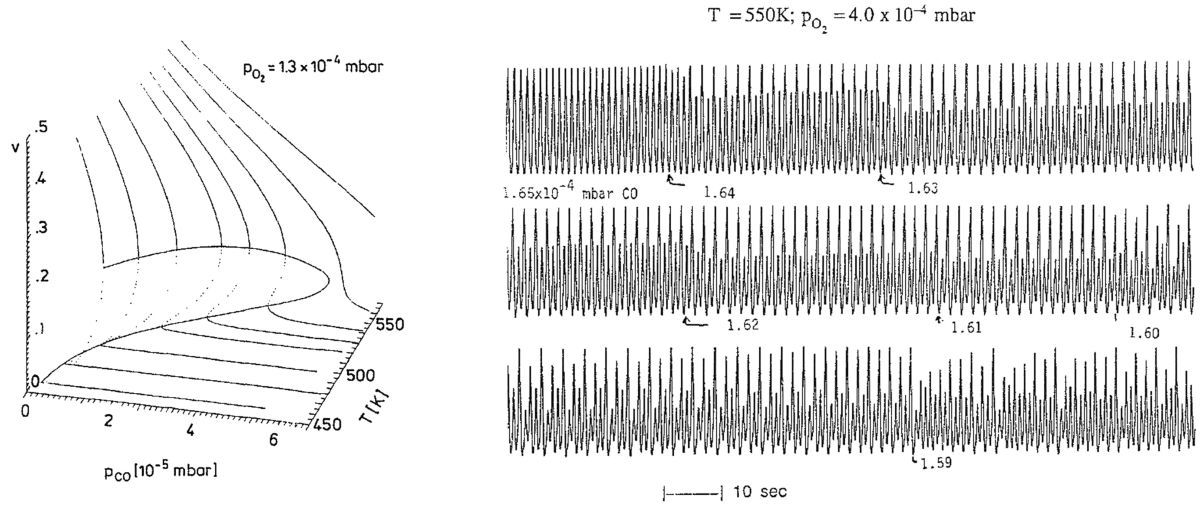

Fig. 4.13: *(left)* Theoretically calculated hysteretic behavior of oxygen coverage v on Pt(110) at fixed p_{O_2} and varying T, p_{CO}. Taken from [95]. *(right)* Transition from harmonic rate oscillations to chaotic rate oscillations in CO oxidation on Pt(110) at fixed T, p_{O_2}, and varying p_{CO}. Taken from [93].

Experimental studies of nonlinear phenomena during CO oxidation over Pt surfaces may be divided into spatially nonresolved observations and spatially resolved observations. Spatially nonresolved experiments are generally not limited by ambient pressures. On the other hand, instruments used in spatially resolved experiments usually require pressures below $1 \cdot 10^{-2}$ mbar. Oscillating CO_2 partial pressure is typically monitored by mass spectrometry or gas chromatography. The heat released at various stages of the reaction may be monitored by thermocouple or pyrometer. Fourier transform infrared spectroscopy (FTIR) may be employed for surface coverage monitoring. Changes in the crystallographic orientation of the catalyst surface are typically observed by low energy electron diffraction (LEED). In order to monitor patterns of varying surface coverage, spatial resolution in the order of 10^0 µm needs to be achieved. Time-evolving surface patterns require temporal resolution in the order of 10^0 s. The negative effect of the probe on chemisorbed reactants should be minimized. Historically first technique used for spatiotemporal patterns monitoring on Pt(100) surfaces was scanning LEED microscopy with a spatial resolution of 1 mm [99]. This approach allowed spatiotemporal monitoring of $1\times1 \leftrightarrows$ hex transition waves. Scanning LEED microscopy was soon replaced with photoemission electron microscopy (PEEM) with a temporal resolution of 20 ms and a spatial resolution in the order of 10^2 nm [93]. The amount of electrons leaving the sample surface in PEEM is inversely proportional to the work function of the surface overlayer. The study of spatiotemporal patterns on Pt(100) surface at elevated pressure (8 Pa) was published by Lele et al. [100]. For this purpose, ellipsomicroscopy for surface imaging (EMSI) was employed. The highest spatial resolution of 20 Å was achieved in the field electron microscopy (FEM) and field ion microscopy (FIM) experiments [68]. Due to a low temporal resolution, scanning tunneling microscopy (STM) is not used in the research of spatiotemporal patterns on Pt.

4.3. Experiment

In this work, we present the first observation of spatiotemporal patterns, formed during CO oxidation by O_2 on Pt surfaces, using the TOF-SIMS technique. The experimental part consists of sample preparation, ultrahigh vacuum scanning electron microscopy (UHV-SEM) measurements, and time-of-flight secondary ion mass spectrometry (TOF-SIMS) measurements. Electron backscatter diffraction (EBSD) measurements were performed by doc. Ing. Miroslav Kolíbal, Ph.D.

4.3.1. Sample preparation

Pt wire with 100 µm in diameter was used as a catalyst sample. Around 5 cm long piece of the wire was cut and formed into a U-shape to minimize sample wrinkling and shifting from the microscope field of view caused by thermal expansion. The U-shaped wire was subsequently pressed in the press from the IONTOF company to form a flat and smooth surface, see Fig. 4.14. So prepared sample was inserted into the UHV-SEM sample holder, which allows sample resistive heating in the main chamber of the microscope, see Fig. 4.14.

Fig. 4.14: *(left)* Press from the IONTOF company used for sample preparation. *(right)* UHV-SEM sample holder with Pt sample inserted. The sample holder allows resistive sample heating in the main microscope chamber.

A whole sample cleaning procedure was carried out in the main chamber of the UHV-SEM instrument from the TESCAN company, see Fig. 4.15. The microscope was developed as a part of the project AMISPEC [101]. In order to remove impurities introduced to the sample surface during the pressing, the sample was annealed at around 1 000 °C in the H_2/O_2 surrounding atmosphere. A pyrometer monitored the surface temperature. H_2 partial pressure in the main chamber of the microscope was set to $1 \cdot 10^{-5}$ Pa, O_2 partial pressure was set to $1 \cdot 10^{-4}$ Pa. During the whole cleaning procedure, the sample was imaged with an electron microscope. The surface was scanned with a 5 keV/5 nA electron probe, and secondary electrons were detected by an Everhart-Thornley detector. If the sample remained contaminated even at temperatures close to the Pt melting point, the surface was sputtered with 5 keV argon ions. A micrograph of the clean surface is displayed in Fig. 4.16. A typical sample is composed of multiple grains with different crystallographic orientations. Desired Pt grain size is in the order of 10^2 µm. Annealing in an O_2 atmosphere allows the controllable growth of grains. The crystallographic orientation of grains was determined by EBSD measurements.

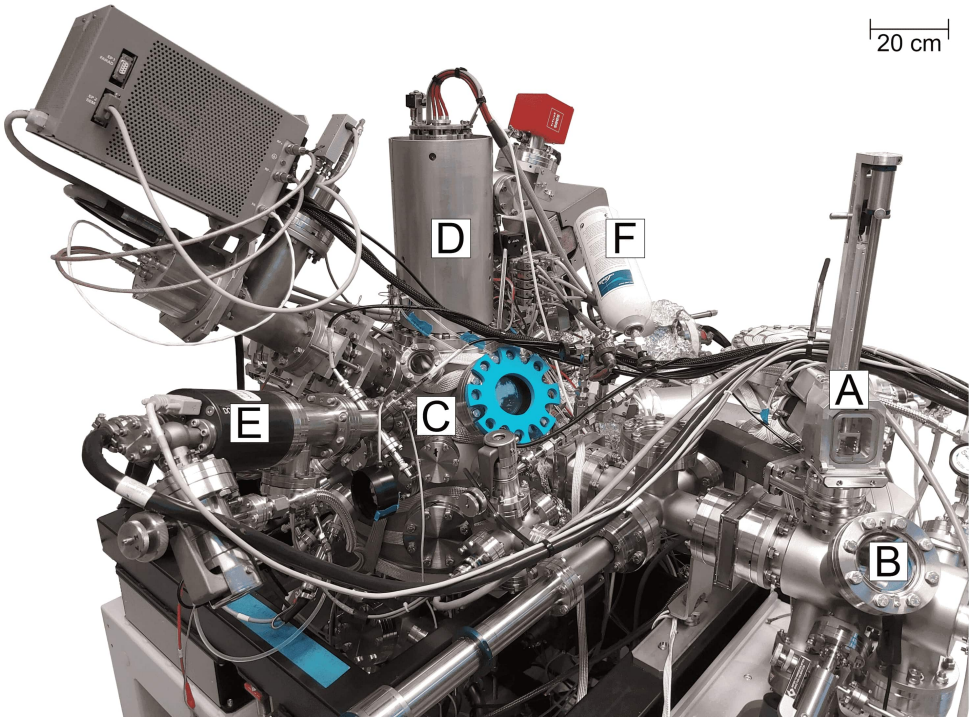

Fig. 4.15: UHV-SEM instrument. A – airlock chamber; B – loadlock chamber; C – main chamber; D – electron gun; E – sputter gun; F – gas feeding system.

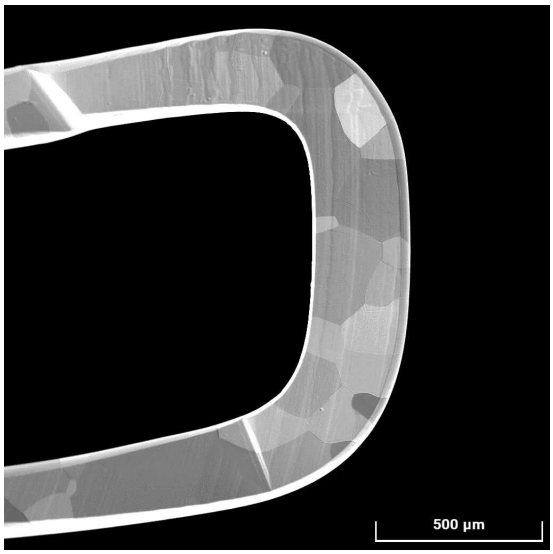

Fig. 4.16: Micrograph of clean Pt sample. The image was taken by UHV-SEM.

4.3.2. UHV-SEM experiments

To make things clear, UHV-SEM and TOF-SIMS instruments are not interconnected. Therefore, samples are necessarily exposed to the ambient atmosphere when transferred. Another noteworthy piece of information is that the TOF-SIMS is equipped only with an ion gun, and no other less destructive imaging method is available in this instrument. Therefore, the primary aim of UHV-SEM experiments was to find a region in the parameter space (p_{O_2}, p_{CO}, T) without significant surface damage, where spatiotemporal patterns

may be observed. Since EBSD measurements revealed exclusively high Miller index planes on the prepared sample, grains with suitable crystallographic orientation had to be found as well. Last but not least, imaging with electrons provides better spatial resolution than imaging with ions, which makes the process of looking for spatiotemporal patterns on Pt surface easier.

The vacuum system of the UHV-SEM instrument allows reaching a base pressure of $1 \cdot 10^{-7}$ Pa in the main microscope chamber. Ultrahigh vacuum initial conditions ensure minimal surface contamination with unwanted residual gases. Maximal allowed pressure in the main chamber during the electron microscope operation reaches $1 \cdot 10^{-2}$ Pa. However, the limitation in our case is a maximal pressure allowed in the TOF-SIMS instrument, which is slightly lower and reaches $3 \cdot 10^{-3}$ Pa. The first iteration in the process of looking for a suitable p_{O_2}/p_{CO} partial pressures ratio is based on the parameter space diagram displayed in Fig. 4.12. CO partial pressure is set to $2 \cdot 10^{-4}$ Pa and remains constant. O_2 partial pressure is initially set to $1 \cdot 10^{-3}$ Pa and will be further adjusted. During the gas flooding, the surface temperature is kept constant at 200 °C. This approach should protect the surface from CO poisoning occurring at low temperatures. During the whole procedure, the sample surface is scanned with a 5 keV/5 nA electron probe, and an Everhart-Thornley detector detects secondary electrons. The scanning proceeded with a temporal resolution of 6 seconds per scan. The next step is a gradual p_{O_2} raising until chemical waves on the catalyst surface are spotted. Different Pt surface coverages exhibit different emissivity of secondary electrons, which turns out in the surface brightness. Since the chemical wave creation is conditioned by three parameters, namely p_{O_2}, p_{CO} partial pressures, and temperature T, two parameters need to be varied simultaneously. In our approach, sample temperature is permanently ramping up and down between 125 – 250 °C with the ramping speed of 2 °C.s^{-1}. Pt wire is heated resistively by an electric current running directly through the sample. The temperature ramping may be controlled either manually or automatically from the control software. The surface temperature is monitored by a pyrometer. O_2 floods into the main chamber through a manually controlled needle valve. Since only a small fraction of Pt grains has a suitable crystallographic orientation for regular spatiotemporal pattern creation, the sample needs to be imaged with a wide field of view in order to find the right grains. The experience has shown that the surface gradually loses its activity towards chemical wave creation. Therefore, the surface needs to be from time to time reactivated by flash heating to temperatures around 1 000 °C. Partial pressures do not need to be changed before the flash heating.

Two types of chemical waves may be observed on Pt surfaces. The first type of waves occurs when surface coverage turns from CO to oxygen, or vice versa, and indicates that p_{O_2}, p_{CO} partial pressures are balanced for given temperature T. Such chemical waves do not require Pt surface reconstructability and therefore may be observed on the vast majority of grains. The second type of waves are self-sustained spatiotemporal patterns, which occur only on reconstructable surfaces at the well-defined temperature and p_{O_2}, p_{CO} partial pressures. The process of looking for spatiotemporal patterns on Pt surfaces continues with the first type of wave stabilization. p_{O_2}/p_{CO} partial pressures ratio is kept constant, and the surface temperature is manually fine-tuned. The goal is to reach the state when CO and oxygen coverages coexist on one grain. When the coexistence of two coverages is established, all three parameters (p_{O_2}, p_{CO}, T) may be further fine-tuned in order to find the state when both coverages spatially move. This state may be, however, reached only on surfaces with suitable crystallographic orientation. Numerous experiments have

shown that regular spatiotemporal patterns may be observed at 170 °C surface temperature, $3.0 \cdot 10^{-4}$ Pa CO partial pressure, and $1.5 \cdot 10^{-3}$ Pa O_2 partial pressure. Results of UHV-SEM experiments are presented in Sec. 4.4.1.

4.3.3. TOF-SIMS experiments

Static SIMS measurements were carried out in the TOF.SIMS 5 instrument from the IONTOF company, see Fig. 4.17. Minor modifications of the instrument were required in order to study CO oxidation on the Pt wire inserted into the UHV-SEM sample holder. TOF-SIMS instrument is equipped with a software-controlled O_2 feeding; however, CO feeding had to be installed. For this purpose, a needle valve with a CO bottle was attached to the load lock chamber. During the experiment, the gate valve between the main chamber and the load lock chamber stays open. The outlet of the instrument's rotary pump was connected to a laboratory gas disposal system. Otherwise, the permanently pumped down CO gas from the main chamber would contaminate the laboratory workplace. The minimal sample handling is ensured by a direct UHV-SEM sample holder attachment to the TOF-SIMS sample holder, see Fig. 4.18. Sample heating is provided by an electric current running directly through the Pt wire. Temperature monitoring is carried out by a chromel-alumel thermocouple touching the lower sample surface right beneath the analyzed area.

After the sample cleaning, identifying active grains, and finding external conditions (p_{O_2}, p_{CO}, T) favorable for spatiotemporal patterns, the sample was transferred from the UHV-SEM to the TOF-SIMS instrument. Surface contamination induced during the sample exposure to the ambient atmosphere was removed by short annealing at 1 000 °C in $1 \cdot 10^{-4}$ Pa O_2 surrounding atmosphere. The quick cleaning procedure was followed by CO gas introduction to the partial pressure of $3.0 \cdot 10^{-4}$ Pa and O_2 gas introduction to the partial pressure of $1.5 \cdot 10^{-3}$ Pa. During the gas feeding, the sample was kept at 200 °C to avoid CO surface poisoning. Base pressure in the order of 10^{-7} Pa ensured minimal surface contamination with unwanted residual gases. 30 keV Bi^+ ions performed surface imaging. Low probe current in the order of 10^1 pA, on the one hand, minimized ion-induced surface damage and, on the other hand, provided a sufficient signal of secondary ions. The square surface area with 300 µm in length was analyzed at 256×256 points in random scan mode. The temporal resolution of the measurement was 4 seconds per scan. A reflectron-equipped time-of-flight mass spectrometer analyzed negative secondary ions from a mass range of 1 – 320 amu. The final step before spatiotemporal patterns observation was to set a proper surface temperature. Although the UHV-SEM experiment predetermined the proper surface temperature to 170 °C, this value could slightly change due to the measurement uncertainty or small deviation in partial pressures. The procedure of temperature fine-tuning is based on the momentary change in CO and O_2 coverages integrated over the active grain surface. Since both coverages should coexist on the active grain, spatiotemporal patterns may be observed near the steep edge of CO/O_2 coverage change, measured by TOF-SIMS instrument. Results of TOF-SIMS experiments are presented in Sec. 4.4.2.

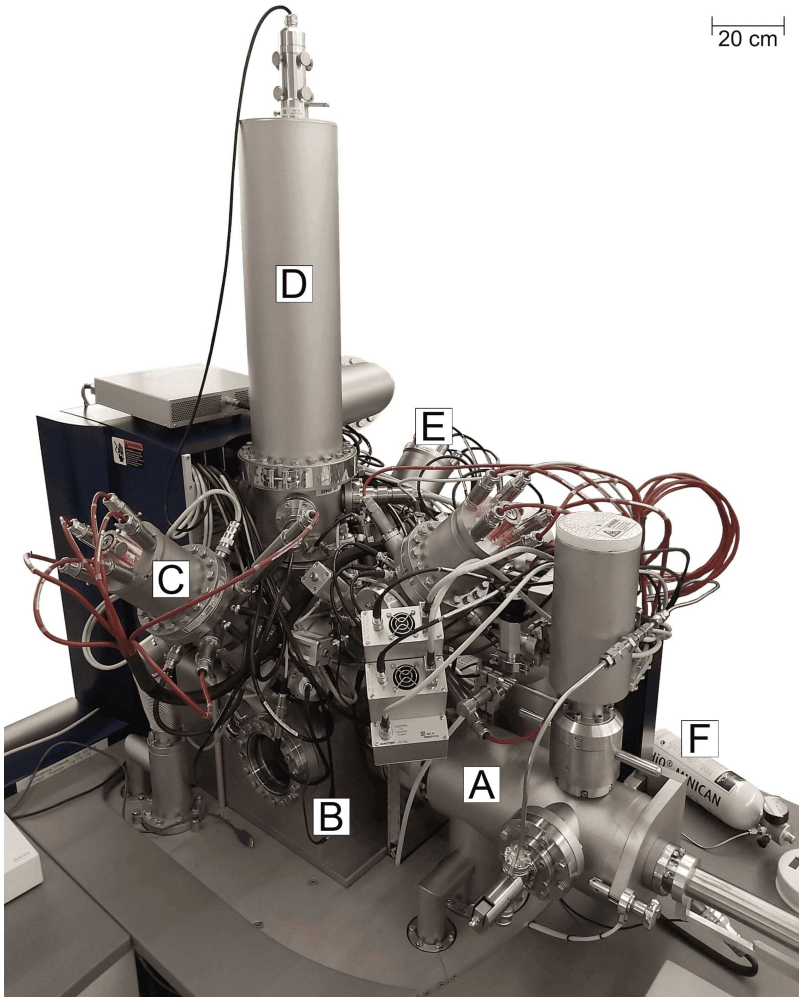

Fig. 4.17: TOF.SIMS 5 instrument. A – loadlock chamber; B – main chamber; C – primary ion gun; D – time-of-flight mass spectrometer equipped with reflectron; E – sputter gun; F – gas feeding system.

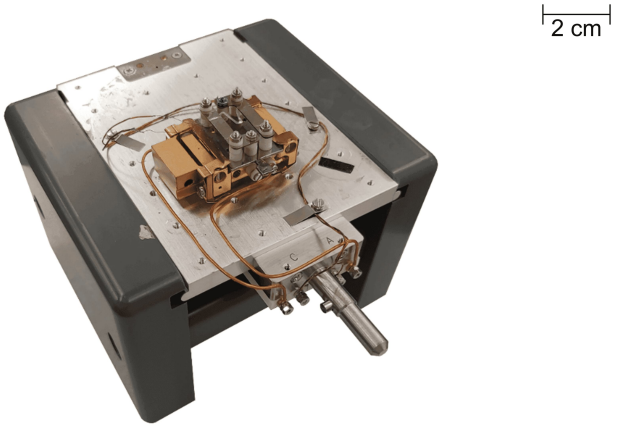

Fig. 4.18: TOF-SIMS sample holder with UHV-SEM sample holder attached. The sample holder allows resistive sample heating in the main microscope chamber and temperature monitoring by chromel-alumel thermocouple.

4.4. Results

The results of our research may be divided into three parts. In the first part, spatiotemporal patterns observed by the UHV-SEM instrument during CO oxidation on the polycrystalline Pt samples are presented. Sufficient spatial and temporal resolution gives better insight into the reaction dynamics; however, the information about the surface elemental composition is absent. In the second part, spatiotemporal patterns observed by the TOF-SIMS instrument are presented. Despite the considerably worse lateral resolution, spatiotemporal patterns with sufficient temporal resolution may still be recognized. The surface elemental composition may be derived from the signal of secondary ions. In the last part, temperature-programmed TOF-SIMS experiments are correlated with temperature--programmed UHV-SEM experiments. Based on the signal of secondary ions at various surface temperatures, the surface elemental composition may be assigned to the brightness observed by the UHV-SEM instrument. Our research demonstrates that SIMS monitoring of reaction-diffusion processes on catalyst surfaces is possible even after long-term observations (several hours) when ion dose is beyond the static SIMS limit.

4.4.1. UHV-SEM results

Spatiotemporal patterns of various shapes observed by the UHV-SEM instrument at 170 °C, $3.0 \cdot 10^{-4}$ Pa CO partial pressure, and $1.5 \cdot 10^{-3}$ Pa O_2 partial pressure are displayed in Fig. 4.19. While reconstructable grains allow the creation of regular rotating spirals, nonreconstructable grains remain permanently CO or O_2 covered. Bright areas within the active grains are CO covered, dark areas within the active grains are oxygen covered. The coverage of steady-state grains may be determined by comparing the brightness at different temperatures (will be discussed in the temperature programed TOF-SIMS section). Besides the identification of external parameters (p_{O_2}, p_{CO}, T) suitable for rate oscillations, UHV-SEM experiments gave us a deeper understanding of the pattern dynamics. According to the review paper of Imbihl and Ertl [68], rotating spirals are usually pinned to surface defects, which determine their rotation period. Unpinning from defects is possible upon external parameter variation. In our observations, spirals were usually formed after binding of directly moving waves to unspecified points on the surface. As a result, waves began to rotate around these points, see. Fig. 4.20. Chemical waves were typically created on grain boundaries or macroscopic surface defects, e.g., grooves after pressing.

A detailed temporal evolution of rotating spirals on Pt surfaces is displayed in Fig. 4.21 and Fig. 4.22. EBSD measurements revealed Pt(4,1,10) crystallographic orientation on the active grain in these figures. Typically, spatiotemporal patterns in the UHV-SEM instrument could be observed for about 50 minutes. After this time, the grain coverage turns into a stable state. During the spiral's lifetime, three distinct regimes were identified. In the beginning, unevenly shaped chemical waves created mainly on the grain boundaries chaotically move over the catalyst surface. When the waves get bonded to the surface defects, crooked rotating spirals composed of wide strips are formed. In the second phase, regular rotating spirals spread across the grain surface. The stripes are getting gradually narrower and denser. In the last stage, rotating spirals slowly disappear. The mechanism of the pattern's disappearance is unknown. Possible reasons are surface faceting or surface poisoning with strongly bonded species. The duration of identified stages may vary.

For example, the longest-lasting part in Fig. 4.22 is the phase of regular rotating spirals, while in Fig. 4.21, the formation phase took significantly longer than the phase of regular rotating spirals. Disappearing spirals can be partially restored by elevation of external parameters (p_{O_2}, p_{CO}, T). The stripes get suddenly wider, but the gradual narrowing continues. Total recovery is possible as well, but completely new patterns will be formed.

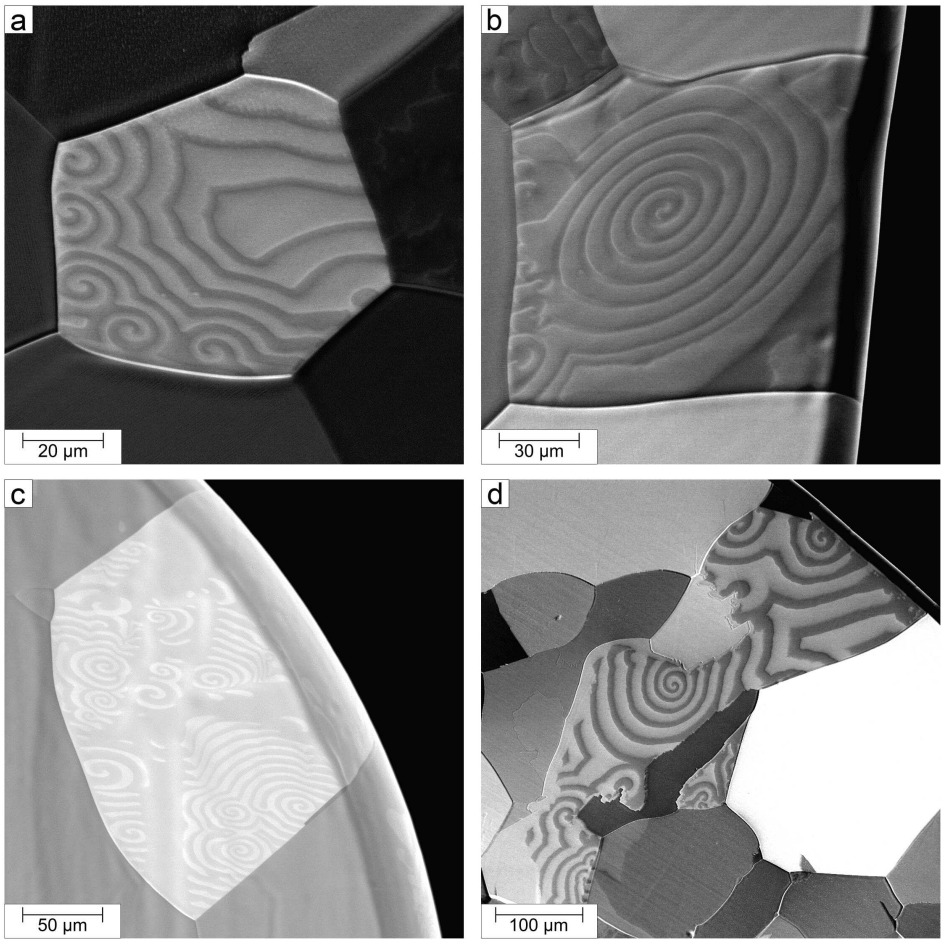

Fig. 4.19: Various regular spatiotemporal patterns observed by UHV-SEM at $T = 170\,°C$, $p_{CO} = 3.0 \cdot 10^{-4}\,Pa$, $p_{O_2} = 1.5 \cdot 10^{-3}\,Pa$. Bright areas are CO covered; dark areas are oxygen covered.

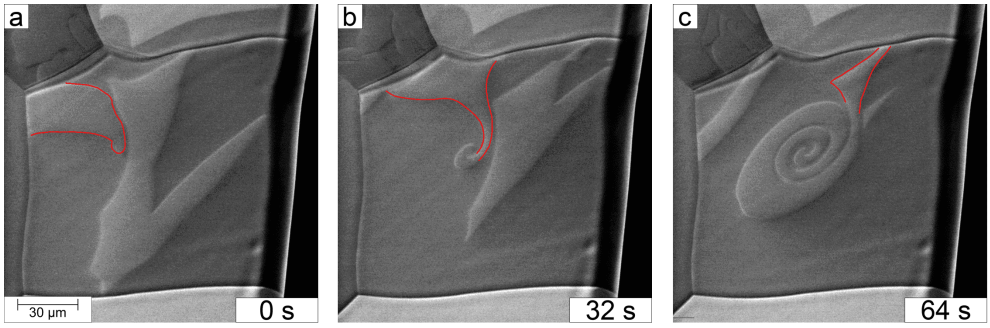

Fig. 4.20: Temporal evolution of the rotating spiral formation at $T = 170\,°C$, $p_{CO} = 3.0 \cdot 10^{-4}\,Pa$, $p_{O_2} = 1.5 \cdot 10^{-3}\,Pa$. Bright areas are CO covered; dark areas are oxygen covered. Red lines highlight the original wave created on the grain boundary. The same spiral is also displayed in Fig. 4.19b.

The recovery procedure consists of rapid surface heating to ca. $T = 1\,000\,°C$, followed by rapid cooling to the room temperature and subsequent gradual heating to a final temperature of ca. $T = 170\,°C$. During this process, partial pressures are kept constant. Flash heating activates the surface by removing adsorbed molecules, while rapid cooling and gradual heating to $T = 170\,°C$ enabled CO adsorption.

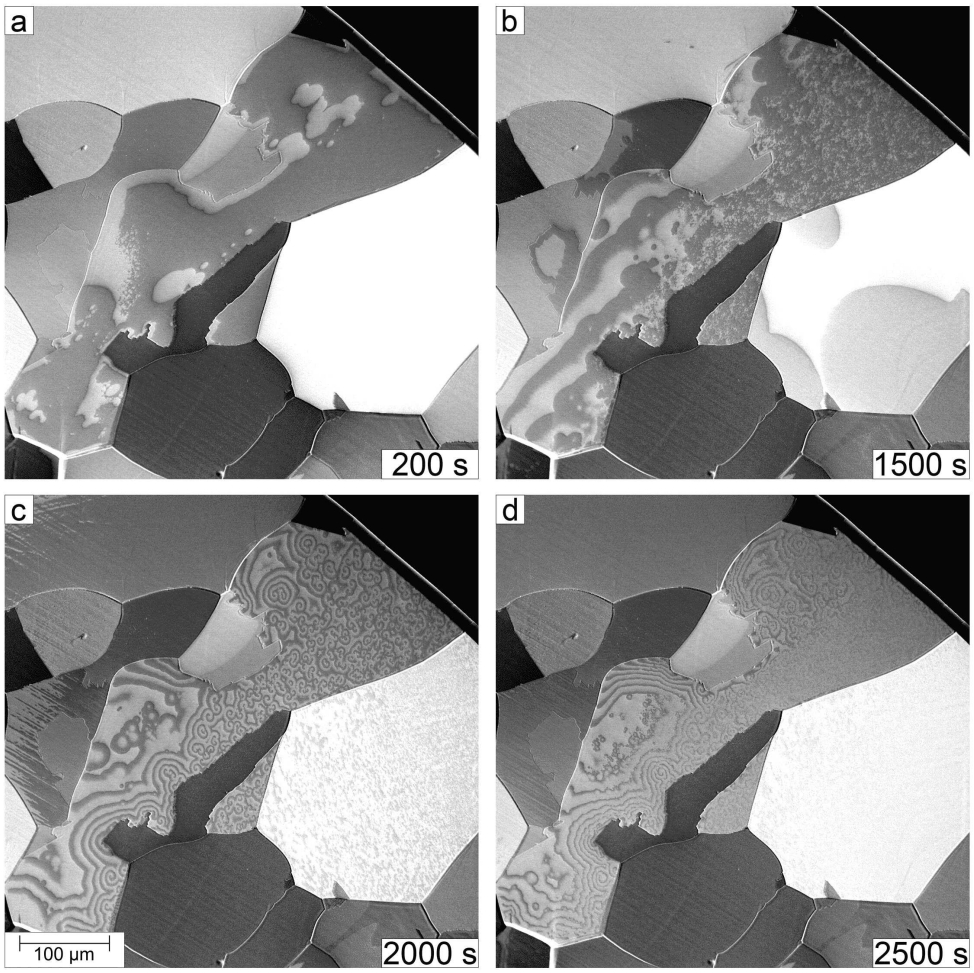

Fig. 4.21: Temporal evolution of spatiotemporal patterns on Pt(4,1,10) surface at $T = 170\,°C$, $p_{CO} = 3.0 \cdot 10^{-4}\,Pa$, $p_{O_2} = 1.5 \cdot 10^{-3}\,Pa$. Bright areas are CO covered; dark areas are oxygen covered. Three phases may be identified: a – b: formation of patterns; c: regular patterns; d: disappearing patterns.

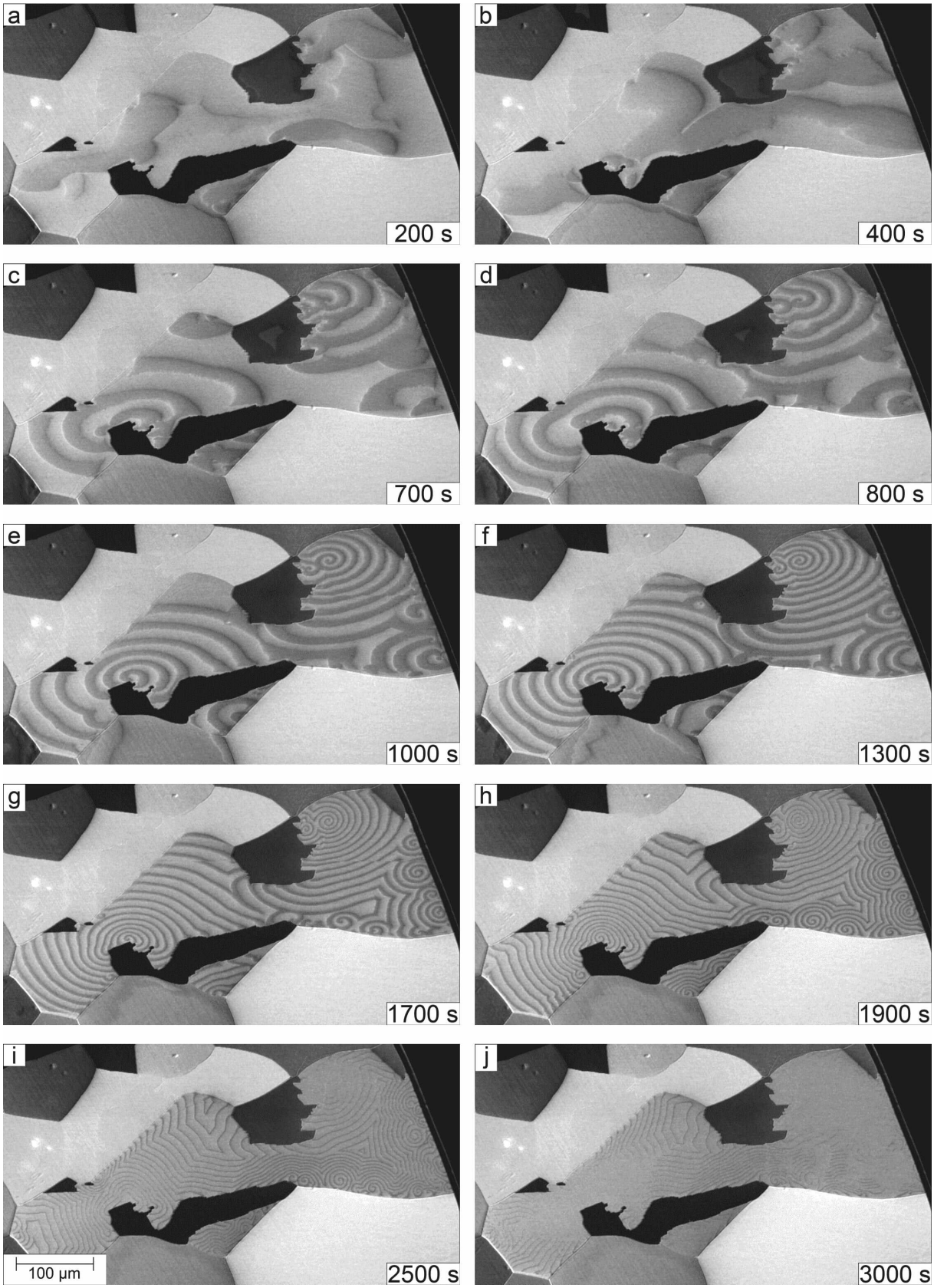

Fig. 4.22: Temporal evolution of rotating spirals on Pt(4,1,10) surface at $T = 170\,^{\circ}\mathrm{C}$, $p_{\mathrm{CO}} = 3.0 \cdot 10^{-4}\,\mathrm{Pa}$, $p_{\mathrm{O_2}} = 1.5 \cdot 10^{-3}\,\mathrm{Pa}$. Bright areas are CO covered; dark areas are oxygen covered. Three phases may be identified: a – b: formation of spirals; b – h: regular rotating spirals; i – j: disappearing rotating spirals.

4.4.2. TOF-SIMS results

External parameters during TOF-SIMS measurements were identical with external parameters during UHV-SEM measurements ($T = 170\,°C$, $p_{CO} = 3.0 \cdot 10^{-4}\,Pa$, $p_{O_2} = 1.5 \cdot 10^{-3}\,Pa$). TOF-SIMS mass spectrum analysis revealed that oxygen coverage is well represented by the peak located on PtO_2^- mass, and CO coverage is well represented by the sum of peaks located on C_2^-, C_2H^-, and $C_2H_2^-$ masses. The correctness of this finding is proven by spatial maps, where both coverages represented by corresponding signals of secondary ions appear complementary. Another proof is a temperature-programmed TOF-SIMS measurement, where CO coverage occurs at low temperatures, while oxygen coverage occurs at higher temperatures. Both proofs will be further supported with the following results.

Fig. 4.23a displays the area of the sample explored both in the UHV-SEM experiments and TOF-SIMS experiments. Individual grains are labeled with letters (A–N). The active grain with crystallographic orientation (4,1,10) is labeled with the letter D. Fig. 4.23b shows grains, which remain throughout the observation of spatiotemporal patterns on the active grain CO covered, while Fig. 4.23c shows oxygen covered grains. Coverages in Fig. 4.23b and Fig. 4.23c are complementary. The temporal evolution of spatial patterns observed by TOF-SIMS on the active grain is displayed in Fig. 4.24. Oxygen coverage is represented by red color; CO coverage is represented by green color. Pixel density is proportional to the surface coverage. A full white line highlights the moving wavefront, which we want to point out, and white arrows indicate the direction in which the wave proceeds between displayed frames. A dashed white line delimits the area without chemisorbed reactants removed by passing oxygen wave.

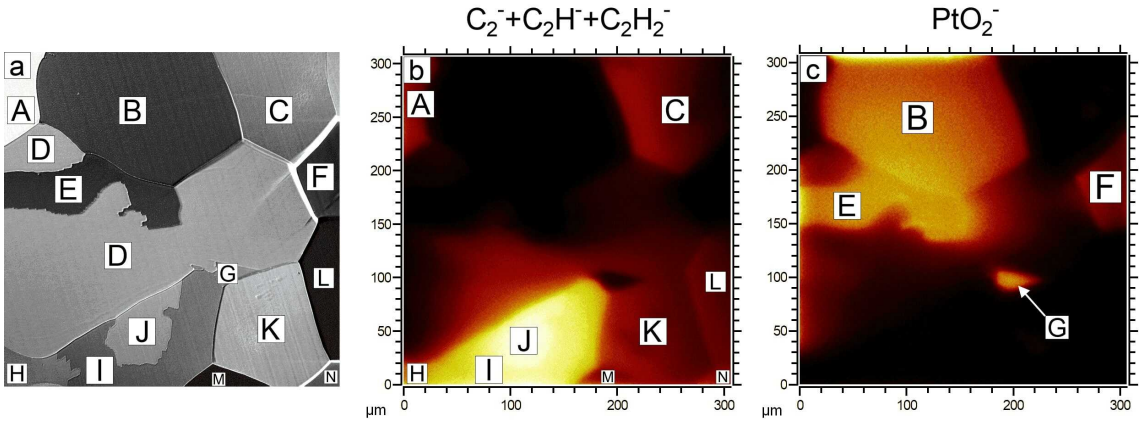

Fig. 4.23: Map of examined sample. a: electron micrograph with labeled grains (A – N). Grain D is an active Pt(4,1,10) grain displayed in Fig. 4.21 and Fig. 4.22. b: TOF-SIMS map of permanently CO covered grains. CO coverage is proportional to $C_2^- + C_2H^- + C_2H_2^-$ signal. c: TOF-SIMS map of permanently oxygen covered grains. Oxygen coverage is proportional to PtO_2^- signal.

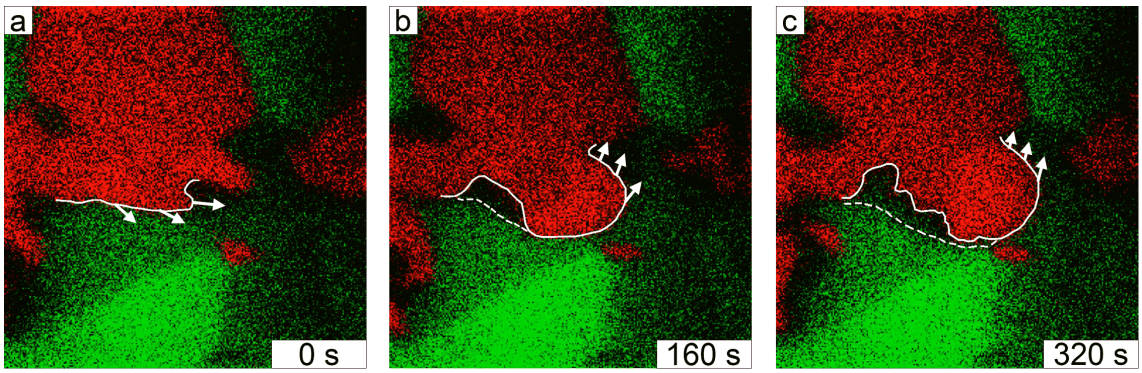

Fig. 4.24: Temporal evolution of patterns observed on an active Pt(4,1,10) grain at $T = 170\,°C$, $p_{CO} = 3.0 \cdot 10^{-4}\,Pa$, $p_{O_2} = 1.5 \cdot 10^{-3}\,Pa$. Green areas are CO covered; red areas are oxygen covered. Electron micrograph of the sample for easier identification of grain boundaries is displayed in Fig. 4.23a. A full white line highlights the moving wavefront; white arrows indicate the direction in which the wave proceeds between frames; a dashed white line delimits the area almost without chemisorbed reactants.

A detailed temporal evolution of spatial patterns observed on the active Pt(4,1,10) grain is displayed in Fig. 4.25. Numbers 1–6 in Fig. 4.25a–i label periodically moving oxygen stripes. Comparison of UHV-SEM measurements with TOF-SIMS measurements reveals two main differences. Firstly, no regular spatiotemporal patterns were observed by the TOF-SIMS instrument. The highest regularity was observed during the periodic stripes occurrence. Secondly, spatiotemporal patterns in the TOF-SIMS instrument were sustained for a significantly longer period of time than 50 minutes. The operator terminated the longest run in the TOF-SIMS instrument after 3.5 hours. The correct explanation of extended activity is unknown. A possible reason may be the permanent sputtering of poisoning species from the catalyst surface by scanning ion probe (30 keV Bi^+).

Fig. 4.25 also shows that oxygen coverage on the active grain exhibits higher mobility than chemisorbed CO. Oxygen waves originate from oxygen covered grains. After disconnecting from oxygen covered grains, oxygen waves gradually vanish. On the other hand, CO molecules gradually form a uniform coverage of the active grain outside oxygen covered region. This behavior is well observable on the Pt surface cleaned by passing oxygen wave, which gets subsequently uniformly covered by chemisorbed CO molecules from the gas phase and not by CO molecules from the CO wave. Integration of signals proportional to CO and oxygen coverages in the region where periodic stripes were observed reveals the oscillatory behavior of both surface coverages, see Fig. 4.26.

Another example of spatiotemporal patterns during CO oxidation on Pt surface observed by TOF-SIMS is displayed in Fig. 4.27. EBSD measurements revealed Pt(1,2,7) crystallographic orientation of the active grain. A temporal evolution clearly shows the gradual declination of oxygen coverage. Initially, declining oxygen gets concentrated to the spots highlighted by white arrows in Fig. 4.27e. Subsequently, spots with enhanced oxygen concentration move to the grain boundary highlighted by a white arrow in Fig. 4.27g. In the end, oxygen from the grain boundary is transferred to the oxygen covered grain, which may be easily identified in Fig. 4.27l. Temporal evolution in Fig. 4.27 also shows uniform chemisorption of CO molecules onto clean Pt surface, which was left behind a declining oxygen coverage.

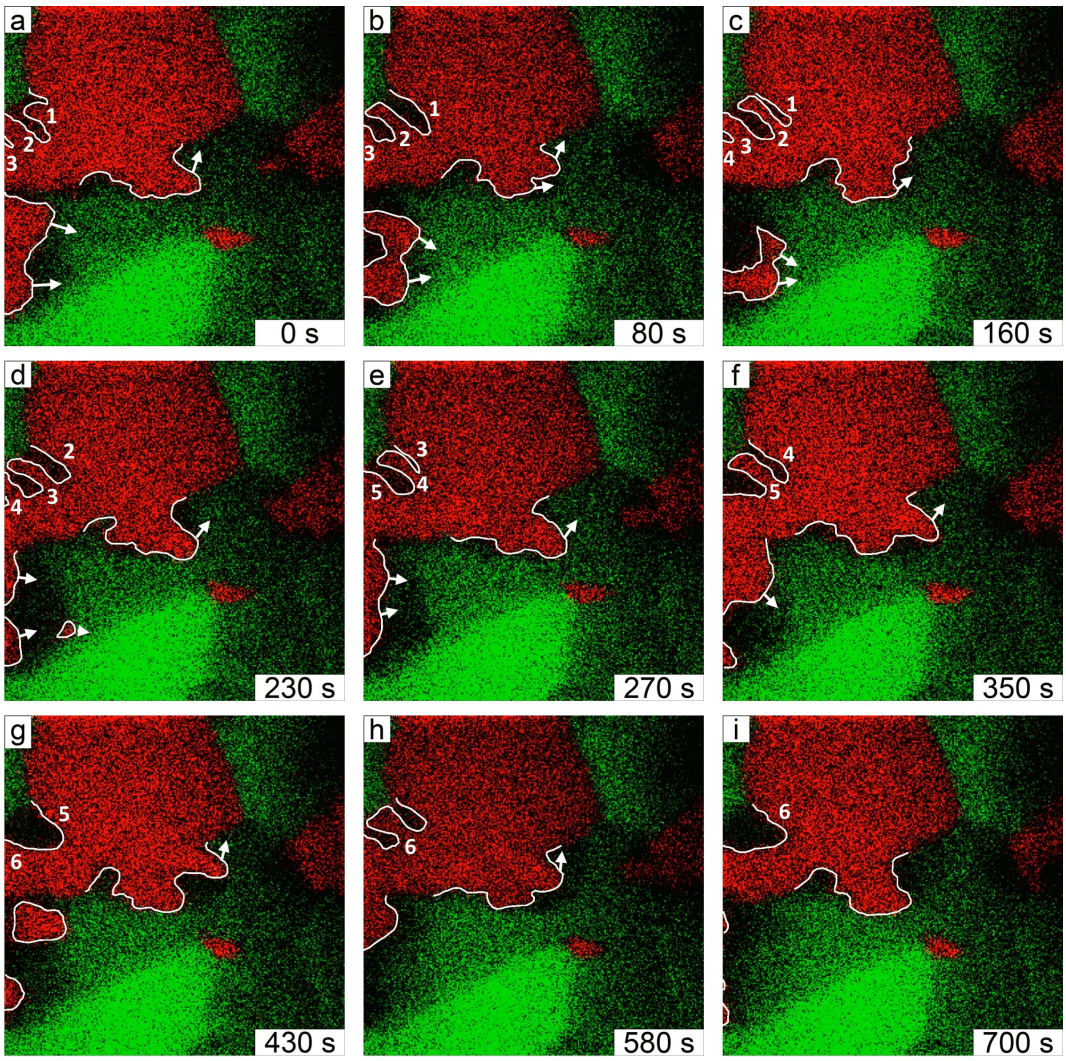

Fig. 4.25: Temporal evolution of patterns observed on an active Pt(4,1,10) grain at $T = 170\,^{\circ}\mathrm{C}$, $p_{\mathrm{CO}} = 3.0 \cdot 10^{-4}\,\mathrm{Pa}$, $p_{\mathrm{O_2}} = 1.5 \cdot 10^{-3}\,\mathrm{Pa}$. Green areas are CO covered; red areas are oxygen covered. Electron micrograph of the sample for easier identification of grain boundaries is displayed in Fig. 4.23a. A full white line highlights the moving wavefront; white arrows indicate the direction in which the wave proceeds between frames; white numbers (1 – 6) label periodically moving oxygen stripes.

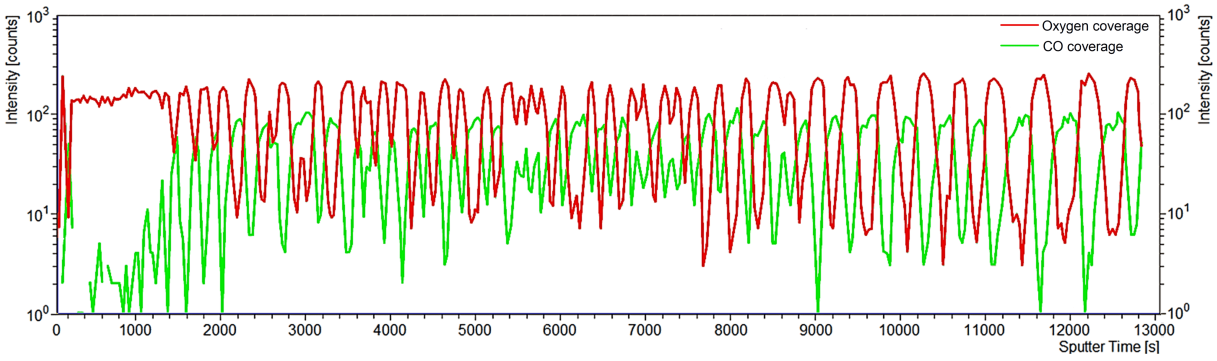

Fig. 4.26: Oscillations of CO (green curve) and oxygen (red curve) coverage on an active Pt(4,1,10) grain at $T = 170\,^{\circ}\mathrm{C}$, $p_{\mathrm{CO}} = 3.0 \cdot 10^{-4}\,\mathrm{Pa}$, $p_{\mathrm{O_2}} = 1.5 \cdot 10^{-3}\,\mathrm{Pa}$.

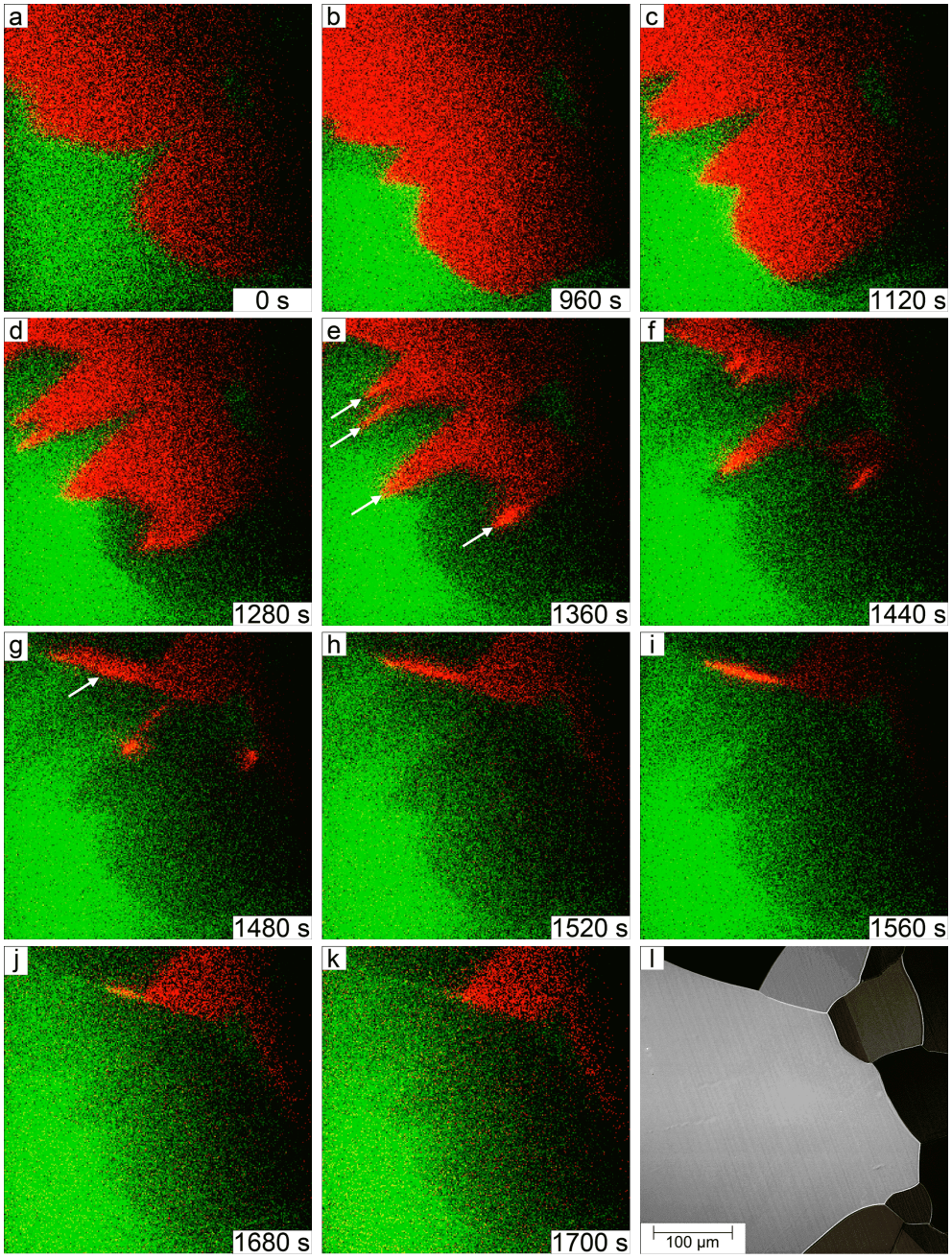

Fig. 4.27: Temporal evolution of declining oxygen wave observed on an active Pt(1,2,7) grain at $T = 170\,°C$, $p_{CO} = 3.0 \cdot 10^{-4}\,Pa$, $p_{O_2} = 1.5 \cdot 10^{-3}\,Pa$. Green areas are CO covered; red areas are oxygen covered. l: electron micrograph of the sample for easier identification of grain boundaries. White arrows highlight spots with concentrated oxygen.

4.4.3. Temperature programmed TOF-SIMS/UHV-SEM results

The primary aim of temperature-programmed TOF-SIMS/UHV-SEM experiments was to assign the elemental composition of surface coverage to the surface brightness observed by UHV-SEM. Therefore, two identical experiments were performed. One in the UHV-SEM instrument, another in the TOF-SIMS instrument. Partial pressures were set to values favorable for spatiotemporal pattern creation ($p_{CO} = 3.0 \cdot 10^{-4}\,Pa$, $p_{O_2} = 1.5 \cdot 10^{-3}\,Pa$). The surface temperature was ramping up and down in the range of $100 - 950\,°C$ with

a ramping speed of ca. 1.8 °C.s^{-1}. Fig. 4.28 shows surface brightness at different surface temperatures. Although the surface brightness is also affected by other phenomena, like surface reconstruction, the main contributor remains surface coverage. Comparison of Fig. 4.28a with Fig. 4.28c reveals that Pt surface at high temperatures appears dark, while Pt surface at low temperatures appears bright. During temperature descending, the Pt surface changes its coverage at 140 °C, see Fig. 4.28b. During temperature rising, the Pt surface changes its coverage at 200 °C, see Fig. 4.28d. The coverage change is accompanied by chemical waves traveling over the surface.

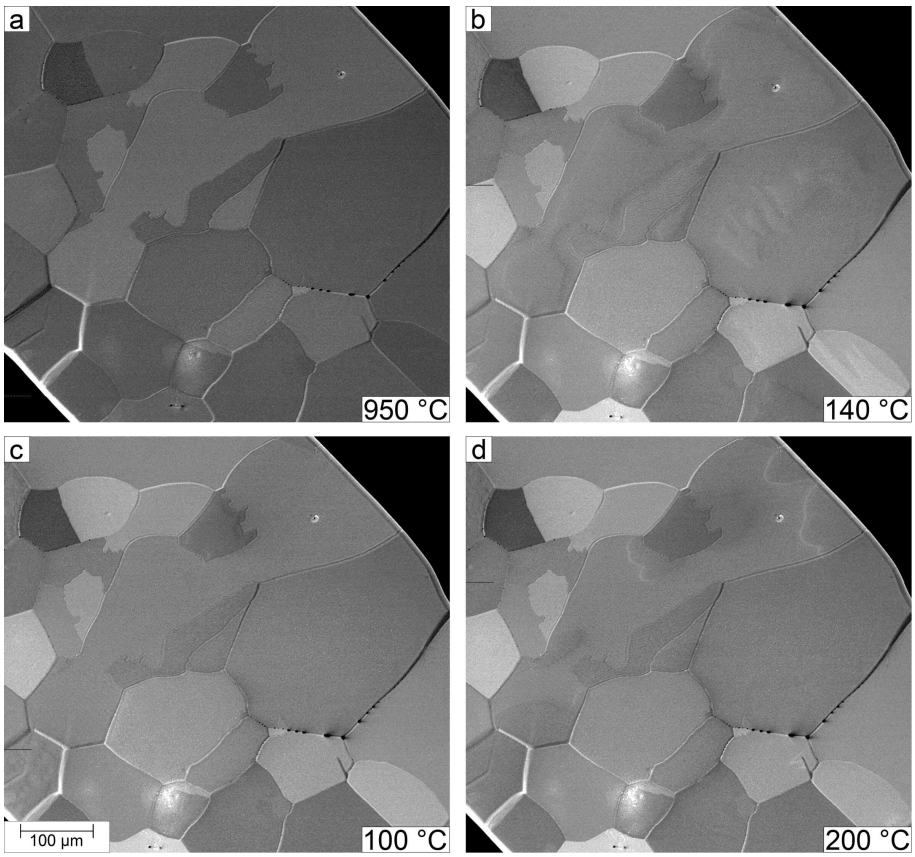

Fig. 4.28: Pt surface brightness at different temperatures observed by UHV-SEM at $p_{CO} = 3.0 \cdot 10^{-4}$ Pa, $p_{O_2} = 1.5 \cdot 10^{-3}$ Pa. a: dark surface at 950 °C; b: chemical waves indicating a change of coverage at 140 °C during temperature decreasing; c: bright surface at 100 °C; d: chemical waves indicating a change of coverage at 200 °C during temperature rising.

Graph showing two heating-cooling cycles in a range of 100 – 950 °C with a ramping speed of ca. 1.8 °C.s^{-1} is displayed in Fig. 4.29. The blue curve represents the temporal evolution of the surface brightness observed by the UHV-SEM. The red curve represents the temporal evolution of oxygen coverage monitored by TOF-SIMS, and the green curve represents CO coverage monitored by TOF-SIMS. Plotting two measurements (UHV-SEM and TOF-SIMS) into one graph reveals that bright Pt surface is CO covered, while oxygen coverage causes Pt surface darkening. One heating-cooling cycle from the graph in Fig. 4.29 is plotted as a temperature dependence in Fig. 4.30. Hysteretic behavior of surface brightness and both coverages may be observed. Similar hysteretic behavior was mathematically modeled by Krischer, Eiswirth, and Ertl [95], see Fig. 4.13. Experimen-

tal observations of the hysteresis phenomenon on heterogeneous catalysts are reviewed in the article of Soubaihi et al. [102]. Explanations of this phenomenon are, however, conflicting; therefore, further study is required.

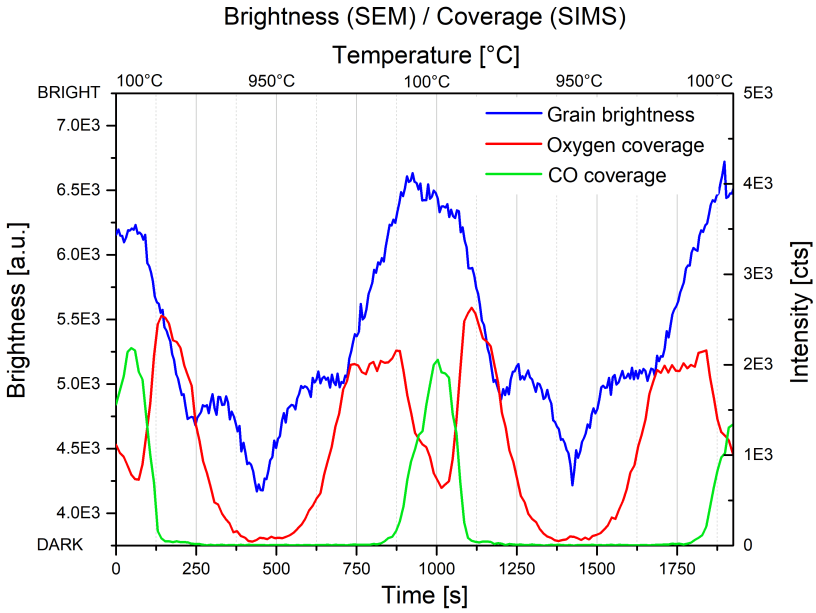

Fig. 4.29: Temporal evolution of Pt surface brightness (blue) observed by UHV-SEM; oxygen coverage (red) observed by TOF-SIMS; CO coverage (green) observed by TOF-SIMS. Partial pressures were set to $p_{CO} = 3.0 \cdot 10^{-4}$ Pa, $p_{O_2} = 1.5 \cdot 10^{-3}$ Pa and temperature was ramping between 100 °C – 950 °C – 100 °C – 950 °C – 100 °C with a ramping speed of 1.8 °C.s^{-1}. CO covered surface at low temperatures appears bright, oxygen coverage at elevated temperatures causes surface darkening.

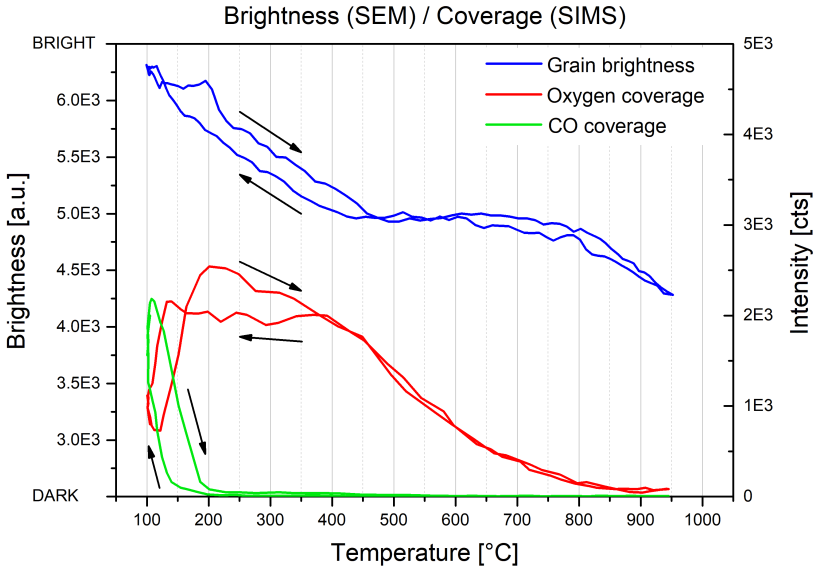

Fig. 4.30: Temperature dependence of Pt surface brightness (blue) observed by UHV-SEM; oxygen coverage (red) observed by TOF-SIMS; CO coverage (green) observed by TOF-SIMS. Partial pressures were set to $p_{CO} = 3.0 \cdot 10^{-4}$ Pa, $p_{O_2} = 1.5 \cdot 10^{-3}$ Pa and temperature was ramping between 100 °C – 950 °C – 100 °C with a ramping speed of 1.8 °C.s^{-1}.

The last temperature-programmed TOF-SIMS experiment examines CO and oxygen coverages in various surrounding atmospheres as a function of temperature. The surface temperature was ramping up and down in the range of 100 – 950 °C with a ramping speed of ca. 1.8 °C.s^{-1}. The first surrounding atmosphere was a well-known CO/O_2 mixture with partial pressures $p_{CO} = 3.0 \cdot 10^{-4}$ Pa, and $p_{O_2} = 1.5 \cdot 10^{-3}$ Pa. The second surrounding atmosphere was a pure O_2 atmosphere with $p_{O_2} = 1.5 \cdot 10^{-3}$ Pa, and the third surrounding atmosphere was a pure CO atmosphere with $p_{CO} = 3.0 \cdot 10^{-4}$ Pa.

Fig. 4.31 shows CO coverage as a function of temperature. Both curves in CO/O_2 and CO surrounding atmospheres exhibit hysteretic behavior. According to the literature, CO molecules desorb from terraces at ca. 400 K (127 °C), while at ca. 500 K (227 °C) CO molecules desorb from steps [76]. In our experiment, the signal of secondary ions proportional to CO coverage ($C_2^- + C_2H^- + C_2H_2^-$) started noticeable decrease at 230 °C, which corresponds to desorption from steps. EBSD measurements observed exclusively high Miller planes on the examined sample which supports the finding of CO desorption from steps. In the mixed CO/O_2 surrounding atmosphere CO coverage declines at around 200 °C during temperature rising and increases at around 140 °C during temperature decreasing. At higher temperatures chemisorbed CO molecules get oxidized by chemisorbed oxygen. The higher intensity of $C_2^- + C_2H^- + C_2H_2^-$ signal may be explained by enhanced ionization probability caused by surrounding O_2 atmosphere.

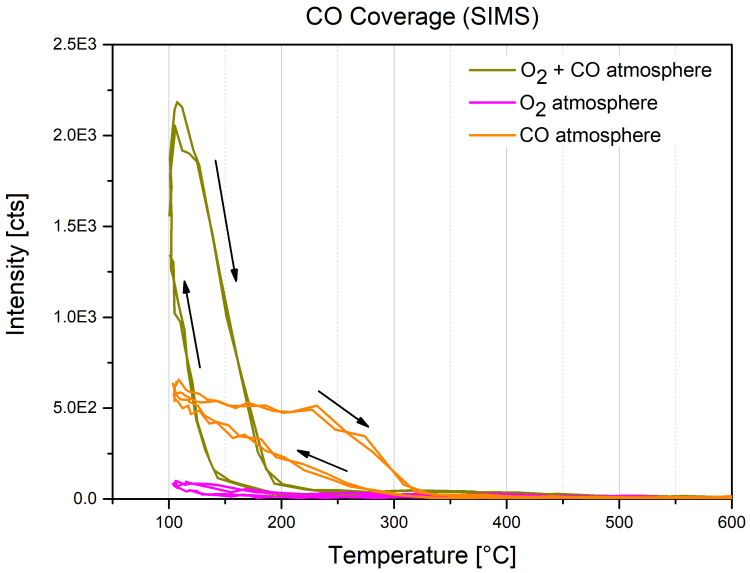

Fig. 4.31: Temperature dependence of CO coverage on Pt surface in $p_{CO} = 3.0 \cdot 10^{-4}$ Pa/$p_{O_2} = 1.5 \cdot 10^{-3}$ Pa surrounding atmosphere (dark green), $p_{O_2} = 1.5 \cdot 10^{-3}$ Pa surrounding atmosphere (pink), and $p_{CO} = 3.0 \cdot 10^{-4}$ Pa surrounding atmosphere (orange). Temperature was ramping between 100 °C – 950 °C – 100 °C – 950 °C – 100 °C with a ramping speed of 1.8 °C.s^{-1}.

Fig. 4.32 shows oxygen coverage as a function of temperature. Both curves in CO/O_2 and O_2 surrounding atmospheres exhibit hysteretic behavior. According to the literature oxygen associatively desorbs from Pt surface at ca. 700 K (427 °C) [70]. In O_2 surrounding atmosphere, oxygen coverage decreased at ca. 355 °C, while in mixed CO/O_2 and O_2 surrounding atmosphere oxygen coverage decrease was observed at ca. 430 °C, which

agrees with literature. The origin of deviation in case of O_2 surrounding atmosphere is unknown. In the mixed CO/O_2 and O_2 surrounding atmosphere oxygen coverage gets saturated at around 200 °C during temperature rising and declines at around 140 °C during temperature decreasing. At low temperatures oxygen coverage gets oxidized by chemisorbed CO.

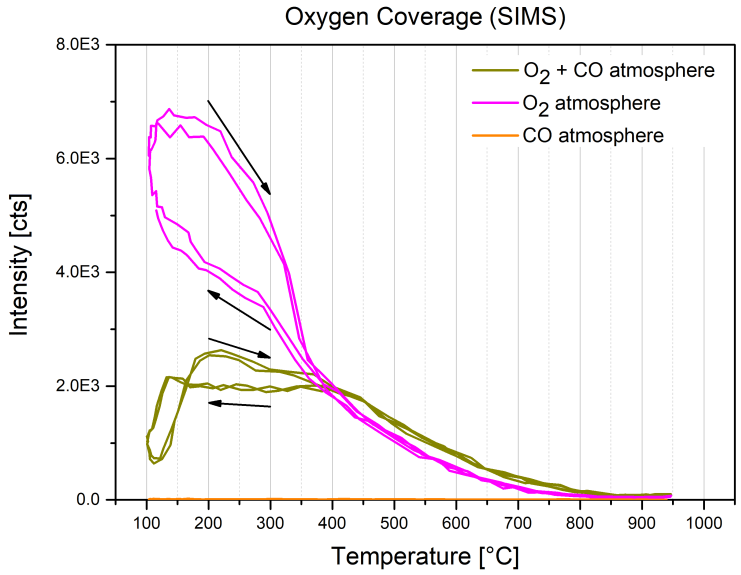

Fig. 4.32: Temperature dependence of oxygen coverage on Pt surface in $p_{CO} = 3.0 \cdot 10^{-4}$ Pa/$p_{O_2} = 1.5 \cdot 10^{-3}$ Pa surrounding atmosphere (dark green), $p_{O_2} = 1.5 \cdot 10^{-3}$ Pa surrounding atmosphere (pink), and $p_{CO} = 3.0 \cdot 10^{-4}$ Pa surrounding atmosphere (orange). Temperature was ramping between 100 °C – 950 °C – 100 °C – 950 °C – 100 °C with a ramping speed of 1.8 °C.s^{-1}.

Conclusion

The presented work demonstrates three different applications of TOF.SIMS 5 instrument from the IONTOF company available at the CEITEC Nano laboratory.

In the first part, a measurement protocol allowing detection of defective high voltage dies on silicon wafers was proposed and tested. The measurement protocol is based on performing leakage current tests at various die locations. The excessive leakage current indicates the presence of defects. Since the active area of examined fast recovery diodes (FRD) and trench insulated gate bipolar transistors (TIGBT) have a typical size of thousands of micrometers, localization of defects with few micrometers in size is necessary for their further characterization by TOF.SIMS 5 instrument. For this purpose, an experimental setup composed of SUMMIT 12000 probe station, Keithley 6517B electrometer, and control computer was assembled. The experimental setup is fully controlled from the newly developed control software with the graphical user interface. A part of the software is devoted to measured data plotting. An automatized measurement of 6-inch wafers with 300 TIGBT dies proved the ability of the proposed assembly to reveal defective dies. The localization of defects was, however, not successful yet. Automated measurements of 6-inch wafers with 579 FRD dies revealed dies with melted edges. The edge melting was induced during previous measurements. In order to identify the exact moment of edge melting, the control software was supplemented with the scanner function, which takes an image of the die surface after each analytical step. This approach could reveal weak areas of the die.

In the second part, a methodology for quantification of Mg dopants in various $Al_xGa_{1-x}N$ samples was proposed. Mg doped $Al_xGa_{1-x}N$ heterostructures characterized by TOF.SIMS 5 instrument are usually intended for high electron mobility transistors (HEMT) production. The proposed methodology is based on the RSF method. For this purpose, 12 Mg doped $Al_xGa_{1-x}N$ calibration samples with varying AlN mole fraction were prepared by the ion implantation technique. TRIM simulations found proper implantation parameters. Total quantification of DSIMS depth profiles requires a set of three calibration curves that were constructed. The first calibration curve serves for a depth scale quantification. The second curve serves to quantify matrix species, and the last curve serves to quantify dopant concentrations. The quantification of matrix species requires one $Al_xGa_{1-x}N$ calibration sample with $x \in \langle 0.13, 0.6, \rangle$. The quantification of Mg dopants requires Mg doped GaN, Mg doped AlN, and one Mg doped $Al_xGa_{1-x}N$ $x \in \langle 0.26, 0.6, \rangle$ calibration sample.

In the third part, the abilities of TOF-SIMS in the heterogeneous catalysis research were demonstrated. Two main conclusions may be drawn from static SIMS monitoring of spatiotemporal patterns during catalytic CO oxidation by O_2 on Pt surfaces. Firstly, long-term, real-time imaging of reaction-diffusion processes on catalyst surfaces by 30 keV Bi^+ ion probe is possible. Secondly, ion-induced surface damage is not necessarily fatal for reaction-diffusion processes because spatiotemporal patterns in the TOF.SIMS 5 instrument could be observed for a much longer time than in the UHV-SEM instrument. Temperature programmed TOF-SIMS measurements correlated with temperature programmed UHV-SEM measurements revealed that CO covered Pt surface appears bright, and oxygen covered Pt surface appears dark in electron micrographs.

References

[1] Colliex, C. The "father" of microanalysis: Raymond Castaing, creator of a generation of scientific instruments, still in worldwide operation. *C. R. Physique* 2019; 20 (7-8), 746-755.
DOI: 10.1016/j.crhy.2018.12.001

[2] Chait, B. T.; Standing, K. G. A time-of-flight mass spectrometer for measurement of secondary ion mass spectra. *Int. J. Mass Spectrom. Ion Phys.* 1981; 40, 185-193.
DOI: 10.1016/0020-7381(81)80041-1

[3] IONTOF (2021). *TOF.SIMS 5: the most sold TOF-SIMS instrument world wide.* Available at: `https://www.iontof.com` (Accessed: 7 May 2021).

[4] Heide, P. *Secondary ion mass spectrometry: An introduction to principles and practices.* John Wiley & Sons, Inc., 2014; 365 p. ISBN: 978-1-118-48048-9

[5] IONTOF (2019). *SurfaceLab 6 Help 7.0.*

[6] Ziegler, J. F.; Biersack, J. P.; Ziegler, M. D. *SRIM: The stopping and range of ions in matter.* SRIM Co., 2008; 398 p. ISBN: 978-0-9654207-1-6

[7] Alford, T.; Feldman, L.; Mayer, J. *Fundamentals of nanoscale films analysis.* Springer, 2007; 349 p.
ISBN: 978-0-387-29260-1

[8] Janák, M. (2019). *Calibration of SIMS method by implantation profiles.* Bachelor's thesis. Brno University of Technology. Available at: `https://www.vutbr.cz` (Accessed: 7 May 2021).

[9] Gu, C. J. (2005). *SIMS Quantification of Matrix and Impurity Species in III-Nitride Alloys.* Thesis. North Carolina State University. Available at: `https://repository.lib.ncsu.edu` (Accessed: 7 May 2021).

[10] Gu, C. J.; Stevie, F. A.; Hitzman, C. J.; Saripalli, Y. N.; Johnson, M.; Griffis, D. P. SIMS quantification of matrix and impurity species in $Al_xGa_{1-x}N$. *Appl. Surf. Sci.* 2006; 252, 7228-7231.
DOI: 10.1016/j.apsusc.2006.02.148

[11] Yoshida, S.; Misawa, S.; Gonda, S. Properties of $Al_xGa_{1-x}N$ films prepared by reactive molecular beam epitaxy. *J. Appl. Phys.* 1982; 53, 6844-6848.
DOI: 10.1063/1.329998

[12] Tang, L.; Tang, B.; Zhang, H.; Yuan, Y. Review – Review of research on AlGaN MOCVD growth. *ECS J. Solid State Sci. Technol.* 2020; 9 (2), 024009.
DOI: 10.1149/2162-8777/ab6833

[13] Bernardini, F.; Fiorentini V. Spontaneous polarization and piezoelectric constants of III-V nitrides. *Phys. Rev. B* 1997; 56 (16), R10024-R10027.
DOI: 10.1103/PhysRevB.56.R10024

[14] Nagasawa, Y.; Hirano, A. A review of AlGaN-based deep-ultraviolet light-emitting diodes on sapphire. *Appl. Sci.* 2018; 8 (8), 1264.
DOI: 10.3390/app8081264

[15] Lin, Y. Activation mechanism of annealed Mg-doped GaN in air. *Appl. Phys. Lett.* 2004; 84, 2760.
DOI: 10.1063/1.1704873

[16] Zheng, T. C.; Lin, W.; Liu, R.; Cai, D. J.; Li, J. C.; Li, S. P.; Kang, J. Y. Improved p-type conductivity in Al-rich AlGaN using multidimensional Mg-doped superlattices. *Sci. Rep.* 2019; 6 (1), 21897.
DOI: 10.1038/srep21897

[17] Castiglia, A.; Carlin, J. F.; Grandjean, N. Role of stable and metastable Mg-H complexes in p-type GaN for cw blue laser diodes. *Appl. Phys. Lett.* 2011; 98, 213505.
DOI: 10.1063/1.3593964

[18] Zvanut, M. E.; Sunay, U. R.; Dashdorj, J.; Willoughby, W. R. Mg-hydrogen interaction in AlGaN alloys. In *Gallium nitride materials and devices VII*; Chyi, J.; Nanishi, Y.; Morkoc, H.; Piprek, J.; Yoon, E.; SPIE, 8262, 2012.
DOI: 10.1117/12.916073

[19] Köhler, K.; Gutt, R.; Wiegert, J.; Kirste, L. Diffusion of Mg dopant in metal-organic vapor-phase epitaxy grown GaN and $Al_xGa_{1-x}N$. *J. Appl. Phys.* 2013; 113, 073514.
DOI: 10.1063/1.4792662

[20] Pérez-Tomás, A.; Placidi, M.; Baron, N.; Chenot, S.; Cordier, Y.; Moreno, J. C.; Millán, J.; Godignon, P. 2DEG HEMT mobility vs inversion channel MOSFET mobility. *Mater. Sci. Forum* 2010; 645-648, 1207-1210.
DOI: 10.4028/www.scientific.net/MSF.645-648.1207

[21] Roccaforte, F.; Greco, G.; Fiorenza, P.; Iucolano, F. An overview of normally-off GaN-based high electron mobility transistors. *Materials* 2019; 12, 1599.
DOI: 10.3390/ma12101599

[22] Fearn, S. Modes of analysis. In *An introduction to time-of-flight secondary ion mass spectrometry (TOF-SIMS) and its application to materials science.* Fearn, S.; Morgan & Claypool Publishers, 2015; pp. 3-1 – 3-5. Online ISBN: 978-1-6817-4088-1
DOI: 10.1088/978-1-6817-4088-1ch3

[23] Ioffe Institute. *New semiconductor materials. Characteristics and properties.* Available at: `http://www.ioffe.ru/SVA/NSM/Semicond/` (Accessed: 19 May 2021).

[24] Kinoshita, H.; Türkan, H.; Vucinic, S.; Naqvi, S.; Bedair, R.; Rezaee, R.; Tsatsakis, A. Carbon monoxide poisoning. *Toxicol. Rep.* 2020; 7, 169-173.
DOI: 10.1016/j.toxrep.2020.01.005

[25] Garzia, G.; Koper, M. T. M. Carbon monoxide oxidation on Pt single crystal electrodes: Understanding the catalysis for low temperature fuel cells. *ChemPhysChem* 2011; 12 (11), 2064-2072.
DOI: 10.1002/cphc.201100247

[26] Oh, S. H., Sinkevitch, R. M. Carbon monoxide removal from hydrogen-rich fuel cell feedstreams by selective catalytic oxidation. *J. Catal.* 1993; 142 (1), 254-262. DOI: 10.1006/jcat.1993.1205

[27] Holton, O. T.; Stevenson, J. W. The role of platinum in proton exchange membrane fuel cells. *Platinum Metals Rev.* 2013; 57 (4), 259-271. DOI: 10.1595/147106713x671222

[28] Acres, G. J. K. Platinum group metal catalysis at the end of this century. *Mater. Des.* 1987; 8 (5), 258-262. DOI: 10.1016/0261-3069(87)90002-1

[29] Dey, S.; Dhal, G. C. Property and structure of various platinum catalysts for low--temperature carbon monoxide oxidations. *Mater. Today Chem.* 2020; 16, 100228. DOI: 10.1016/j.mtchem.2019.100228

[30] Shido, T.; Prins, R. Application of synchrotron radiation to in situ characterization of catalysts. *Curr. Opin. Solid State Mater. Sci.* 1998; 3 (4), 330-335. DOI: 10.1016/S1359-0286(98)80041-7

[31] He, B.; Zhang, Y.; Liu, X.; Chen, L. In-situ transmission electron microscope techniques for heterogeneous catalysis. *ChemCatChem* 2020, 12 (7), 1853-1872. DOI: 10.1002/cctc.201902285

[32] Lindström, B.; Pettersson, L. J. A brief history of catalysis. *CATTECH* 2003; 7, 130-138. DOI: 10.1023/A:1025001809516

[33] Ertl G. Reaction at surfaces: From atoms to complexity (Nobel Lecture). *Angew. Chem. Int. Ed. Engl.* 2008; 47 (19), 3524-3535. DOI: 10.1002/anie.200800480

[34] Grand View Research Inc. (2020). *Catalyst market size worth $48.0 billion by 2027.* Available at: `https://www.grandviewresearch.com` (Accessed: 20 April 2021).

[35] Humphreys, J.; Lan, R.; Tao, S. Development and recent progress on amonia synthesis catalysts for Haber-Bosch process. *Adv. Energy Sustainability Res.* 2021; 2, 2000043. DOI: 10.1002/aesr.202000043

[36] Jahangiri, H.; Bennett, J.; Mahjoubi, P.; Wilson, K.; Gu, S. A review of advanced catalyst development for Fischer-Tropsch synthesis of hydrocarbons from biomass derived syn-gas. *Catal. Sci. Technol.* 2014; 4, 2210-2229. DOI: 10.1039/C4CY00327F

[37] Li, X.; Zhang, J.; Zhang, M.; Zhang, W.; Zhang, M.; Xie, H.; Wu, Y.; Tan, Y. The support effect on the direct conversion of syngas to higher alcohol synthesis over copper-based catalysts. *Catalysts* 2019; 9, 199. DOI: 10.3390/catal9020199

[38] Speight, J. G. Catalytic cracking. In *The Refinery of the Future (Second Edition)*; Spent, J. G.; Gulf Professional Publishing, 2020, pp. 197-226. DOI: 10.1016/B978-0-12-816994-0.00006-3

[39] Jiang, X.; Nie, X.; Guo, X.; Song, C.; Chen, J. G. Recent advances in carbon dioxide hydrogenation to methanol via heterogeneous catalysis. *Chem. Rev.* 2020; 120, 7984-8034.
DOI: 10.1021/acs.chemrev.9b00723

[40] Stølen, S.; Grande, T. *Chemical Thermodynamics of Materials: Macroscopic and Microscopic Aspects.* John Wiley & Sons, Ltd., 2004; 408 p.
ISBN: 978-0-470-09267-5

[41] Rothenberg, G. *Catalysis: Concepts and Green Applications*; Wiley-VCH, 2008; 279 p. Online ISBN: 9783527621866.
DOI: 10.1002/9783527621866

[42] 'Catalytic cycle' (2021). *Wikipedia.* Available at: `https://en.wikipedia.org/wiki/Catalytic_cycle` (Accessed: 6. May 2021).

[43] Medford, A. J.; Vojvodic, A.; Hummelshøj, J. S.; Voss, J.; Abild-Pedersen, F.; Studt, F.; Bligaard, T.; Nilsson, A.; Nørskov, J. K. From the Sabatier principle to a predictive theory of transition-metal heterogeneous catalysis. *J. Catal.* 2015; 328, 36-42.
DOI: 10.1016/j.jcat.2014.12.033

[44] Wang, J.; Lu, S.; Li, J.; Li, C. Remarkable difference in CO_2 hydrogenation to methanol on Pd nanoparticles supported inside and outside of carbon nanotubes. *Chem. Commun.* 2015; 51, 17615-17618.
DOI: 10.1039/C5CC07079A

[45] Richardson, J. T. Structure of catalysts. In *Principles of Catalyst Development. Fundamental and Applied Catalysis*; Richardson, J. T.; Springer, 1989; pp. 23-39.
DOI: 10.1007/978-1-4899-3725-4_2

[46] Mross, W. D. Alkali doping in heterogeneous catalysis. *Catal. Rev.* 1983; 25 (4), 591-637.
DOI: 10.1080/01614948308078057

[47] Zhang, Z.; Lagally, M. G. Atomistic processes in the early stages of thin film growth. *Science* 1997; 276 (5311), 377-383.
DOI: 10.1126/science.276.5311.377

[48] Gritsch, T.; Coulman, D.; Behm, R. J.; Ertl, G. Mechanism of the CO-induced 1×2 - 1×1 structural transformation of Pt(110). *Phys. Rev. Lett.* 1989; 63 (10), 1086-1089.
DOI: 10.1103/PhysRevLett.63.1086

[49] Qu, Z.; Cheng, M.; Huang, W.; Bao, X. Formation of subsurface oxygen species and its high activity toward CO oxidation over silver catalysts. *J. Catal.* 2005; 229 (2), 446-458.
DOI: 10.1016/j.jcat.2004.11.043

[50] Wrobel, R. J.; Becker, S.; Weiss, H. Influence of subsurface oxygen in the catalytic CO oxidation on Pd(111). *J. Phys. Chem. C* 2015; 119 (10), 5386-5394.
DOI: 10.1021/jp508952f

[51] Weijing, D.; Weihong, Z.; Xiaodong, Z.; Baofeng, Z.; Lei, C.; Laizhi, S.; Shuangxia, Y.; Haibin, G.; Guanyi C.; Liang, Z.; Ge, S. The application of DFT in catalysis and adsorption reaction system. *Energy Procedia* 2018; 152, 997-1002.
DOI: 10.1016/j.egypro.2018.09.106

[52] Ertl, G. Oscillatory kinetics and spatio-temporal self-organization in reactions at solid surfaces. *Science* 1991; 254 (5039), 1750-1755.
DOI: 10.1126/science.254.5039.1750

[53] World Platinum Investment Council Ltd. (2021). *Platinum quarterly Q4 2020.* Available at: `https://platinuminvestment.com` (Accessed: 20 April 2021).

[54] World Gold Council Ltd. (2020). *Gold demand trends full year and Q4 2019.* Available at: `https://www.gold.org` (Accessed: 20 April 2021).

[55] Ganong, W. F. Review of Medical Physiology – 21st Ed. McGraw-Hill Publishing Company, 2003; 2305 p. ISBN: 9780071402361.

[56] Greiner, T. H. (1997). *Carbon monoxide concentrations: table (AEN-172).* Available at: `https://www.abe.iastate.edu` (Accessed: 20 April 2021)

[57] Paranjpe, R.; Suresh, A. K.; Aghalayam, P. Understanding Pt-Rh synergy in a three--way catalytic converter. *Int. J. Chem. React. Eng.* 2013; 11 (1), 1-8.
DOI: 10.1515/ijcre-2013-0072

[58] Mahannah, J. (2015). *Catalytic converter.* Available at: `https://science-art.com` (Accessed: 6 May 2021).

[59] Empa (2019). *Empa Quarterly.* Available at: `https://www.empa.ch/documents/56164/11637868/Empa_Quarterly67_EN_Web.pdf` (Accessed: 6 May 2021)

[60] Salivanchuk, S. *Strong car traffic jams in the city.* Available at: `https://stock.adobe.com` (Accessed: 6 May 2021).

[61] Queiroz, C. M. S.; Machado, A. P.; Paiva, A. R. N.; Antoniassi, R. M.; Vaz, J. M.; Spinacé, E. V. Active Pt/CeO_2 catalysts prepared by an alcohol-reduction process for low-temperature CO-PROX reaction. *Mater. Renew. Sustain. Energy* 2019; 8 (3), 17.
DOI: 10.1007/s40243-019-0155-y

[62] Waugh, K. C.; Butler, D.; Hayden, B. E. The mechanism of the poisoning of ammonia synthesis catalysts by oxygenates O_2, CO, H_2O: An in situ method for active surface determination. *Catal. Lett.* 1994; 24, 197-210.
DOI: 10.1007/BF00807390

[63] Punde, S. S.; Tatarchuk, B. J. Metal microfibers entrapped catalysts as effective ambient temperature CO oxidation catalysts. *Appl. Catal. A Gen.* 2012; 441-442, 54-64.
DOI: 10.1016/j.apcata.2012.07.021

[64] Blakely, D. W.; Somorjai, G. A. The stability and structure of high Miller index platinum crystal surfaces in vacuum and in the presence of adsorbed carbon and oxygen. *Surf. Sci.* 1977; 65, 419-442.
DOI: 10.1016/0039-6028(77)90457-5

[65] Ducros, R.; Merrill, R. P The interaction of oxygen with Pt(110). *Surf. Sci.* 1976; 55, 227-245.
DOI: 10.1016/0039-6028(76)90386-1

[66] Santos, V. P.; Camara, G. A. Platinum single crystal electrodes: Prediction of the surface structures of low and high Miller indexes faces. *Results in Surfaces and Interfaces* 2021; 3, 100006.
DOI: 10.1016/j.rsurfi.2021.100006

[67] Cheng, T.; Parish, C. M.; More, K. L. Synthesis of platinum single-crystal nanoparticles in water vapor. *J. Mater. Sci.* 2013; 48, 3834-3840.
DOI: 10.1007/s10853-013-7184-1

[68] Imbihl, R.; Ertl, G. Oscillatory kinetics in heterogeneous catalysis. *Chem. Rev.* 1995; 95, 697-733.
DOI: 10.1021/cr00035a012

[69] Winkler, A.; Guo, X.; Siddiqui, H. R.; Hagans, P. L.; Yates, J. T. Kinetics and energetics of oxygen adsorption on Pt(111) and Pt(112) – A comparison of flat and stepped surfaces. *Surf. Sci.* 1988; 201 (3), 419-443.
DOI: 10.1016/0039-6028(88)90495-5

[70] Petrova, N. V.; Yakovkin, I. N. Mechanism of associative oxygen desorption from Pt(111) surface. *Eur. Phys. J. B* 2007; 58, 257-262.
DOI: 10.1140/epjb/e2007-00234-0

[71] Šljivančanin, Ž.; Hammer, B. Oxygen dissociation at close-packed Pt terraces, Pt steps, and Ag-covered Pt steps studies with density functional theory. *Surf. Sci.* 2002; 515 (1), 235-244.
DOI: 10.1016/s0039-6028(02)01908-8

[72] Gambardella, P.; Šljivančanin, Ž.; Hammer, B.; Blanc, M.; Kuhnke, K.; Kern, K. Oxygen dissociation at Pt steps. *Phys. Rev. Lett.* 2021; 87 (5), 056103.
DOI: 10.1103/physrevlett.87.056103

[73] Bashlakov, D. L.; Juurlink, L. B. F.; Koper, M. T. M.; Yanson, A. I. Subsurface oxygen on Pt(111) and its reactivity for CO oxidation. *Catal. Lett.* 2012; 142 (1), 1-6.
DOI: 10.1007/s10562-011-0730-z

[74] McEwen, J. S.; Bray, J. M.; Wu, C.; Schneider, W. F. How low can you go? Minimum energy pathways for O2 dissociation on Pt(111). *Phys. Chem. Chem. Phys.* 2012; 14 (48), 16677.
DOI: 10.1039/c2cp42225e

[75] Doyen, G.; Ertl, G. Theory of carbon monoxide chemisorption on transition metals. *Surf. Sci.* 1974; 43 (1), 197-229.
DOI: 10.1016/0039-6028(74)90228-3

[76] Xu, J.; Yates, J. T. Terrace width effect on adsorbate vibrations: A comparison of Pt(335) and Pt(112) for chemisorption of CO. *Surf. Sci.* 1995; 327 (3), 193-201.
DOI: 10.1016/0039-6028(94)00849-3

[77] Gunasooriya, G. T. K. K.; Saeys, M. CO adsorption on Pt(111): From isolated molecules to ordered high-coverage structures. *ACS Catal.* 2018; 8 (11), 10225–10233.
DOI: 10.1021/acscatal.8b02371

[78] Lakshmikanth, K. G.; Kundappaden, I.; Chatanathodi, R. A DFT study of CO adsorption on Pt(111) using van der Waals functionals. *Surf. Sci.* 2018; 681, 143-148.
DOI: 10.1016/j.susc.2018.12.001

[79] Bonzel, H. P.; Ku, R. Mechanisms of the catalytic carbon monoxide oxidation on Pt(110). *Surf. Sci.* 1972; 33 (1), 91-106.
DOI: 10.1016/0039-6028(72)90101-X

[80] Campbell, C. T.; Ertl, G.; Kruipers, H.; Segner, J. A molecular beam study of the catalytic oxidation of CO on a Pt(111) surface. *J. Chem. Phys.* 1980; 73 (11), 5862-5873.
DOI: 10.1063/1.440029

[81] Engel, T.; Ertl, G. Elementary steps in the catalytic oxidation of carbon monoxide on platinum metals. In *Advances in Catalysis*; Eley, D. D.; Pines, H.; Weez, P. B.; Academic Press, 28, 1979; pp. 1-78.
DOI: 10.1016/S0360-0564(08)60133-9

[82] Neumann, S.; Gutmann, T.; Buntkowsky, G.; Paul, S.; Thiele, G.; Sievers, H.; Bäumer, M.; Kunz, S. Insight into the reaction mechanism and particle size effect of CO oxidation over supported Pt nanoparticle catalysts. *J. Catal.* 2019; 377, 662-672.
DOI: 10.1016/j.jcat.2019.07.049

[83] Baxter, R. J.; Hu, P. Insight into why the Langmuir-Hinshelwood mechanism is generally preferred. *J. Chem. Phys.* 2002; 116 (11), 4379-4381.
DOI: 10.1063/1.1458938

[84] Grabow, L.; Xu, Y.; Mavrikakis, M. Lattice strain effects on CO oxidation on Pt(111). *Phys. Chem. Chem. Phys.* 2006; 8 (29), 3369–3374.
DOI: 10.1039/b606131a

[85] Neugebohren, J.; Borodin, D.; Hahn, H. W.; Altschäffel, J.; Kandratsenka, A.; Auerbach, D. J.; Campbell C. T.; Schwarzer, D.; Harding, D. J.; Wodtke, A. M.; Kitsopoulos, T. N. Velocity-resolved kinetics of site-specific carbon monoxide oxidation on platinum surfaces. *Nature* 2018; 558 (7709), 280-283.
DOI: 10.1038/s41586-018-0188-x

[86] Minot, C. Modeling of high-pressure CO dissociation on Pt(100) and Pt(111). *Catal. Today* 2004; 89, 357-362.
DOI: 10.1016/j.cattod.2003.12.016

[87] Langmuir, I. The mechanism of the catalytic action of platinum in the reaction $2CO + O_2 = 2CO_2$ and $2H_2 + O_2 = 2H_2O$. *Trans. Faraday Soc.* 1922; 17, 621-654.
DOI: 10.1039/TF9221700621

[88] Allian, A. D.; Takanabe, K.; Fujdala, K. L.; Hao, X.; Truex, T. J.; Cai, J.; Buda, C.; Neurock, M.; Iglesia, E. Chemisorption of CO and mechanism of CO oxidation on supported platinum nanoclusters. *J. Am. Chem. Soc.* 2011; 133 (12), 4498–4517.
DOI: 10.1021/ja110073u

[89] Spronsen, M. A.; Frenken, J. W. M.; Groot, I. M. N. Observing the oxidation of platinum. *Nat. Commun.* 2017; 8 (1), 429.
DOI: 10.1038/s41467-017-00643-z

[90] Hendriksen, B. L. M.; Frenken, J. W. M. CO oxidation on Pt(110): Scanning tunneling microscopy inside a high-pressure flow reactor. *Phys. Rev. Lett.* 2002; 89 (4), 046101.
DOI: 10.1103/PhysRevLett.89.046101

[91] Pedersen, T. M.; Li, W. X.; Hammer, B. Structure and activity of oxidized Pt(110) and $-PtO_2$. *Phys. Chem. Chem. Phys.* 2006; 8 (13), 1566-1574.
DOI: 10.1039/B515166J

[92] Wang, J. G.; Li, W. X.; Borg, M.; Gustafson, J.; Mikkelsen, A.; Pedersen, T. M.; Lundgren, E.; Weissenrieder, J.; Klikovits, J.; Schmid, M.; Hammer, B.; Andersen, J. N. One-dimensional PtO_2 at Pt steps: formation and reaction with CO. *Phys. Rev. Lett.* 2005; 95 (25), 256102.
DOI: 10.1103/PhysRevLett.95.256102

[93] Ertl, G. Temporal and spatial self-organisation in catalysis at single crystal surfaces. *Catal. Lett.* 1991; 9 (3-4), 219-230.
DOI: 10.1007/bf00773180

[94] Kiprijanov, K. S. Chaos and beauty in a beaker: The early history of the Belusov-Zhabotinsky reaction. *Ann. Phys.* 2016; 528 (3-4), 233-237.
DOI: 10.1002/andp.201600025

[95] Krischer, K.; Eiswirth, M.; Ertl, G. Oscillatory CO oxidation on Pt(110): Modeling of temporal self-organization. *J. Chem. Phys.* 1992; 96 (12), 9161.
DOI: 10.1063/1.462226

[96] Ryzha, I.; Matseliukh, M. Carbon monoxide oxidation on the Pt-catalyst: Modelling and stability. *MMC.* 2017; 4 (1), 96-106.
DOI: 10.23939/mmc2017.01.096

[97] Ryzha, I.; Gaiduchok, O. Mathematical model for carbon monoxide oxidation: Influence of diffusion effects. *MMC.* 2019; 6 (1), 129-136.
DOI: 10.23939/mmc2019.01.129

[98] Bzovska, I. S.; Mryglod, I. M. Spatiotemporal patterns formation in a three-variable CO oxidation reaction model. *Condens. Matter Phys.* 2018; 21 (2), 23801.
DOI: 10.5488/CMP.21.23801

[99] Cox, M. P.; Ertl, G.; Imbihl, R. Spatial self-organization of surface structure during an oscillating catalytic reaction. *Phys. Rev. Lett.* 1985; 54 (15), 1725-1728. DOI: 10.1103/physrevlett.54.1725

[100] Lele, T. P.; Pletcher, T. D.; Lauterbach, J. Spatiotemporal patterns during CO oxidation on Pt(100) at elevated pressures. *AIChE J.* 2001; 47 (6), 1414-1424. DOI: 10.1002/aic.690470617

[101] AMISPEC project (2021). Available at: `http://amispec.isibrno.cz/doku.php` (Accessed: 6 May 2021).

[102] Soubaihi, R. M. A.; Saoud, K. M.; Dutta, J. Critical review of low-temperature CO oxidation and hysteresis phenomenon on heterogeneous catalysts. *Catalysts* 2018; 8 (12), 660. DOI: 10.3390/catal8120660

List of abbreviations and symbols

2DEG	two dimensional electron gas
AES	auger electron spectroscopy
DC	direct current
DFT	density functional theory
DSIMS	dynamic secondary ion mass spectrometry
EBSD	electron backscatter diffraction
FCC structure	face-centered cubic structure
FIB	focused ion beam
FRD	fast recovery diode
GCIB	gas cluster ion beam
GUI	graphical user interface
HEMT	high electron mobility transistor
KEE model	Krischer-Eiswirth-Ertl model
LEED	low-energy electron diffraction
LEIS	low-energy ion scattering
LMIS	liquid metal ion source
MCP	microchannel plate
MOCVD	metal-organic chemical vapor deposition
MOSFET	metal-oxide semiconductor field effect transistor
MPS	molecular precursor state
ODE	ordinary differential equation
PEEM	photoemission electron microscopy
RSF	relative sensitivity factor
SEM	scanning electron microscopy
SIMS	secondary ion mass spectrometry
SSIMS	static secondary ion mass spectrometry
STM	scanning tunneling microscopy

TIGBT	trench insulated gate bipolar transistor
TOF-SIMS	time-of-flight secondary ion mass spectrometry
TPD	temperature-programmed desorption
TS	transition state
UHV-SEM	ultrahigh vacuum scanning electron microscopy
XPS	X-ray photoelectron spectroscopy